X-ray Scattering Investigations of the Structure of Water and Ice in Periodic Mesoporous Organosilicas

Dissertation
zur Erlangung des Doktorgrades
an der Fakultät für Mathematik, Informatik und Naturwissenschaften
Fachbereich Physik
der Universität Hamburg

vorgelegt von
Niels Christian Gießelmann

Hamburg
2025

Gutachter/innen der Dissertation:	Prof. Dr. Andreas Stierle
	Prof. Dr. Michael Fröba
Zusammensetzung der Prüfungskommission:	Prof. Dr. Andreas Stierle
	Prof. Dr. Michael Fröba
	Prof. Dr. Patrick Huber
	Dr. Felix Lehmkühler
Vorsitzende/r der Prüfungskommission:	Prof. Dr. Daniela Pfannkuche
Datum der Disputation:	15.10.2025
Vorsitzender des Fach-Promotionsausschusses PHYSIK:	Prof. Dr. Wolfgang J. Parak
Leiter des Fachbereichs PHYSIK:	Prof. Dr. Markus Drescher
Dekan der Fakultät MIN:	Prof. Dr.-Ing. Norbert Ritter

Abstract

Water is one of the most common materials on Earth and in everyday life. However, with its many anomalies which in many cases get further amplified when supercooled, it is still poorly understood. A particularly interesting case is water under confinement. When water is subject to spatial restrictions, it has been found that the structure of its network is influenced and its equilibrium and dynamical properties vary. An interesting confining matrix for water is found in the form of periodic mesoporous organosilicas (PMOs). These materials enable mesoporous confinement in a broad range of pore diameters with the possibility of tuning the pore wall-water interaction. This is achieved by organic moieties in the pore wall, which can house additional functional groups. These groups can for example have hydrophobic or hydrophilic properties. This thesis investigates the structure of water and ice under confinement in a broad range of PMOs with different pore diameters and pore wall functionalizations, by use of X-ray scattering. A strong dependence of the structure of confined water on the pore functionalization, as well as the pore diameter is found. Pores with smaller diameters and hydrophilic functionalizations lead to a decrease in density when compared to bulk water. Furthermore, a stronger tetrahedral water network is observed in these pores. At lower temperatures, an ice structure with diffuse cubic-like, hexagonal and amorphous contributions is observed. The hexagonal component also exhibits a shift in its lattice parameters when compared to bulk hexagonal ice. In smaller, hydrophilic pores, the ice crystallites are furthermore oriented in specific, preferred angles compared to the pore axis. It is also observed that the PMO host materials undergo a deformation when water is being adsorbed. Specifically, the periodicity of their organic moieties changes in dependence on their interaction with water.

Zusammenfassung

Wasser ist eines der häufigsten Materialien auf der Erde, wie auch im täglichen Leben. Mit seinen zahlreichen Anomalien, die sich in vielen Fällen bei Unterkühlung noch verstärken, gibt es jedoch noch einige Rätsel auf. Ein besonders interessanter Fall ist Wasser in nanometergroßen Poren. Wenn es solchen räumlichen Beschränkungen unterworfen ist, wurde festgestellt, dass die Struktur des Wassernetzwerks beeinflusst wird und sich seine Gleichgewichts- und dynamischen Eigenschaften verändern. Eine interessante Einschlussmatrix für Wasser sind periodische mesoporöse Organosilikate (PMOs). Diese Materialien bieten ein breites Spektrum von Porendurchmessern mit der Möglichkeit, die Wechselwirkung zwischen Porenwand und Wasser zu steuern. Dies wird durch organische Bestandteile in der Porenwand erreicht, die zusätzliche funktionelle Gruppen enthalten können. Diese Gruppen haben zum Beispiel hydrophobe oder hydrophile Eigenschaften. In dieser Arbeit wird die Struktur von Wasser und Eis unter Einschluss in einer breiten Auswahl von PMOs mit unterschiedlichen Porendurchmessern und Porenwandfunktionalisierungen mit Hilfe von Röntgenstreuung untersucht. Es zeigt sich eine starke Abhängigkeit der Struktur des eingeschlossenen Wassers von Porenfunktionalisierung und -durchmesser. Poren mit kleineren Durchmessern und hydrophilen Funktionalisierungen führen zu einer Verringerung der Dichte im Vergleich zur Bulk-Wasser. Außerdem wird in diesen Poren ein stärker ausgebildetes tetraedrisches Wassernetzwerk beobachtet. Bei niedrigeren Temperaturen wird eine Eisstruktur mit diffusen kubischen, hexagonalen und amorphen Anteilen beobachtet. Die hexagonale Komponente weist auch eine Verschiebung ihrer Gitterkonstanten im Vergleich zu hexagonalem Bulk-Eis auf. In kleineren, hydrophilen Poren sind die Eiskristallite außerdem in bestimmten, bevorzugten Winkeln relativ zur Porenachse ausgerichtet. Es wird auch beobachtet, dass die PMO-Materialien selbst auch eine Verformung erfahren, wenn Wasser adsorbiert wird. Insbesondere ändert sich die Periodizität ihrer organischen Bestandteile in Abhängigkeit von ihrer Wechselwirkung mit Wasser.

Contents

List of Figures

1 Introduction

Water is one of the most common materials on Earth and is crucial for life.[1–3] However, despite the long history of water research, its properties are still relatively poorly understood with many behaviors and anomalies that are not expected in a simple liquid.[4–9] In most cases, these deviating behaviors are further amplified at supercooled temperatures.[4] But also its solid form, ice, presents a rich field of study with around 20 crystalline and at least three amorphous phases.[10–13]

A particularly interesting case is water under confinement. Confined water is quite common on Earth, for example in sediments or even in the human body. When water is subject to spatial restrictions, it has been found that the structure of its hydrogen-bond network is influenced and its equilibrium and dynamical properties vary.[14–17] Examples of confinement effects in water, specifically when confined in silica-based porous materials, are a lower melting point[18] and lower average density[19–21] when compared to bulk water. Furthermore, the structure of ice is also altered when subject to confinement.[22,23]

Periodic mesoporous organosilicas (PMOs) are interesting as a confinement matrix for water. These SiO_2-based materials posses periodically arranged organic moieties in the pore walls, which form a crystal-like wall structure.[24–31] Furthermore, the organic moieties can host functional components, which can influence the interaction between the pore walls and the confined water.[32–35]

So far, the structure and dynamics of water in these systems has been studied by means of spectroscopy[36] or quasi-elastic neutron scattering (QENS).[34,35] Employing X-ray scattering could give important information, especially about the structuring behavior of water in PMOs. In previous studies of water in confinement, spectroscopy and X-ray scattering techniques have come to conflicting results.[37–39] While the former suggests a less developed tetrahedral network in confined water,[36,37], the latter leads to conclusions of a more tetrahedrally arranged structure,[38,39] which is also in agreement with simulation studies.[19–21] However, focused X-ray scattering studies of water in PMOs with a broad selection of different pore diameters and organic moieties have not yet been conducted. The same is true for the investigation of ice structures, forming in these systems. This thesis aims to fill these gaps by using X-ray scattering on water under confinement in a broad selection of PMO materials. Investigations regarding the structure of liquid water and ice, the orientation of ice crystallites and the influence of water adsorption on the PMO material itself will be presented.

The thesis is structured in the following way. **Chapter 2** first gives an introduction into X-ray scattering and techniques based on it. The fundamental interactions of X-rays with amorphous and crystalline materials are discussed, along with the more sophisticated analysis method of X-ray cross-correlation analysis (XCCA). Then, some background is given on the properties of water and ice. In the last section, periodic mesoporous organosilicas (PMOs) are introduced and discussed as the host material for water. **Chapter 3** takes a closer look at the experimental methods including some brief information on the PMO synthesis and descriptions of the three X-ray scattering experiments at which the presented data were collected. The results of these experiments are then discussed in the following chapters. In **Chapter 4**, the structure of liquid water under confinement in PMOs is discussed. In the first section, a focus is set on the structure factor of the confined water, especially its peak positions. Then the pair distribution functions and running coordination numbers are investigated with a focus on their implications for the tetrahedral structuring of water. The structure and orientation of ice in PMOs is the topic of **Chapter 5**. First, the phases present in the pore, are analyzed before the lattice constants of the hexagonal contribution are determined. As it was found that deviations in the lattice constants do not always occur in all dimensions, the orientation of ice crystallites are probed using XCCA. The effect on water adsorption on the PMOs is investigated in **Chapter 6**. For this, the Bragg peaks associated with the periodicity of the organic moieties of the PMO are analyzed in relation to the relative humidity the material is exposed to. Finally, the results are summarized and put into a broader context in **Chapter 7**.

2 Background

This chapter aims to give a brief introduction into the topics relevant to this thesis. These are specifically the basics of X-ray scattering, the fundamental properties of water and ice, including their peculiarities in confinement, and finally some background on Periodic Mesoporous Organosilicas (PMOs) and their effect on water when confined in them.

On the topic of X-rays, the second edition of *Elements of Modern X-ray Physics* by Jens Als-Nielsen and Des McMorrow (2011)[40] serves as a resource, as well as one of the main sources for section 2.1. A starting point for further reading on the science and properties of water is the website *Water Structure and Science*, created and maintained by Martin Chaplin.[41] There, the current state of research of many aspects regarding water is summarized and a large number of references are provided that can be used for further research.

2.1 X-ray Scattering

X-rays are electromagnetic waves with typical wavelengths λ of 0.1 to 100 Å. As such, they can be described in a simplified way by their electric field

$$\mathbf{E}(\mathbf{r}, t) = \hat{\epsilon} E_0 \exp(i(\mathbf{k} \cdot \mathbf{r} - \omega t)), \tag{2.1}$$

where $\hat{\epsilon}$ is a unit vector describing the polarization of the electric field and $\mathbf{k}$ is its wave vector with $k = 2\pi/\lambda$ and $\hat{\epsilon}\cdot\mathbf{k} = 0$. The latter relationship holds because of the transverse nature of electromagnetic waves. $E_0 \exp(i(\mathbf{k} \cdot \mathbf{r} - \omega t))$ describes the variation of the field in space and time with E_0 being its amplitude. When an X-ray wave interacts with an atom, the electrons in the atom get excited by the X-ray beam and will then emit a wave with the same wavelength as the incidence wave. While the wavelength stays the same, a phase shift will occur between the incident and the emitted wave. When an X-ray interacts with an atom set in the origin and another at location $\mathbf{r}$, the phase shift $\Delta\phi$ at position $\mathbf{r}$ can be described as

$$\Delta\phi(\mathbf{r}) = (\mathbf{k} - \mathbf{k}') \cdot \mathbf{r} = \mathbf{Q} \cdot \mathbf{r}, \tag{2.2}$$

where $\mathbf{Q}$ is called the scattering vector, $\mathbf{k}$ is the incident wave vector and $\mathbf{k}'$ the scattered wave vector. This process, called elastic scattering, is visualized in Fig. 2.1. The quantity that is studied in X-ray scattering experiments is the scattered intensity I, which can be obtained from the number of counts per time recorded by a detector. It is proportional to the modulus squared of the electric field radiated from the scattering object $|\mathbf{E}_{\text{rad}}|^2$.

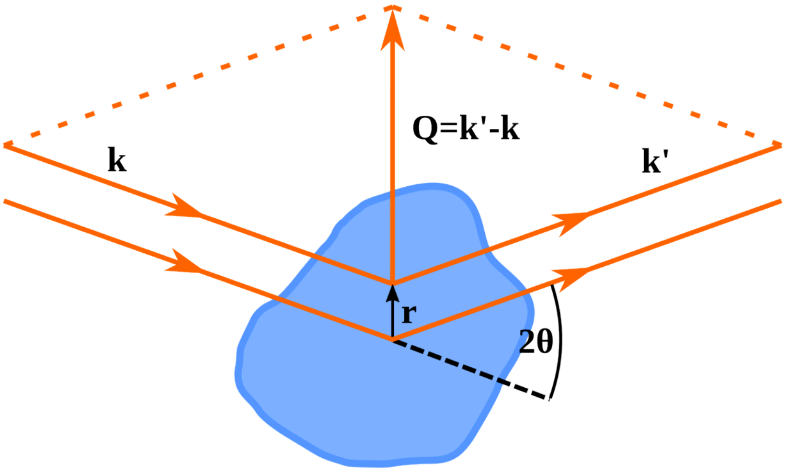

Figure 2.1: A visualization of scattering of an incident wave with wave vector $\mathbf{k}$ at the location $\mathbf{r}$. The resulting wave has a wave vector $\mathbf{k}'$ with $\mathbf{Q} = \mathbf{k}' - \mathbf{k}$,

2.1.1 Scattering from an amorphous material

When analyzing X-ray scattering data, one typically studies the intensity in relation to the momentum transfer $I(q)$, where q is the absolute value of the scattering vector $\mathbf{Q}$:

$$q = |\mathbf{Q}| = \frac{4\pi}{\lambda} \sin \frac{2\theta}{2}. \tag{2.3}$$

While historically, it was only possible to record this one dimensional quantity, nowadays two-dimensional detectors are available, which give access to many more aspects of the scattered light, such as angular orientation of crystals (see Section 2.1.3). Examples for 2D scattering patterns are shown in Fig. 2.2. From the 2D patterns, $I(q)$ is obtained by azimuthally integrating the intensity over the detector image.

For materials with short-range order, such as glasses or liquids, the integrated inten-

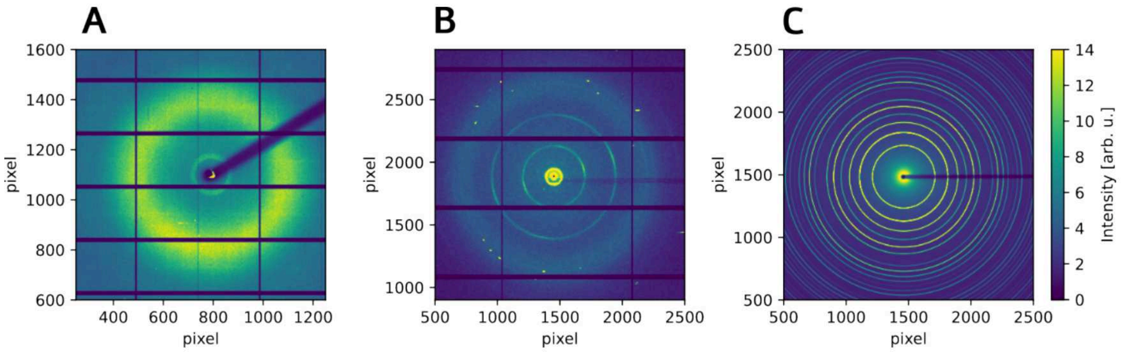

Figure 2.2: X-ray scattering patterns of an amorphous, a crystalline and a crystalline powder sample. **A** X-ray scattering pattern of polyimide, an amorphous material. **B** Scattering pattern of a crystalline material, specifically ice I in a periodic mesoporous organosilica. **C** Scattering pattern of a crystalline material as powder, in this case $\mathrm{LaB_6}$.

sity at a scattering vector $I(q)$ that gets scattered from a material has two contributions, namely the molecular form factor $f(q)$ and the liquid structure factor $S(q)$. Their relationship is given by

$$I(q) = S(q) \cdot N|f(q)|^2, \tag{2.4}$$

where N is the number of contributing scattering objects. $S(q)$ can be described as

$$S(q) = \frac{I(q)}{Nf(q)^2} = 1 + \frac{4\pi}{q} \int_0^\infty r[\rho(r) - \rho_a] \sin(qr)\mathrm{d}r, \tag{2.5}$$

with $\rho(r)$ describing the electron density at a given distance r from the origin and ρ_a being the average electron density. Eq. 2.5 indicates that $S(q)$ is described by a Fourier transform. If the Fourier transform is reversed, one arrives at the radial distribution function $g(r)$:

$$g(r) = 1 + \frac{1}{2\pi^2 r\rho_a} \int_0^\infty q[S(q) - 1] \sin(qr)\mathrm{d}q. \tag{2.6}$$

This real-space quantity describes the probability density of two scattering objects being separated by a distance r. This means that peaks in $g(r)$ correspond directly to the presence of coordination shells in the material (see Fig. 2.3B and C). Examples for the liquid structure factor and radial distribution function of water are shown in Fig. 2.3. In Fig. 2.3B, one observes a clearly defined first neighbour shell at $r_1 \approx 2.8\,\text{Å}$ and less pronounced peaks corresponding to the second and third coordination shells in the radial distribution function of bulk water.

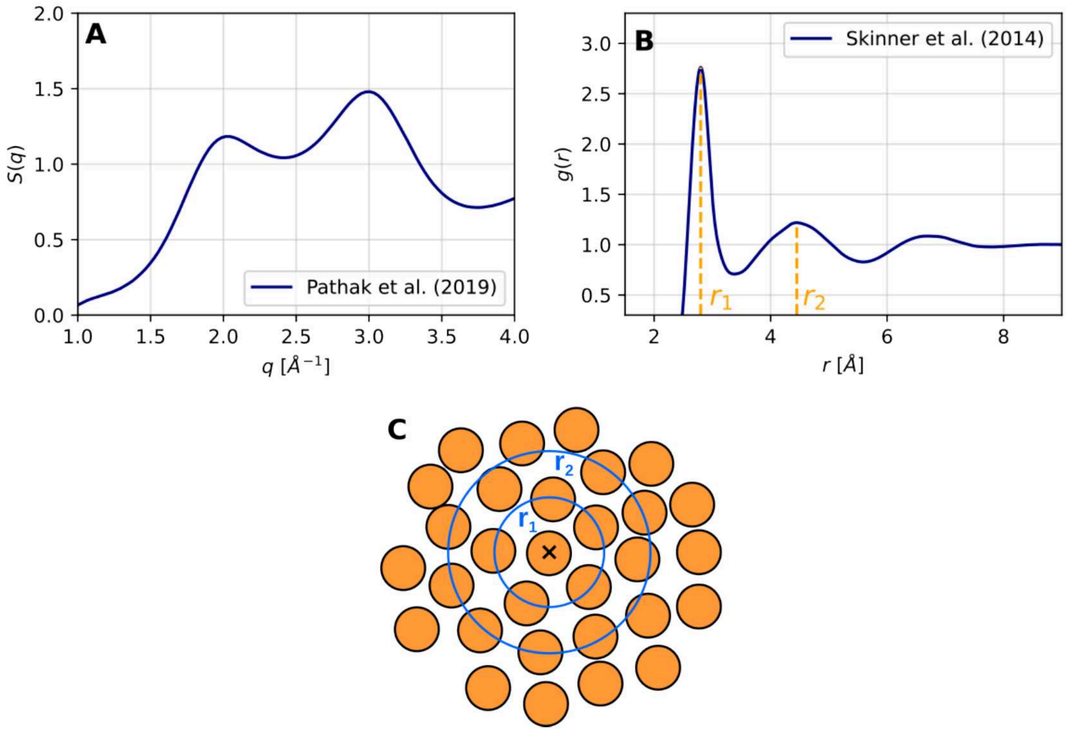

Figure 2.3: The liquid structure factor (**A**) and radial distribution function (**B**) of bulk water with indicated first and second hydration shells (r_1 and r_2). The data was obtained from Pathak *et al.*[42] (**A**) and Skinner *et al.*[43] (**B**) A 2D representation of the radial distribution function is shown in **C**.

2.1.2 X-ray scattering from a crystal

Let us now consider the case of a crystalline material. In a crystal, the X-rays emitted by the electrons will interfere at specific incident angles due to the periodic arrangement of the scattering objects. These angles can be determined by Bragg's law.

$$n\lambda = 2d \sin \frac{2\theta}{2}, \tag{2.7}$$

where n is the diffraction order and d is the spacing of the crystal lattice planes. This means that the X-ray scattering pattern of a single crystal consists of clearly defined spots at specific scattering angles, corresponding to the lattice planes at which the incident light was scattered. These are called Bragg reflections. This effect is visualized in Fig. 2.2B, where single crystal Bragg reflections are visible as spots at larger q. The pattern additionally shows an amorphous contribution from the silica, making up the bulk of the PMO host material (see Section 2.3).

The conditions for Bragg scattering can also be tested in reciprocal space. To do this, one overlays a sphere with its center in the origin and with radius k, the so-called Ewald sphere, with the reciprocal crystal lattice. If the Ewald sphere intersects with a reciprocal lattice point (hkl), this means that Bragg scattering occurs from the corresponding lattice plane. A 2D visualization of Bragg scattering in reciprocal space is shown in Fig. 2.4.

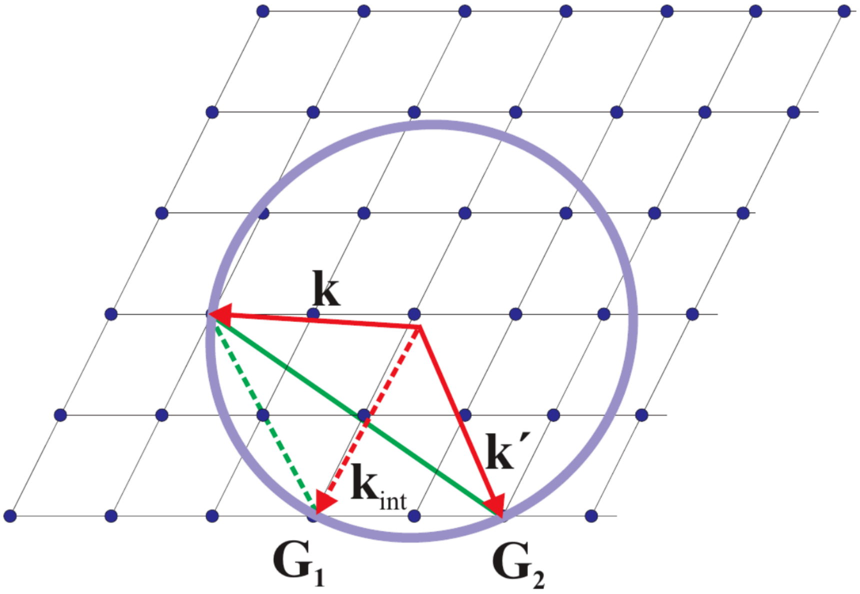

Figure 2.4: Visualization of Bragg scattering in reciprocal space. The Ewald sphere (violet) with radius k is overlayed over the reciprocal lattice (blue). Scattering will occur at points which intersect with the sphere. Reused from Als-Nielsen and McMorrow[40] with permission from *John Wiley & Sons*.

In many experiments, crystals are studied in the form of powders instead of single crystals. In these cases, the X-rays are scattered from many crystals with different orientations with the effect that their spots combine to rings visible on the detector, the so-called Debye-Scherrer rings. An example is shown in Fig. 2.2B, where rings from the organic moieties in the PMO host material are visible at smaller q, and in Fig. 2.2C, where the pattern of $\mathrm{LaB_6}$ powder is shown.

From the scattering angles at which spots or rings occur, one can draw direct conclusions on the arrangements of atoms and therefore the lattice structure. In order to define these structures, the lattice planes are described by Miller indices (hkl), which represent vectors normal to the planes. If the general structure of the crystal and the Miller indices of a specific peak are known, it is possible to calculate the lattice constants, *i.e.* the vectors defining a crystal unit cell. For the example of a hexagonally arranged crystal, such as hexagonal ice $\mathrm{I_h}$, this relationship can be described by

$$\frac{q^2}{4\pi^2} = \frac{4}{3}\frac{h^2 + hk + k^2}{a^2} + \frac{l^2}{c^2}, \tag{2.8}$$

where a and c are the two lattice constants of a hexagonal cell (cf. Fig. 2.5).

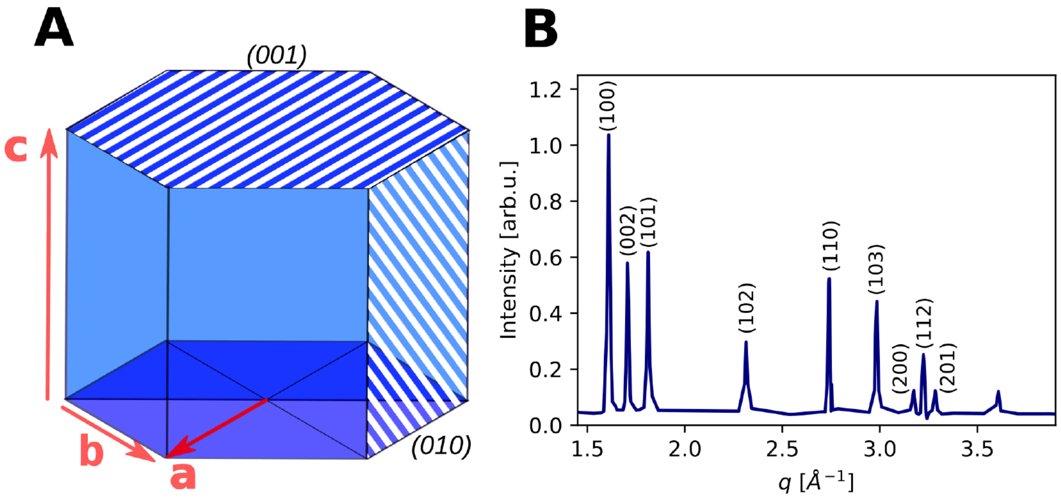

Figure 2.5: **A** Sketch of a hexagonal cell with the lattice vectors **a**, **b** and **c** marked in red. Note that **a** and **b** have the same absolute value and only differ in their directions. The (010) and (001) Miller planes are also indicated as examples. **B** Azimuthally integrated X-ray scattering pattern of a hexagonal crystal, in this case ice $\mathrm{I_h}$. The peaks are labeled with their respective Miller indices (hkl).

The width of a peak in the X-ray scattering signal is directly related to the size of the crystallite L on which the beam was scattered. The relationship can be described by the Scherrer equation:

$$L \approx \frac{K \cdot \lambda}{\Delta(2\theta) \cdot \cos\theta}, \tag{2.9}$$

with K being the Scherrer constant and $\Delta(2\theta)$ the full width at half maximum of the peak after taking into account instrument broadening. The equation implies that larger crystallites lead to narrower peaks in the scattering signal. Note that K depends strongly on factors such as the shape of the crystal and the orientation of scattering planes towards the crystal.[44,45]

2.1.3 X-ray Cross Correlation Analysis

It was mentioned in the previous section that the X-ray scattering pattern of crystalline materials consists of discrete spots at certain azimuthal angles ϕ and scattering vectors q. The latter serves hereby as a descriptor of the scattering plane while ϕ contains information on the orientation of the plane. Therefore, the angle $\Delta = \phi_2 - \phi_1$ between two spots directly describes the angle between the two scattering planes.[46,47] By applying this analysis, one can find preferred orientations of crystal structures in respect to themselves or other structures by analyzing a large amount of patterns this way. This is achieved by applying the correlation function

$$C(q_1, q_2, \Delta) = \frac{\langle I(q_1, \phi) I(q_2, \phi + \Delta) \rangle_\phi}{\langle I(q_1, \phi) \rangle \langle I(q_2, \phi) \rangle_\phi}. \tag{2.10}$$

A study of these functions is done in the framework of X-ray cross correlation analysis (XCCA).[46–51] Fig. 2.6 shows an example of how XCCA can be applied. It was taken from a study by Mukharamova *et al.*[47], which investigates the orientation of nanocrystals in respect to superlattices in which they are arranged. This is achieved by correlating the Bragg reflections of the atomic lattices of the nanocrystals to those of the superlattices, consisting of the nanocrystals.

Fig. 2.6(f-j) show the wide angle X-ray scattering (WAXS) patterns, relating to the nanocrystals, as well as the small angle (SAXS) pattern, which belong to the superlattices. Fig. 2.6(a-e) then show the correlation functions calculated from the patterns in Fig. 2.6(f-j). One observes several peaks, which correspond to the angles between the specified scattering planes of the nanocrystals and the superlattice. Real space visualizations are shown in Fig. 2.6(k-o). This study serves as an example how XCCA can be used to relate orientation of structures on different lengthscales by correlating Bragg reflections in the scattering pattern at different q. Note that XCCA is typically also applied at only one q-value ($q_1 = q_2$), *e.g.* in the crystallography of colloidal systems. Such systems posses poor crystalline qualities, which make it hard to deduce their structure from only their Bragg peaks.[46,48,52]

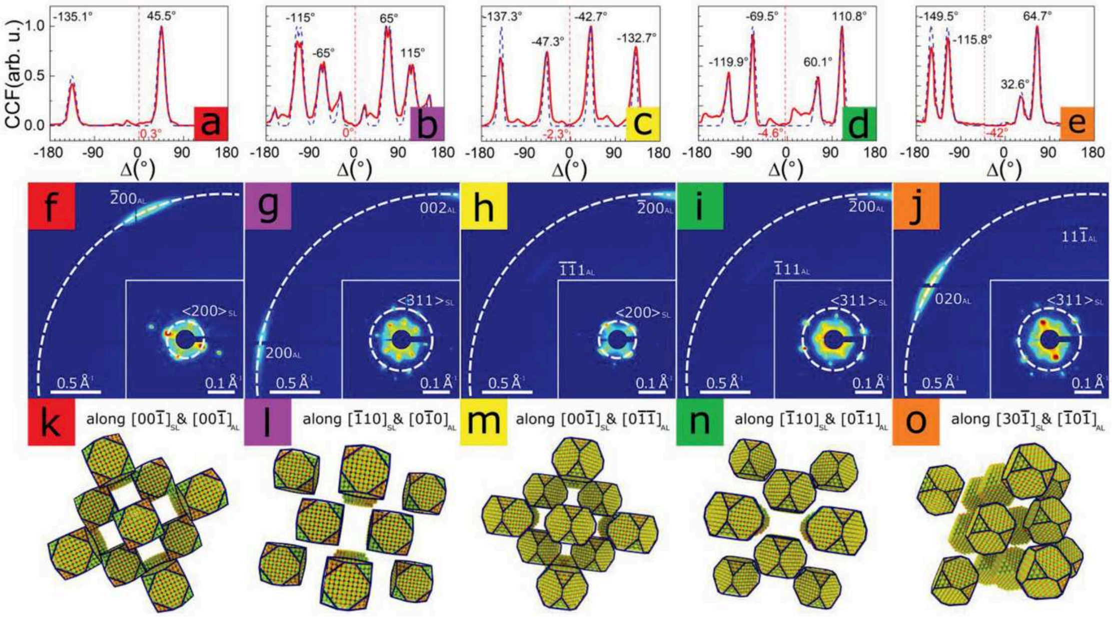

Figure 2.6: **(a-e)** Cross correlation functions calculated from the patterns in (f-j). **(f-j)** WAXS and SAXS (bottom right corner) patterns of nanocrystal superlattices. **(k-o)** Real space superlattice structures implied by (a-e). Figure originally published by Mukharamova *et al.*[47] in Small under CC-BY-NC-ND 4.0 license.

2.2 Water and Ice

Water is one of the most common materials on Earth, covering the majority of our planet's surface in the form of oceans, lakes, rivers, glaciers, *etc.*[1] It is also a necessary component for the emergence of life and makes up over two thirds of the mass of the human body.[2,3] However, despite the long history of water research, its properties are still relatively poorly understood with many behaviors and anomalies that would not be expected in a simple liquid.[4–9] A well-known example is the fact that water shows a density maximum at 4 °C, a temperature where it is present in its liquid state under ambient pressure, or the fact that its solid form, ice, generally possesses a lower density than the liquid.[6] More thermodynamic quantities where water shows anomalous behaviour, such as the isothermal compressibility, the isobaric heat capacity or the thermal expansion coefficient are shown in Fig. 2.7.[4] One observes that the deviation from how a simple liquid is expected to behave grows strongly in the case of supercooling, *i.e.* when the temperature is lower than T_m.

The solid form of water, ice, is also a very peculiar material with about 20 crystalline polymorphs[10,12] and at least three amorphous forms known at time of writing.[11,13]

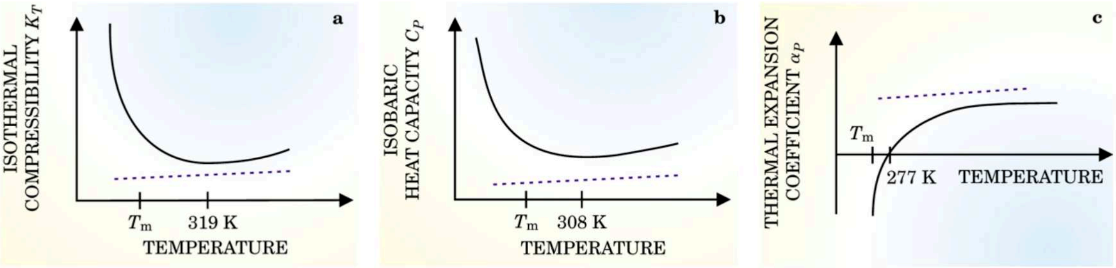

Figure 2.7: The isothermal compressibility K_T (**a**), The isobaric heat capacity C_P (**b**) and the thermal expansion coefficient α_P (**c**), each plotted against temperature, each shown for water (solid line) and a simple model liquid (dashed line). Reproduced from Debenedetti and Stanley[4] with permission from the *American Institute of Physics.*

2.2.1 Water Structure

Many of the properties and anomalies of water are related to its hydrogen bonding and by extension its tetrahedral structuring behaviour.[8,53] It is therefore of interest to examine the water molecule and its bonding in more detail.

A water molecule consists of an oxygen atom and two hydrogen atoms. The hydrogen atoms bond to the oxygen in such a way that they enclose an angle of about 104.5°,[54,55] meaning that the molecule as a whole is asymmetric. This leads to an anisotropic charge distribution with the side of the two hydrogen atoms being more positive and the opposite side more negative (see Fig. 2.8**A**), making water a polar molecule.[55] Two water molecules can then bond by the electropositive side of one molecule being attracted by the more electronegative side of the other. This is called hydrogen bond as the hydrogen serves as a connection between the two molecules.[55]

This way, each water molecule allows for four hydrogen bonds with neighbouring molecules. Typically, these tend to arrange tetrahedrally with one molecule in the center of the tetrahedron surrounded by its four hydrogen-bonded neighbours.[11,56–58] Such a tetrahedron is visualized in Fig. 2.8**B**. As water is a liquid and the molecules undergo constant thermal perturbation, these tetrahedral structures are very short-lived,

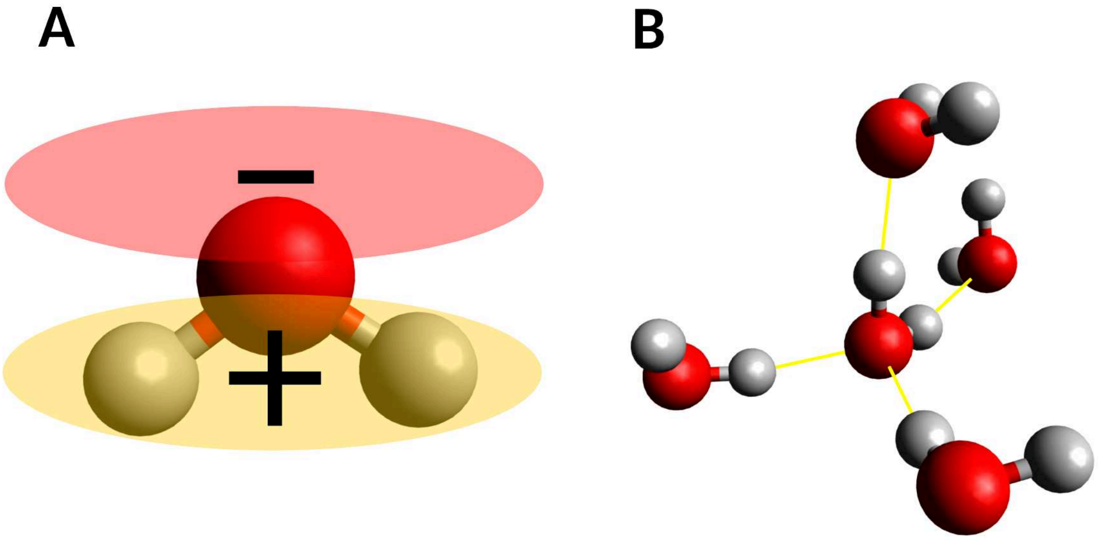

Figure 2.8: **A** Sketch of a water molecule, consisting of the oxygen atom (red) and the two hydrogen atoms (white). The more electronegative and -positive regions are marked in red and yellow, respectively. **B** Sketch of four tetrahedrally arranged water molecules with their hydrogen bonds marked in yellow.

fluctuating in and out of existence on timescale of picoseconds.[59]

When cooling down, the thermal fluctuations in the liquid reduce. As a consequence, the tetrahedral structures become more long-lived.[42,57] This can also be observed in the radial distribution function of supercooled water, where more defined coordination shells indicate a more structured, hydrogen-bonded network (see Fig. 2.9B). In the structure factor $S(q)$ of bulk water, this is reflected in a growth and spread of the two characteristic peaks in the region between 1.5 and 3.5 Å^{-1}, as illustrated in Fig. 2.9A.[42] Note that these structural changes coincide with more strongly pronounced anomalies in supercooled water (cf. Fig. 2.7).[4,53] It has been argued that this is due to the structural fluctuations in the H-bond network of water. Specifically, as the tetrahedrally arranged domains become more long-lived at lower temperatures, so do the more dense and more distorted parts of the network, allowing these domains to grow larger and more stable.[53] This could even imply the existence of a liquid-liquid critical point and therefore two distinct forms of liquid water, i.e. low and high density liquid water (LDL and HDL, respectively).[6,8,53,60] This heterogeneity, which becomes more pronounced in supercooled water, is suspected to be the cause of many of the anomalies of water and subject to current research.[6,53]

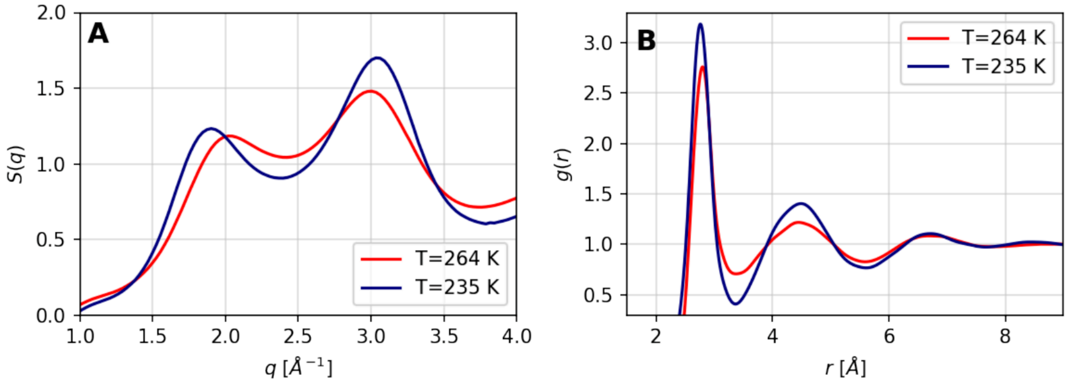

Figure 2.9: Structure factor (**A**) and radial distribution function (**B**) of bulk water at 264 and 235 K. Data is obtained from Pathak *et al.*[42]

2.2.2 Ice and Ice phases

Water has a very complex phase diagram, especially when one considers ice, its solid form.[10,12] Ice has around 20 different crystalline polymorphs known to date, in which the oxygen atoms are ordered. The hydrogen atoms may be ordered or not depending on the polymorph in question.[12] Additionally, water can also take amorphous solid forms called amorphous ices. There are at least three different forms of amorphous ices, namely low, high and very high density amorphous phases[11,13] with a recent report proposing the existence of a fourth form called medium-density amorphous ice.[61]

The most common form of ice in everyday life is called ice I, as it was the first one known to humans. When more and more phases of ice were discovered, forming at different pressure and temperature regimes, these were numbered using Roman numerals, leading to the naming of ice II, ice III *etc.*[10,12,62,63]

Ice I is subdivided into phases called hexagonal ice (ice I_h) and cubic or stacking disordered ice (ice I_c or I_{sd}). Ice I_h is the structure that ice takes when it crystallizes at around 0 °C under atmospheric pressure and is therefore the most familiar one in everyday life. The oxygen atoms in its first coordination shell are arranged tetrahedrally and form six-membered rings on a larger range.[64] Ice I_c is generally very similar to ice I_h, the difference is that the stacked crystal layers are shifted horizontally in ice I_h.[64–66] The X-ray scattering patterns of the ice I polymorphs are shown in Fig. 2.10A.

The ambiguity in the nomenclature of ices I_c and I_{sd} comes from a shift in the naming conventions. Previously, the phase was considered as cubic ice, first described by Hans

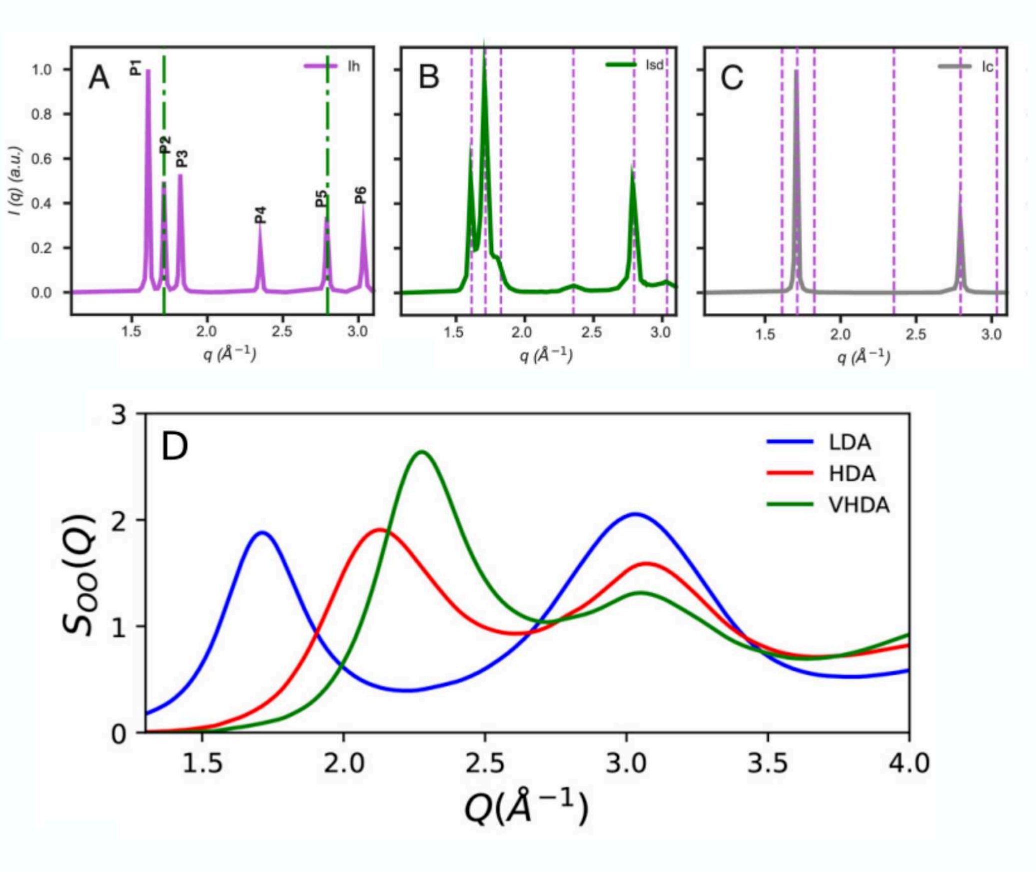

Figure 2.10: X-ray scattering signals of ices I_h (**A**), I_{sd} (**B**) and I_c (**C**). The green dash-dotted line in A represents the peaks of I_c, the pink dashed lines in B and C show the location of the peaks of I_h, which have previously been indicated in Fig. 2.5. **A-C** are adapted from Ladd-Parada, *et al.*[13] **D** X-ray scattering signals of low (blue), high (red) and very high density (green) amorphous ices. Reused from Mariedahl *et al.*[11]. Both originally published under CC-BY 4.0 license.

König in 1943.[67] However, more recent studies argue that this phase does not resemble pure cubic ice, which has only been achieved recently in 2020.[66] Instead, the structure is made up of crystals with alternating hexagonal and cubic layers or domains.[65] As the ratio of cubic to hexagonal layers can vary, stacking disordered ice does not have one characteristic diffraction pattern but can show different degrees of cubic and hexagonal peaks with varying relative peak intensities.[65] An example of an ice I_{sd} X-ray scattering pattern is shown in Fig. 2.10B and Fig. 2.11 shows illustrations of the lattice plains of ices I_h, I_c and I_{sd}.

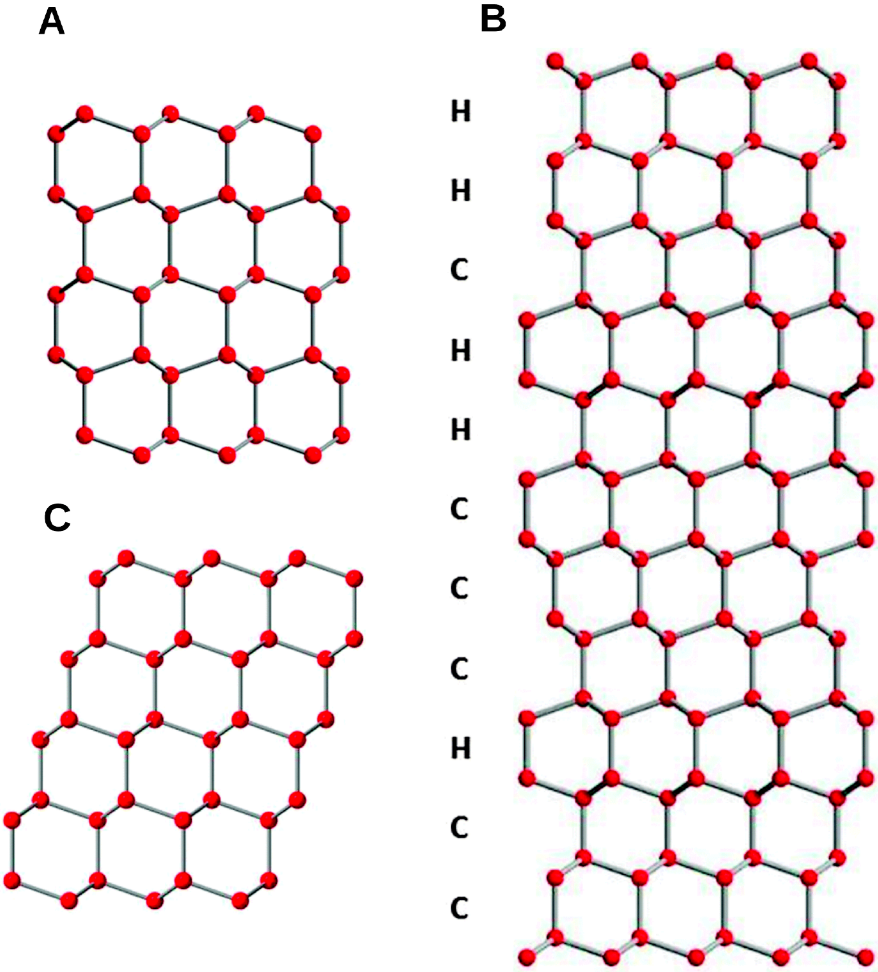

Figure 2.11: Sketches of the lattice planes of ices I_h (**A**), I_c (**B**) and I_{sd} (**C**). Hexagonal and cubic layers are indicated by H and C in the latter. These figures were previously published by Malkin *et al.* in *Physical Chemistry Chemical Physics*[65] under CC-BY 3.0 license.

The amorphous ices can be understood as glassy states of water, meaning that they are a solid form of water but possess an amorphous structure.[11,68] This means that sharp peaks such as in Fig. 2.10A-C, cannot be observed in their XRD patterns as these stem from long-range crystalline order. As shown in Fig. 2.10D, amorphous ices instead lead to broader peaks that are related to short- to mid-range order, *i.e.* an order on a range of only few atoms.[11] As the names imply, the three (or four) forms of amorphous ice represent amorphous forms with different densities. These amorphous ice form differ in the structural arrangement of the water molecules. LDA possesses a tetrahedral structure. In contrast to liquid water, the tetrahedrons exist stably and do not fluctuate in and out of existence. HDA consists of tetrahedrons with an interstitial water molecule inside the tetrahedron that is not hydrogen-bonded to the central molecule, while in VHDA, two such interstitial molecules are present[68,69].

2.2.3 Water and ice under confinement

When water is subject to spatial restrictions, the structure of its network is influenced and its equilibrium and dynamical properties vary.[14–17] For example, the freezing and melting point of water is lowered by confinement in pores of <100 nm in dependence of the pore diameter, *i.e.* water freezes at colder temperatures for smaller pore diameters.[18,70–72]

However, not only the pore diameter influences the properties of confined water but also the interaction between the water and the pore. It has for example been established that in a hydrophilic pore, the density of confined water is not homogeneous throughout the pore cross section.[19,20,73,74] Specifically, the two to three layers of water molecules adjacent to the pore wall show a higher density than bulk water, while the density of the next couple of layers towards the pore center is lower than bulk. Going further towards the center of the pore, the density approaches the value of bulk water. However, considering the entire pore cross section, the average density is in fact lower than bulk water.[20,21] This effect is highlighted in Fig. 2.12A, which shows the simulated density profile of water in a MCM-41 nanopore, which is probably due to the hydrophilic pore wall leading to the formation of a meniscus at the opening of the pore. This induces a negative pressure on the confined water and thus decreases the density.[21] Additionally, in silica pores, oxygen from the water network might adsorb into the pore wall, resulting in an overlap of water and the pore wall with no clear boundary between the two.[19,21,73]

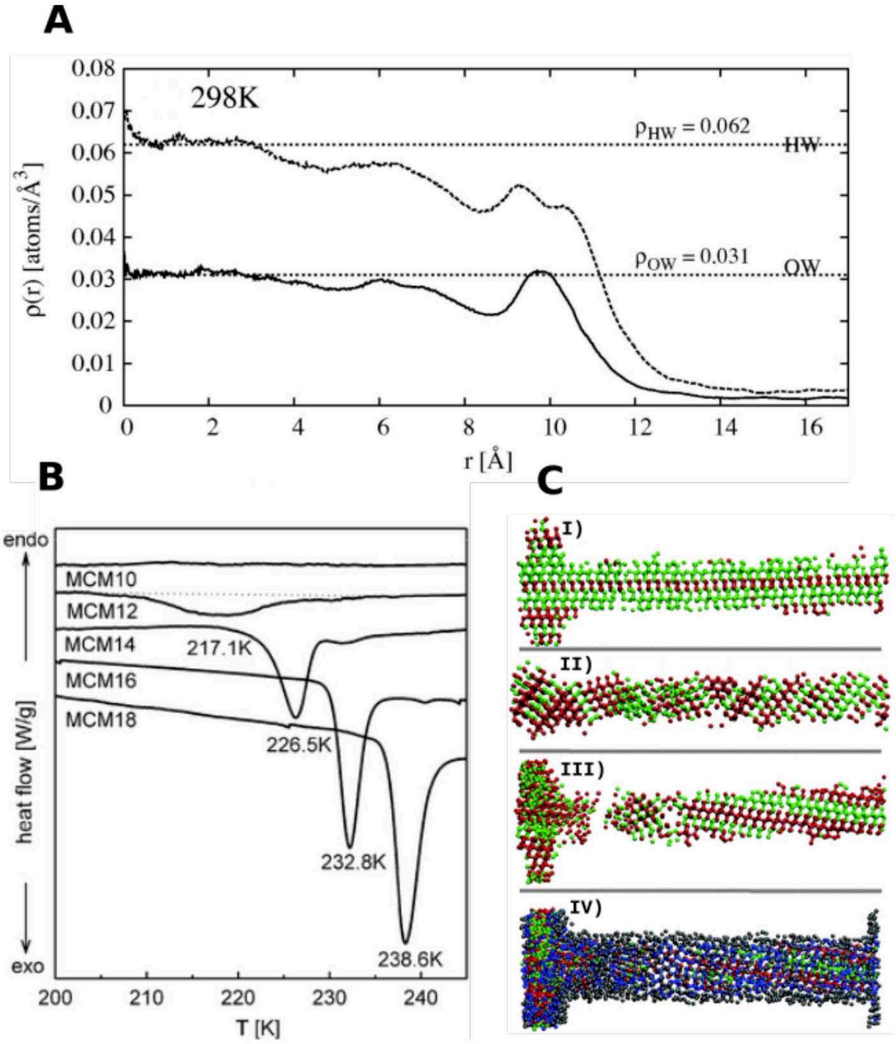

Figure 2.12: **A** The density profile of water in a MCM-41 nanopore at 298 K. The top line shows the density of hydrogen atoms while the lower line shows that of oxygen atoms. The figure was originally published by Alan K. Soper in *Chemical Physics Letters*[21] under CC BY-NC-ND 3.0 license. **B** Differential scanning calorimetry (DSC) measurements of D_2O in MCM-41 materials with pore diameters between 4.5 (MCM18) and 2.5 nm (MCM10). Previously published by Jähnert et al.[18] in *Physical Chemistry Chemical Physics* and reused with permission from The Royal Society of Chemistry. **C** Nanoconfined ice with different stacking configurations of cubic (red) and hexagonal (green) domains (I-III). IV additionally shows interfacial ice (blue) and non-freezing liquid water (grey). Previously published by Moore et al.[22] in *Physical Chemistry Chemical Physics* and reused with permission from The Royal Society of Chemistry.

Studies considering the molecular structuring of water under nanoscale confinement have previously been conducted, using methods such as X-ray and neutron scattering[38,39,75], as well as Raman spectroscopy[36,37]. There are also a number of simulation studies on the topic[19–21]. However, authors employing different methods arrive at varying conclusions, in particular in regards to the effect of confinement on the amount of tetrahedral structuring. Crupi *et al.*[37] and Malfait *et al.*[36], for example, found a decrease in strongly hydrogen-bonded, tetrahedral structures in the confined water, while previous studies using scattering techniques observed an increase of these structures[38,39]. Simulation studies, for example by Soper *et al.*[20,21] also found an increase of tetrahedrally structured water under confinement.

Considering ice in confinement, spatial restrictions and interface interactions also strongly influence the formation and structure of ice. Generally, the spatial restrictions lead to a lower freezing temperature when compared to bulk ice.[18] This is shown in Fig. 2.12B with differential scanning calorimetry (DSC) measurements for D_2O in MCM-41 materials with different pore diameters. The freezing temperatures can be assessed by the poition of the peaks in the DSC data. With decreasing pore size, freezing occurs at lower temperatures until the material with the smallest pores, MCM10, does not show any visible freezing peak. Another property of ice in confinement is the presence of a non-freezing layer of liquid water between the pore wall and the crystalline ice, which has been consistently observed in ice in nanopores.[72,76–78]

While the default ice phase in bulk ice under atmospheric conditions is ice $\mathrm{I_h}$, nanoconfined ice tends to form stacking disordered ice $\mathrm{I_{sd}}$. As explained in section 2.2.2, this phase consists of alternating cubic and hexagonal layers or domains.[65] Fig. 2.12C shows different ways how these layers could arrange when confined in a nanopore with Fig. 2.12C IV also showing the previously mentioned non-freezing water.[22,72]

The thickness of this non-freezing layer can be put into relation with the melting temperature of ice in confinement T_m to the pore radius R and the thickness of the non-freezing water layer D via a modified Gibbs-Thompson equation[23] as

$$T_\mathrm{m} = T_\mathrm{m}^\mathrm{bulk} - \frac{K_\mathrm{GT}}{R - D}, \tag{2.11}$$

where $K_\mathrm{GT} = 53 \pm 1\,\mathrm{K\,nm}$ is the Gibbs-Thompson coefficient and $T_\mathrm{m}^\mathrm{bulk} = 273.15\,\mathrm{K}$ the melting temperature of bulk water.

2.3 Periodic Mesoporous Organosilicas

In order to investigate the influence of different parameters on the structure of confined water and ice, its structure in materials with varying pore diameter and pore wall chemistry is analyzed. This can be achieved by the use of periodic mesoporous organosilicas. These are a class of hybrid material consisting of SiO_2 with periodically arranged organic moieties in the pore walls, forming a crystal-like wall structure.[24–31] The organic moieties can furthermore contain functional components of various kinds, which can influence the interaction between the pore walls and the confined material.[33,34] PMOs provide a high stability due to the inorganic part and at the same time a wide variety of possible functionalities in the organic bridging unit and can therefore be tuned to various intended applications, such as catalysis,[79,80] drug delivery[81,82] or light harvesting.[83–85]

In this thesis, a notation is used that identifies the various PMOs by their precursor followed by their pore diameter in brackets. For example, BTEB(3.8) denotes a PMO based on a 1,4-bis(triethoxysilyl)benzene (BTEB) precursor with a pore diameter of 3.8 nm. For the chemical structures and full designations of the precursors, please refer to Fig. 3.1 in the following chapter. Note that in previous publications, different notations were used, *e.g.* B instead of BTEB or DVA instead of BTEVA.[31,34,35]

2.3.1 Structure and properties

Fig. 2.13A shows an illustration of a PMO material. One observes the periodic, hexagonal arrangements of the pores, which lie parallel to each other.[24,31,32] The organic moieties in the pore wall are represented by light blue ellipsoids. Their arrangement leads to a structure in the pore wall, that alternates between silanol and the functional group of the PMO in question[24] (see Fig. 2.13B and C).

Especially Fig. 2.13B shows how the pore wall functionalization in PMOs does not lead to a uniformly altered interaction with the water. Instead, it is localized at the functional groups. In this example, the areas of the hydrophobic benzene groups show less interaction with the water than the hydrophilic silanol groups. In contrast, Fig. 2.13C shows a hydrophilically functionalized BTEVA-PMO, where the pore wall-water the interaction looks more uniform.

It is to note that the estimation of hydrophilicity or hydrophobicity is not trivial due the alternating nature of the functionalization and the curvature of the pore wall. A number of techniques exist that partially give different results for the same materials.[86–88]

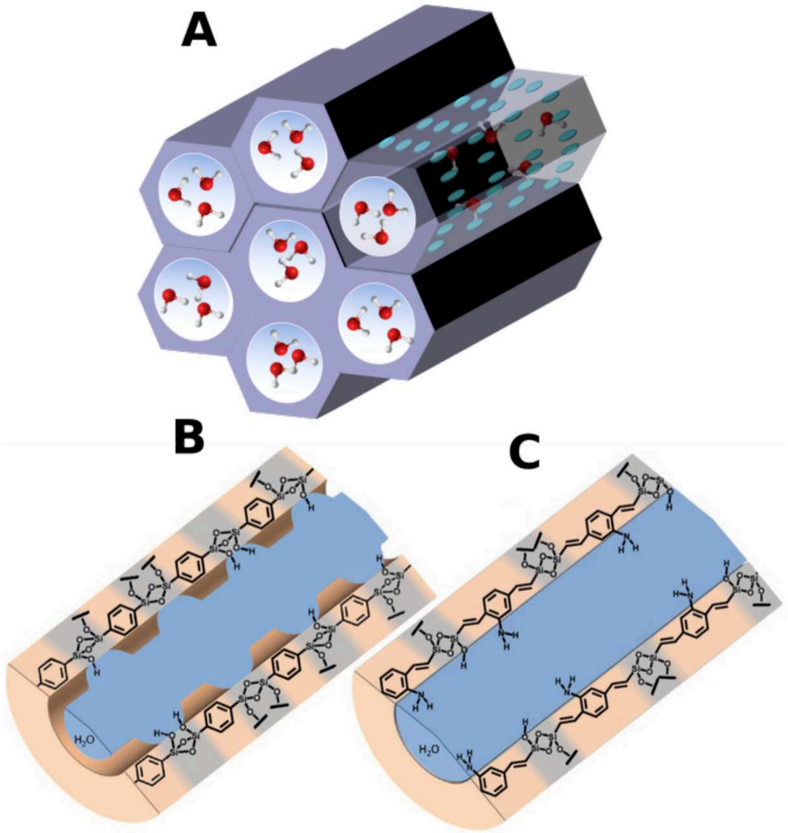

Figure 2.13: **A** Sketch of a hexagonally ordered PMO material. The organic moieties are symbolized by the light blue ellipsoids. **B** Sketch of a PMO pore from the BTEB precursor. **C** Sketch of a pore from the BTEVA precursor. For an explanation of the PMO precursors and their nomenclature, Section 3.1. **B** and **C** are reused with permission from *Wiley and Sons*.[32]

A more detailed discussion of the estimation of hydrophilicity for samples mentioned in this thesis is given in Sec. 3.1.1.

The periodic arrangements of the organic moieties in the pore wall is reflected in a distinct X-ray scattering signal of PMOs. Figures 2.14B and C show the small and wide angle scattering signals of BTEVA(3.8). The peaks that are found in the small angle regime can mainly be attributed to the reflections from the ordering of the pores, *i.e.* $(hk0)$, while those in the wide angle regime stem from the periodicity of the organic moieties inside the pores *i.e.* $(00l)$. Note that the angle at the highest q ($\approx 0.53\,\text{Å}^{-1}$) in Fig. 2.14B is the same as the peak at the lowest q in Fig. 2.14C, signifying the overlap of the two regimes.

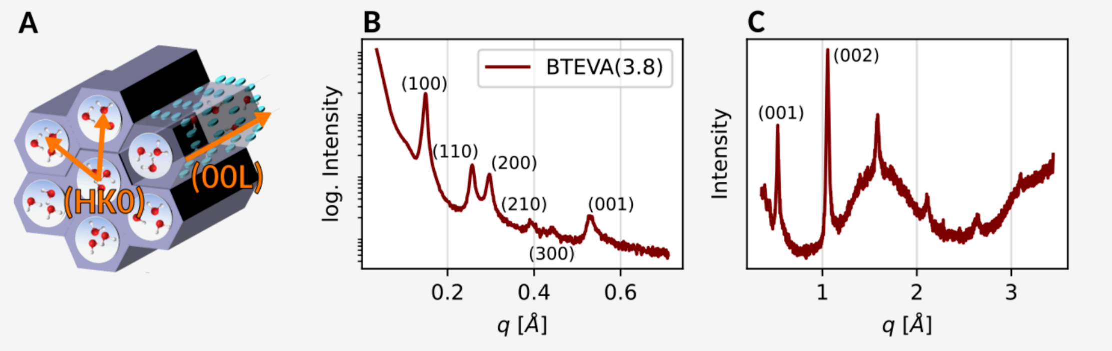

Figure 2.14: **A** Sketch of a PMO material with indicated Miller indices of the PMO scattering directions. **B** and **C** show the small and wide angle X-ray scattering signals of BTEVA(3.8), respectively. The Miller indices of the various peaks are indicated. All peaks in **C** refer to $(00l)$ peaks. Here, only the first two are indicated. Note that **B** is plotted with a logarithmic scale for the intensity, while that in **C** is linear.

2.3.2 Water in PMOs

Due to the altered interaction with the pore wall, the behaviour of water in PMOs has been of great interest with a number of studies having been conducted on the topic in recent years.[32–36] It has generally been established that not only the pore diameter but also the pore wall functionalization contributes to confinement effects of water and that these differ from pure silica materials with comparable pore sizes.[31,32]

For example, the dynamics of water close to the pore wall are drastically slowed down in hydrophilically funtionalized pores compared to hydrophobic ones.[34] This is illustrated in Fig. 2.15, which shows the diffusion coefficient and resident time of interfacial water in different PMOs, as well as MCM-41, extracted from quasi elastic neutron scattering (QENS) measurements by Jani *et al.*[34] In Fig. 2.15a, one observes a diffusion coefficient that is lower than that of bulk water for all porous media studied, *i.e.* MCM-41, a hydrophobic DVB-PMO and a more hydrophilic DVA-PMO. Note that DVB and DVA correspond to BTEVB and BTEVA in the notation of this thesis, respectively. Between these, the hydrophobic PMO shows more bulk-like behaviour while the hydrophilic MCM-41 and DVA-PMO show lower diffusion coefficients. Fig. 2.15b shows the residence times of interfacial water molecules in the previously mentioned materials. Here, the difference to bulk water becomes even more pronounced. The plot also shows the residence times of water in a completely filled pore, which lie between bulk and interfacial water. It can therefore be concluded that the dynamics in interfacial, confined water are considerably slowed down in comparison to bulk water.[34]

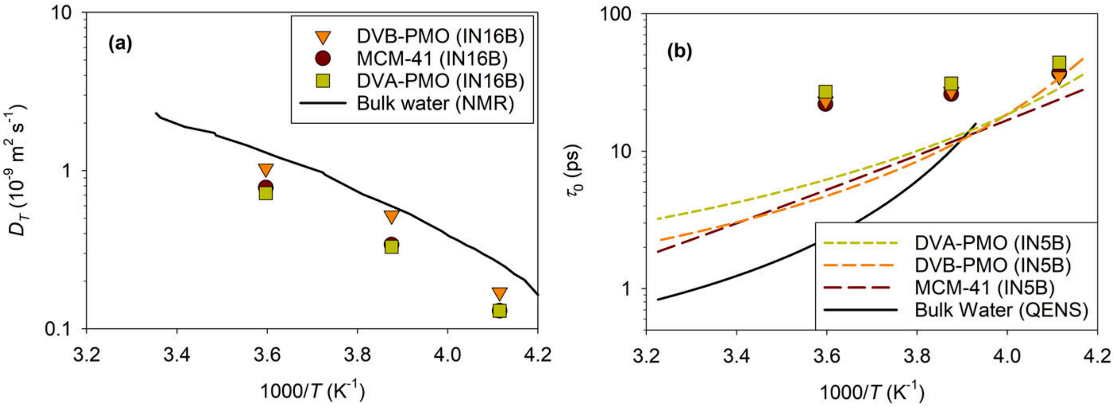

Figure 2.15: Diffusion coefficient (**a**) and residence times (**b**) of interfacial pore water in DVB-PMO, DVA-PMO and MCM-41. Reused from Jani *et al.*[34] with permission from the *American Institute of Physics.*

Furthermore, it was shown that liquid water still present even at temperatures much lower than the freezing temperature.[35] This can be explained by the presence of a non-freezable water layer, which is known to exist in non-functionalized water-filled pores.[22,72,89] Fig. 2.16A shows results of a dielectric relaxation spectroscopy study by Malfait *et al.*[35], where water in various PMOs was studied below the freezing temperature. Three distinct processes were observed. First, there is the Maxwell-Wagner-Sillars process, which is connected to the heterogeneity of the host medium.[35,90] The two other processes are those of ice and the interfacial water in the pore. The presence of the latter indicates the existence of interfacial water in PMOs, which is also illustrated in Fig. 2.16B.

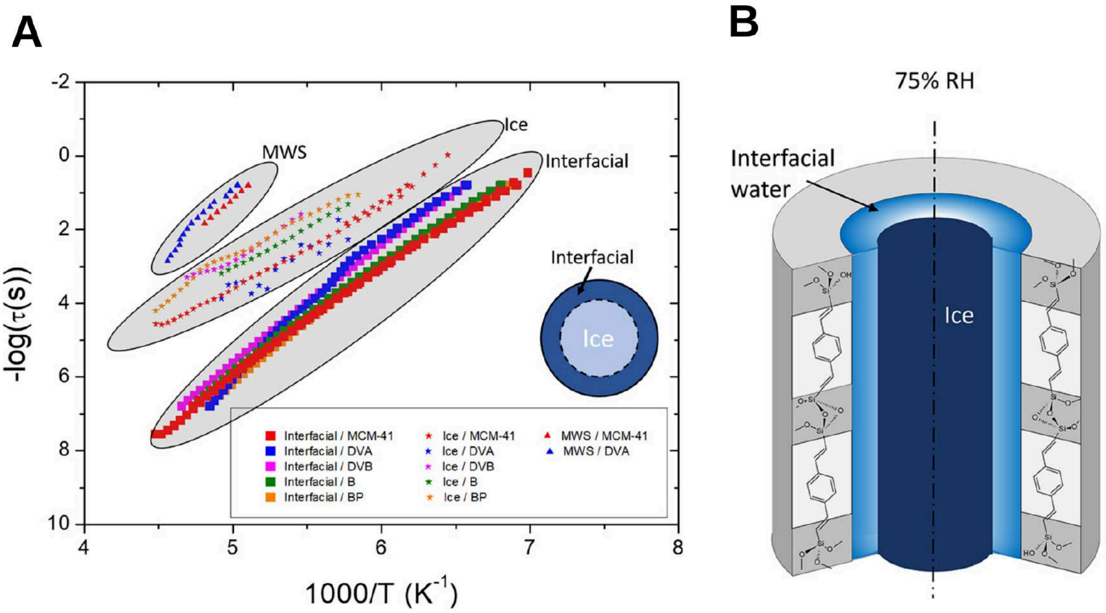

Figure 2.16: **A** Temperature dependence of relaxation times of the Maxwell-Wagner-Sillars (MWS), ice and interfacial processes of water confined into the five matrices: MCM-41, DVA, B, BP and DVB with 75 % pore filling. **B** Illustration of ice and interfacial water in a PMO. Adapted from Malfait *et al.*[35] with permission from the *American Chemical Society.*

Another study by Malfait *et al.*[36] found that water in PMOs has a less pronounced tetrahedral structure compared to bulk water, at least in PMOs, which is functionalized with benzene. Fig. 2.17A shows Raman spectra of water confined in MCM-41. The three contributions, tetrahedral, distorted and free water, are indicated and their contributions plotted in Fig. 2.17B. Here, the tetrahedral contribution is lower than in the spectrum of bulk water, while the free and distorted contributions are lower. Fig. 2.17C-F then compare the spectrum of MCM-41 with that of a B-PMO (BTEB in this thesis, see Sec. 2.3). It is found that the interpolated water signal in the B-PMO is more or less similar to that in MCM-41. From that it is concluded that the tetrahedral contribution in BTEB should also be lower compared to bulk water. However, only water in B-PMO was investigated in this study, therefore the amount of tetrahedral structuring in other PMOs can not be inferred from these results. Furthermore, the relevant section of the Raman spectrum is overlayed by peaks from the PMO material, making the interpolation of the water signal non-trivial.

The freezing and melting points of water are also interesting quantities to study in confinement. It has generally been established that confinement leads to lower freezing and melting points when compared to bulk water (see Section 2.2.3). Fig. 2.18 shows the freezing and melting points for water confined in MCM-41 (Fig. 2.18A), B- and BP-PMOs (Fig. 2.18B), as well as DVB- and DVA-PMOs (Fig. 2.18C), determined by Mietner[31] using DSC. One observes a dependence on the pore diameter in each of the materials. However, this dependence is also strongly related to the material with MCM-41 showing the strongest dependence on pore diameter.

This thesis aims to add to the knowledge about water in PMOs using of X-ray scattering methods. Specifically, the structure of liquid water and ice confined in PMOs with different functionalizations and pore diameters will be investigated. This is of particular interest, considering the conflicting conclusions from the the results presented in Fig. 2.17 and those discussed in Section 2.2.3. In the latter, a more tetrahedrally structured network has been suggested for water in pure silica nanopores using simulation and scattering methods[20,21,38]. In contrast, the results of Malfait *et al.*[36] hint at less tetrahedral water in PMOs and are therefore in agreement with other spectroscopy studies on pure silica materials.[37] This thesis aims to contribute to this discussion with large scale X-ray scattering studies on the structure of water and ice under confinement in a broad selection of PMOs.

The precise procedures and experiments, as well as the list and properties of the used PMOs, are discussed in the following chapter.

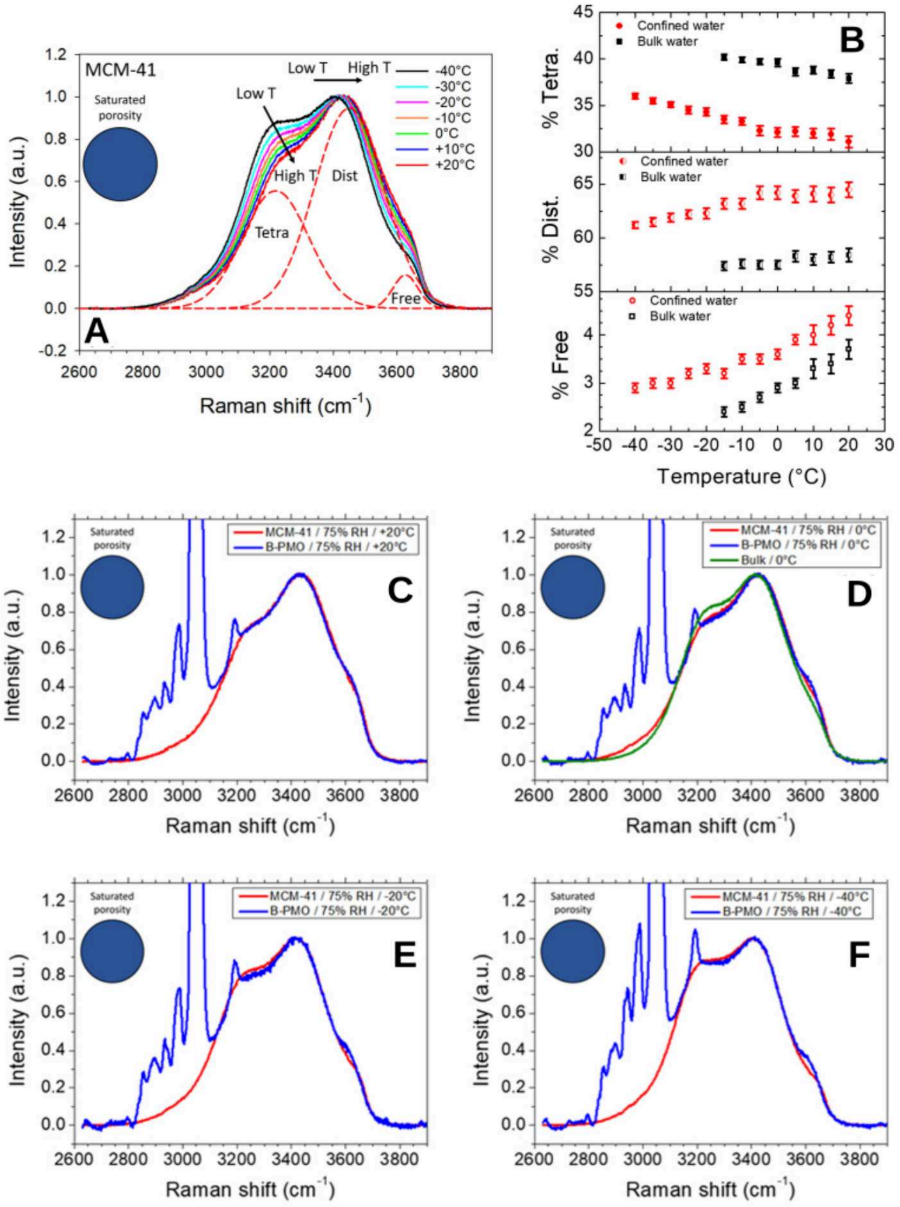

Figure 2.17: Results of Raman spectroscopy on water in a B-PMO, conducted by Malfait *et al.*[36] **(a)** Spectra for temperatures between +20 and −40 °C. The tetrahedral, distorted and free water contributions are indicated. **(b)** Contributions of tetrahedral, distorted and free water to the Raman spectrum of the confined water, as well as bulk water. Reused with permission from the *American Chemical Society*.

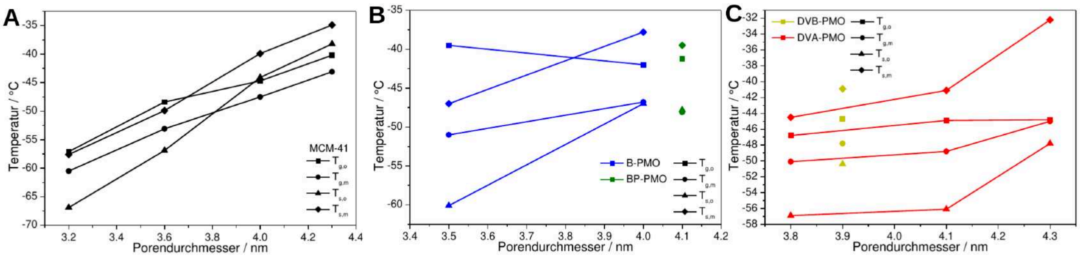

Figure 2.18: Freezing and melting temperatures for water confined in MCM-41 (**A**), B- and BP-PMOs (**B**), as well as DVB- and DVA-PMOs (**C**) with different pore diameters (*"Porendurchmesser"*) from Differential Scanning Calorimetry (DSC). For each material, both the temperatures determined from the onset (freezing: $T_{g,o}$, melting: $T_{s,o}$) and the maximum ($T_{g,m}$, $T_{s,m}$) of the DSC peak are plotted. Adapted from the dissertation of J. B. Mietner *"Zu Gast in Nanoporen"*.[31]

3 Experimental Work

In the course of this work, three main X-ray scattering experiments were conducted, which will be referenced throughout the rest of the manuscript. They were performed at the P02.1, P03 and P21.1 beamlines of the PETRA III facility at Deutsches Elektronen-Synchrotron DESY in Hamburg, Germany. In the first experiment, powder X-ray scattering was conducted on water and ice in PMOs. The aim of the second one was to assess orientations of ice crystals in PMOs using X-ray Cross Correlation Analysis (XCCA) and the last was an in-situ study of the water-filling process of the PMO materials. In this chapter, the synthesis and properties of the PMOs used, as well as each of the experiments will be described in further detail.

3.1 Porous materials

Table 3.1 shows a list of the porous materials used in the studies to be discussed. The samples represent a selection of various pore diameters between 4.9 and 3.4 nm. The nitrogen and water vapor adsorption isotherms, as well as the pore size distributions and the chemical structures of the respective precursors of the materials are shown in Fig. 3.1. The materials were provided by the Institute of Inorganic and Applied Chemistry at the University of Hamburg (AG Fröba). Therefore, please refer to previously published articles for a more detailed description of the process.[91,92] To briefly summarize, the synthesis of the BTEVB,[31,93] BTEVA[31] and BTEVFB[29,93] precursors and their reaction to the corresponding PMOs were carried out according to the synthesis instructions given in literature. The synthesis of the BTEVP precursor is a modified form of literature synthesis.[28] Deviating from the general three-step synthesis in the second step, the preparation of 2,5-diethynylpyridine, was carried out in a modified way.[94] The charge in BTEVP+ samples was introduced afterwards using a postsynthetic pathway, where it was exposed to iodomethane over two days.

In the experiments explained in Sections 3.2 and 3.3, the water was adsorbed into the

	Precursor	$\boldsymbol{d}_{\mathrm{P}}$ [nm]	$\boldsymbol{V}_{\mathrm{P},0.9}$ [cm^{3}g^{-1}]	$\boldsymbol{d}_{\mathrm{org}}$ [nm]	$\left(\frac{\mathbf{p}}{\mathbf{p_0}}\right)_{\mathrm{onset}}$	**Exp.**
■ MCM-41(3.9)	MCM-41	3.9±0.3	0.85	-	0.52	1
✚ BTEB(3.8)	BTEB	3.8±1.1	1.26	0.76	-	1,3
BTEVB(3.8)	BTEVB	3.8±0.7	0.54	1.19	0.75	1,2
● BTEVFB(4.9)	BTEVFB	4.9±1.4	0.83	1.20	-	1
► BTEVFB(4.4)	BTEVFB	4.4±0.7	1.04	1.20	0.88	1
⬟ BTEVFB(3.8)	BTEVFB	3.8±0.4	0.61	1.18	-	2,3
▲ BTEVA(4.4)	BTEVA	4.3±0.3	0.83	1.18	-	1,3
◄ BTEVA(3.8)	BTEVA	3.8±0.4	0.67	1.18	0.67	1,2,3*
◆ BTEVA(3.4)	BTEVA	3.4±0.4	0.64	1.18	-	1
⬣ BTEVP(4.4)	BTEVP	4.4	-	-	-	3
BTEVP(3.8)	BTEVP	3.8±0.7	0.87	1.19	-	2
✖ BTEVP(3.5)	BTEVP	3.5±0.8	0.63	1.19	0.56	1,3
BTEVP+(3.5)	BTEVP+	3.5±0.5	0.47	1.18	-	2
● BTEVP+(3.4)	BTEVP+	3.4±0.6	0.60	1.18	-	1
BTEVCl(3.8)	BTEVCl	3.8±0.8	0.93	1.19	-	2
★ BTEV[B:FB]](3.8)	BTEV[B:FB]	3.8	-	-	-	3

Table 3.1: List of porous materials used in the experiment. Shown are the precursors used for the PMO synthesis, the pore diameter d_{P} (where the uncertainty is given by the half width at half maximum of the pore size distribution), the pore volume at 90 % relative pressure $V_{\mathrm{P},0.9}$, the organic unit periodicity d_{org}, the onset of the water adsorption isotherm $\left(\frac{\mathbf{p}}{\mathbf{p_0}}\right)_{\mathrm{onset}}$ and the experiment in which the sample was used (1 = P02.1, 2 = P03). * Two different batches of BTEVA(3.8) were used in the Exp. 1 and Experiments 2 and 3 but their properties did not show any notable differences.

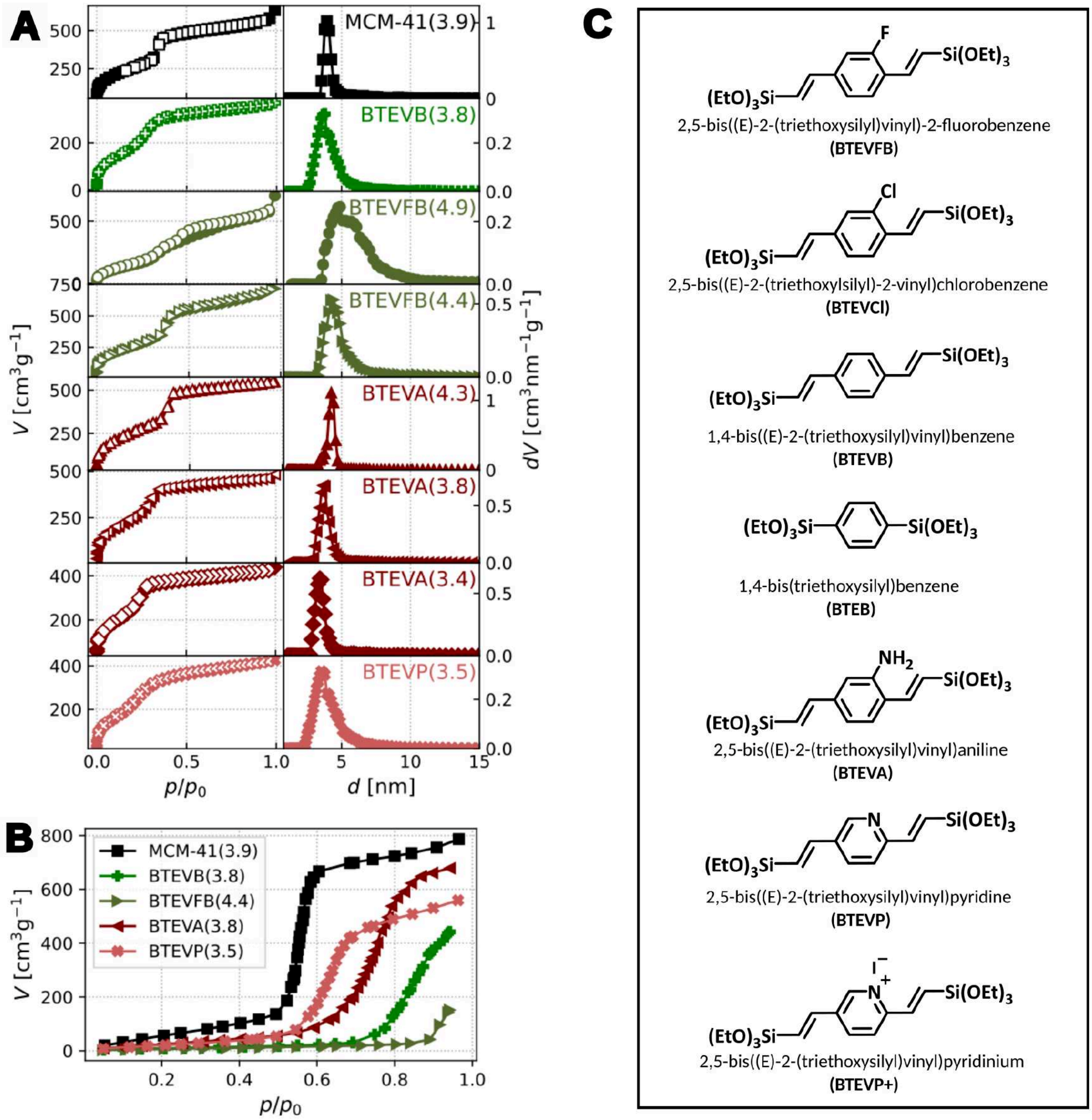

Figure 3.1: Nitrogen (**A**, left) and water vapor (**B**) sorption isotherms, pore size distributions (**A**, right) and chemical structures of the precursors (**C**) of porous materials used.

pores by use of a humidity chamber. This way, a complete filling of the pores could be achieved.

3.1.1 Hydrophilicity assessment

Information on hydrophilicity can be obtained from water vapor sorption isotherms using the onset before the capillary condensation step, as well as the slope of the isotherm in the region of $p/p_0 < 0.5$. Since the relative pressure region of the onset is determined not only by the chemistry of the material surface but also by the pore radius, materials with similar pore diameters should be compared for the determination of hydrophilicity (see Fig. 3.1B). For materials with the same pore diameter, more hydrophilic materials take more water at lower relative pressures, so capillary condensation occurs at lower relative pressures than for more hydrophobic materials[31].

In the relative pressure range $p/p_0 < 0.5$, the pure silica MCM-41(3.9) has the steepest slope. The onset of pore condensation of MCM-41(3.9) has the smallest value. BTEVFB(4.4) has by far the lowest slope and the highest onset position of the capillary condensation, indicating a comparatively higher hydrophobicity. In addition, it does not reach a plateau level after condensation, thus the pores are not completely filled even at higher relative pressures. BTEVA(3.8) and BTEVP(3.5) are found between the samples mentioned above. While both have a similar slope, BTEVP(3.5) has a lower onset position with $p/p_0 = 0.56$ than the BTEVA(3.8) with $p/p_0 = 0.67$. As with the divinylbenzene bridged BTEVB-PMOs, no plateau of the condensation step is achieved even at higher relative pressures. Since this material has the lowest slope and water density on the surface, it can be classified as the most hydrophobic among the presented materials. From the water vapor sorption analysis, the following series can be established, in which the hydrophilicity increases from left to right:

BTEVFB $<$ BTEVB $<$ BTEVA $\leq$ BTEVP $<$ MCM-41

3.2 Powder X-ray scattering on water-filled PMOs

The first experiment was conducted in May 2021 at the P02.1 beamline at DESY.[95] The beamtime was awarded for proposal I-20200440. Its goal was to obtain structural data on water and ice in PMOs using powder X-ray scattering. A visualization of the beamline endstation is shown in Fig. 3.2. The experiment was performed with a beam diameter of approximately 1 mm and at an energy of 60 keV. The powder samples were filled into glass capillaries with a diameter of 1.5 mm and a wall thickness of 10 µm (*Hilgenberg GmbH*). 30 scattering patterns were taken at each temperature for temperatures between 290 and 150 K with an exposure time of 1 s each. These were then added up to increase the overall signal intensity. At each temperature, the sample was given 15 min time to equilibrate. The cooling was controlled by a nitrogen cryostream surrounding the sample capillary. During cooling, the samples were rotated in order to increase the powder averaging and avoid the formation of bulk ice outside the capillary. The error of the temperature was estimated conservatively at 5 K, which is implied in all temperature data. The temperature of the crysostream was pre-calibrated before the measurement. Scattering patterns were recorded using a Perkin Elmer XRD1621 CN3 detector placed 750 mm downstream from the sample. LaB_6 was used as a calibration sample for the measurements. The results of this experiment are mainly discussed in chapters 4 and 5.

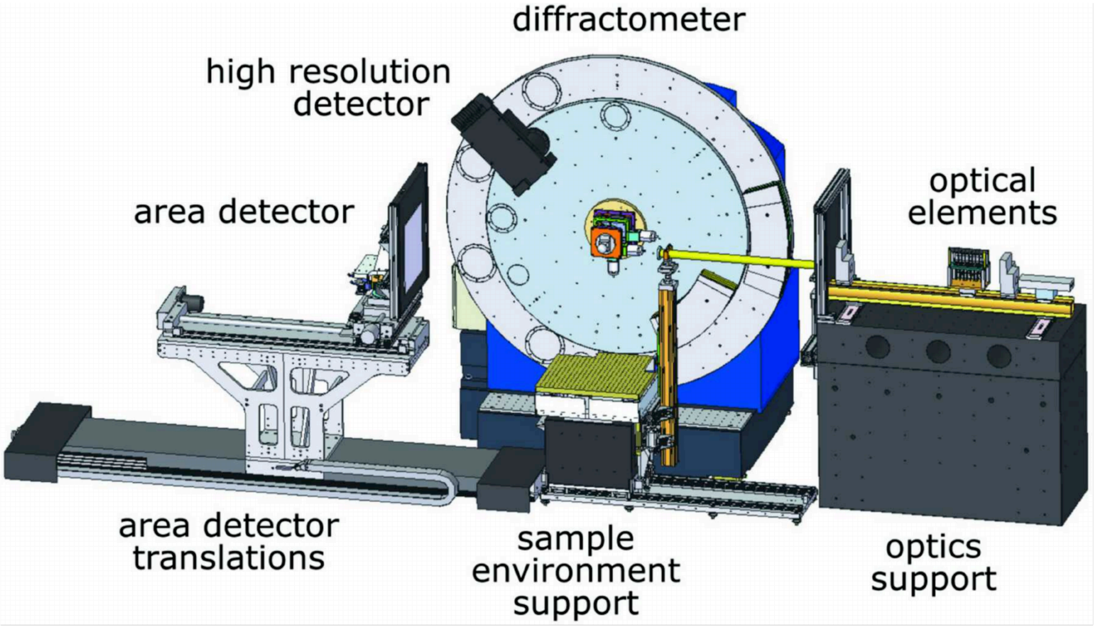

Figure 3.2: A visualization of the endstation of the P02.1 beamline. The X-ray beam is coming from the right-hand side in this image. The figure was created by Dippel *et al.* and was previously published in the *Journal of Synchrotron Radiation* under CC-BY 2.0 license.[95]

3.3 Nanofocused X-ray scattering on water-filled PMOs

The second experiment was performed at the nanofocus endstation of the P03 beamline at DESY.[96,97] The proposal for which the beamtime was awarded is I-20220503. The setup and general procedure of the experiment were similar to the one at P02.1. However, here, the beamsize was approximately 250 nm × 350 nm with a beam energy of 17.5 keV. The cooling of the sample was again achieved by the use of a nitrogen cryostream. Contrary to the experiment at P02.1, the cooling here was not done in steps but a temperature ramp was applied until 150 K were reached. 105 X-ray scattering patterns were recorded at 150 K in a pattern of five rows made up of 21 spots. This way, no spot was measured twice in a given sample. The images were acquired by an Eiger X 9M detector. The results of this experiments are presented in chapter 5.

3.4 In-situ X-ray scattering on PMOs during water adsorption

The goal of the third experiment was to observe the PMO material in-situ during water adsorption. In order to achieve this, the sample was filled into an open sample holder, which is placed in an airtight chamber.[52,98] A sketch of this chamber is visualized in Fig. 3.3B. A humidifier was connected to the chamber in order to control the humidity inside it. X-ray scattering signals were then taken while the humidity inside the chamber was raised in a stepwise manner. This experiment was conducted at the P21.1 beamline with a beam energy of 60 keV and a Pilatus3 X CdTe 2M detector for recording the scattering patterns. Beamtime was awarded from proposal I-20220497. An alternative technique for water adsorption is the incipient wetness (IW) technique, in which water is directly allocated to the sample with a syringe. The syringe is included in Fig. 3.3B but was not used in the experiment. The results of this study are presented in chapter 6.

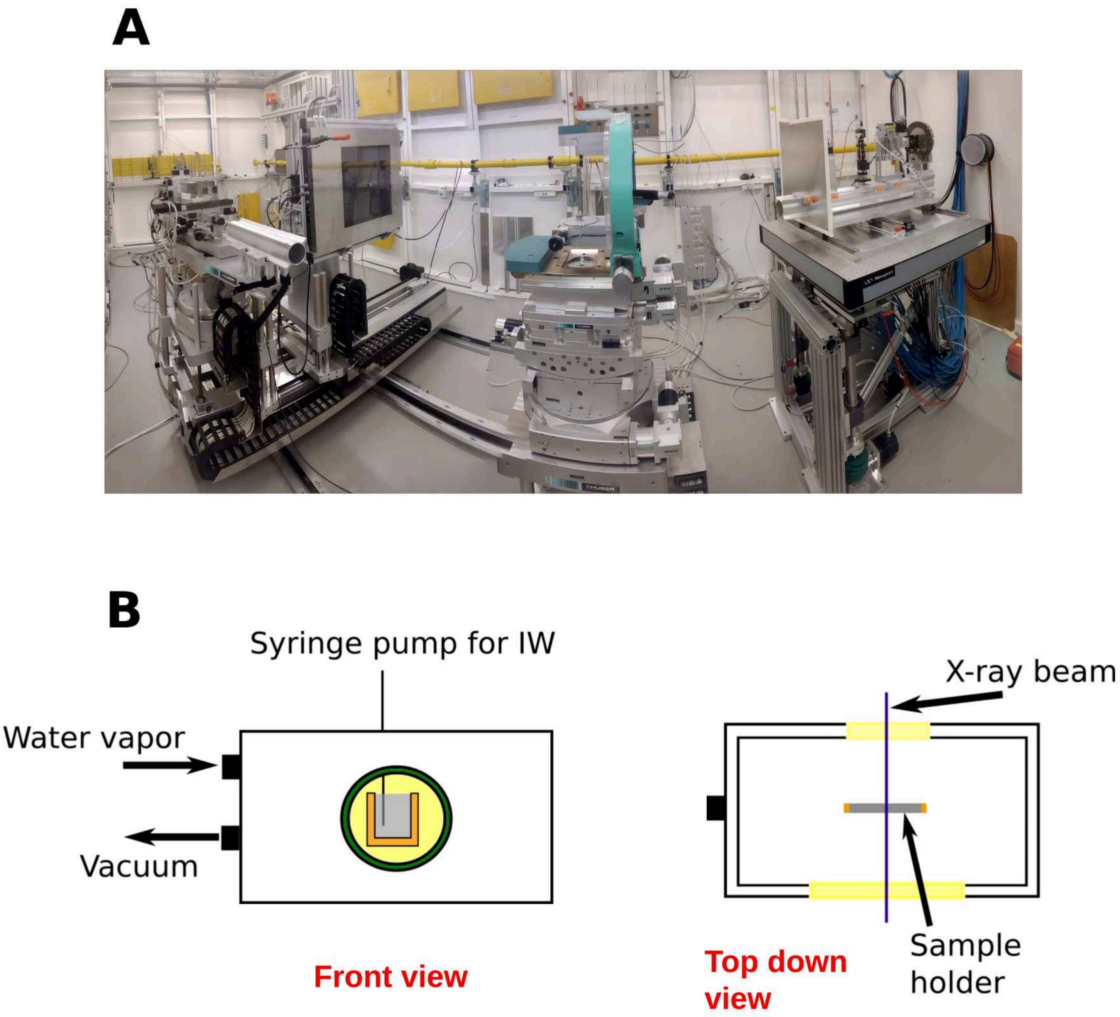

Figure 3.3: **A** A picture of the P21.1 endstation. The image was taken from the website of the beamline.[99] **B** A sketch of the chamber used for the in-situ study of PMOs being filled with water in front (left) and top-down view (right). The direction of the X-ray is downward in the right picture. The syringe pump for the incipient wetness (IW) technique was not used in the experiment.

4 Structure of Liquid Water in PMOs

This chapter discusses the structure of liquid water when confined in PMOs obtained by X-ray scattering. The measurements discussed in this chapter were conducted in the experiment explained in Section 3.2. This chapter is based on research that was previously published under CC-BY 4.0 license in The Journal of Physical Chemistry C.[91]

4.1 Extraction of the water signal

The first step in the analysis of the acquired data is the extraction of the water signal from the filled and empty PMO signals. The water was adsorbed into the PMOs by means of a humidity chamber where the humidity was gradually increased, thereby achieving a complete filling of the pores. As both the water-filled and empty PMOs were investigated, the water signal could be isolated by subtracting the signal of the empty PMO from the filled one. However, the peaks from the PMO material change upon the adsorption of water, leading to artifacts when simply subtracting the two signals from each other. Specifically, changes in the intensity, as well as the peak position are observed. The former can be explained by a change in contrast between the pore material and its content when water is adsorbed, while the latter could be due to strain on the material. A further discussion of this phenomenon in presented in Chapter 6. To mitigate this effect, the PMO peaks were removed and interpolated before the subtraction. The difference between the subtraction with and without removing the PMO peaks is shown in Fig. 4.1A. Here, the solid lines show the signals with the peaks removed, while the more transparent lines show the signals with the peaks present. Remaining artifacts are visible in the water signal, plotted in blue. Fig. 4.1B shows the signals with PMO peaks removed and with the limits of the y-axis chosen, such that features of the water signal are visible. A typical shape for an X-ray scattering signal of water is visible, with its two characteristic broad peaks.[42,100,101]

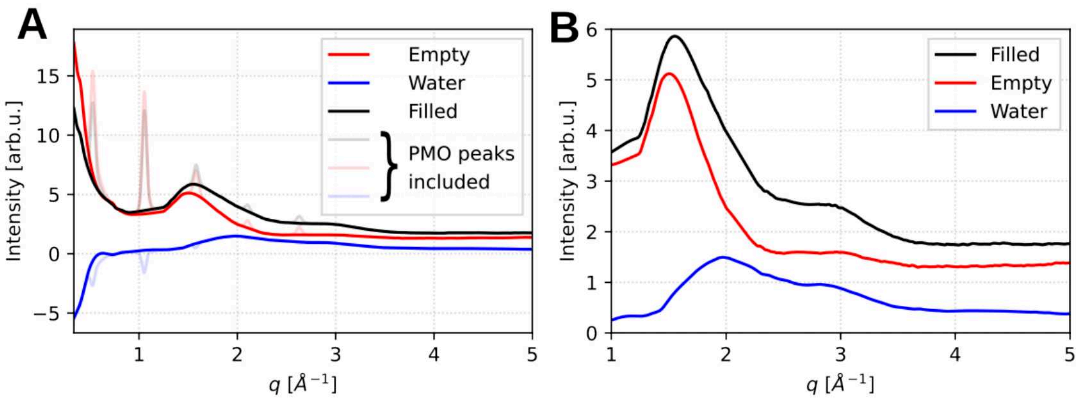

Figure 4.1: **A** The X-ray scattering signals of the empty (red) and filled (black) PMO materials, as well as the resulting water signal (blue). Each is shown with (solid line) and without (transparent line) peak removal. **B** The filled PMO, empty PMO and resulting water signals plotted on a smaller intensity range and the relevant q-range to highlight the features of the water signal.

Note that the result of this subtraction not only contains water-internal interactions but also those of water molecules with the pore wall, which contribute for example to the pair distribution functions and thus the $I(q)$.[38,75] This issue is further discussed later on in Sections 4.3 and 4.4. Because the electron density of the water molecule is mostly located at the oxygen atom, this is the dominant contributor to the X-ray scattering signal. As typical for X-ray studies, the computed quantities do therefore not contain information about the bonding between the oxygen and hydrogen atoms but only about the oxygen structure.[57]

The extracted water signals for the PMOs at temperatures between 290 and 240 K are shown in Fig. 4.2. One observes especially the growth of the second peak when going to lower temperatures. This effect appears in all measured samples, while the peak shapes and ratios vary throughout the materials.

One sample that stands out is BTEVB(3.8). Here, the intensities at different temperatures vary much more than in the other materials. For example, the signal at the lowest temperature, plotted in dark blue, shows higher intensities than at the next highest temperature, plotted in a lighter shade of blue, despite the plots at different temperatures being shifted. As this effect is not present in any of the other samples, this could either be artificially induced, *e.g.* by variations in the X-ray flux between the measurement of the filled and the empty PMO. As the focus of the more detailed discussion of the structure factor (Sec. 4.3) is focused on the positions rather than the intensities of the peaks, this should not influence the results discussed there.

Another notable sample is BTEVP(3.4), where the first peak in the $I(q)$ presents a different shape compared to other materials. It is much more asymmetric and its maximum is located at a lower q than in the other plots. The ratio of the two peaks is also shifted with the intensity of the first peak being much larger than that of the second peak.

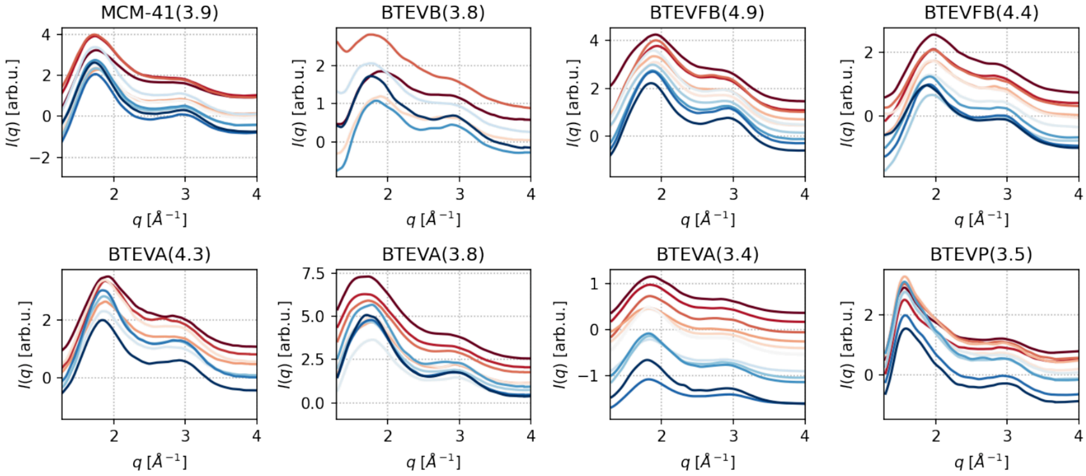

Figure 4.2: Intensities over q of water in different PMOs at temperatures between 290 and 240 K. The plots at different temperatures are shifted vertically for clarity.

In order to extract more information from the water signals, a number of analysis methods are applied, which will be further explained in the following section.

4.2 Analysis methods

To investigate the structure of the confined water in more detail, we make use of the (total) structure factor $S(q)$. This quantity is discussed in Sec. 2.1.1 and can be computed as described by Juhás *et al.*[102]:

$$S(q) = \frac{I_c(q) - \langle f(q)^2\rangle + \langle f(q)\rangle^2}{\langle f(q)\rangle^2}. \tag{4.1}$$

Here, I_c is the coherent scattering intensity and $f(q)$ the atomic scattering factor. In order to compute the coherent contribution of the scattering intensity, corrections have to be applied which are further described by Juhás et al,[102] as well as Egami and Billinge.[103] For the discussion of $S(q)$ we will focus on the region of q between 1.5 to about $4\,\text{Å}^{-1}$. In this region bulk water typically shows two peaks: The first of which shifts to smaller q upon cooling, while the second one shifts to large q. The subsequent spread of the two peaks can be used as a measure of the local order, such as the amount of tetrahedrally structured water in bulk.[100,101] From the structure factor the pair distribution functions (PDFs) can be computed follwing Eq. 2.6. $S(q)$ and the PDFs were computed using the *PDFGetX3* software.[102]

An interesting quantity that contains information on the tetrahedral structuring of water is the running coordination number n_{OO}.[11,21,42] It is calculated via the r-weighted integral of the reduced PDF,

$$n_{\mathrm{OO}}(r) = \int_0^r r' g(r')\,\mathrm{d}r', \tag{4.2}$$

with $g(r) = G(r) - 1$. n_{OO} gives the coordination number at a distance r from the origin atom.

4.3 Structure factor

The structure factors that were computed from the water signals in Fig. 4.2 are displayed in Fig. 4.3. The observations from Fig. 4.2 are also reflected in the structure factors, which is expected, as $I(q)$ and $S(q)$ are closely linked quantities (see Eq. 2.5 and Eq. 4.1). The plots especially show different peak ratios in the various materials, the unique peak shape in BTEVP(3.4), as well as the varying intensity in BTEVB(3.8). As mentioned in Sec. 4.1, the analysis focuses on the peak positions, rather than the intensities, therefore its variation should not influence the results and the conclusions drawn from them.

Figure 4.4A exemplary shows the structure factor of water confined in BTEVA(3.8)-PMO at temperatures between 290 and 240 K. During cooling both a spread and a growth of the two peaks is observed. This is a typical behaviour reported for water. In bulk water this peak spread is often attributed to a more pronounced formation of a tetrahedral hydrogen-bonded structure between the water molecules[100,101]. However, in confinement other interactions, like those between the water molecules and the pore

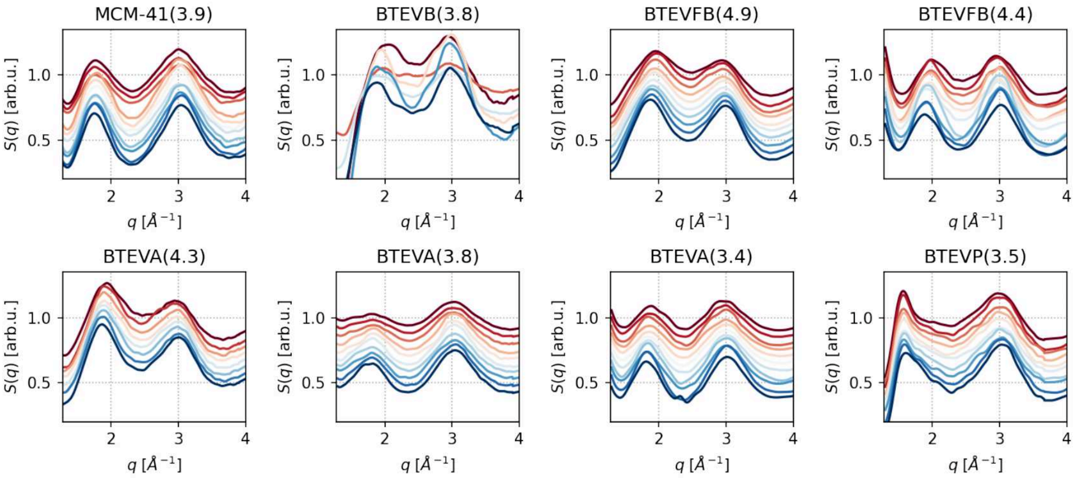

Figure 4.3: Structure factors $S(q)$ of water in different PMOs at temperatures between 290 and 240 K, computed from the intensity signals shown in Fig. 4.2.

wall, also have a considerable influence on the structuring of the molecules.[19–21,38,73]

Figure 4.4B shows the position of the structure factor peaks for different PMOs, as well as bulk water. The peak spread occurs in almost all samples with the exception of BTEVP(3.8). Here the lower-q peak (S1) seems to shift to larger q rather than lower ones.

The spread of the peaks during cooling, *i.e.* the difference between the two peak positions, can be observed in Fig. 4.4C. A strong dependence of the peak spread Δq on the confining material is found. Bulk water consistently shows the smallest values for Δq, while also giving rise to the strongest increase of the spread during the cooling process. The hydrophobic samples, which are shown with green markers in the figures, show a slightly larger spread and smaller increase for lowering temperature. The hydrophilic PMOs, as well as MCM-41(3.9), marked in red and black, respectively, show the largest Δq but cause a smaller change during cooling. BTEVP(3.5) shows the most extreme behaviour compared to bulk water by staying at almost a constant value for Δq throughout the cooling process.[100]

The further discussion of the structure factor, will be focused only on the position of the first peak (S1), as the second peak does not show a strong dependence on the different confinement, as well as bulk conditions. This reduces the statistical error compared to the difference between the peak positions.

These S1 positions q_1 are shown in Fig. 4.5A. A roughly linear behaviour is found in all

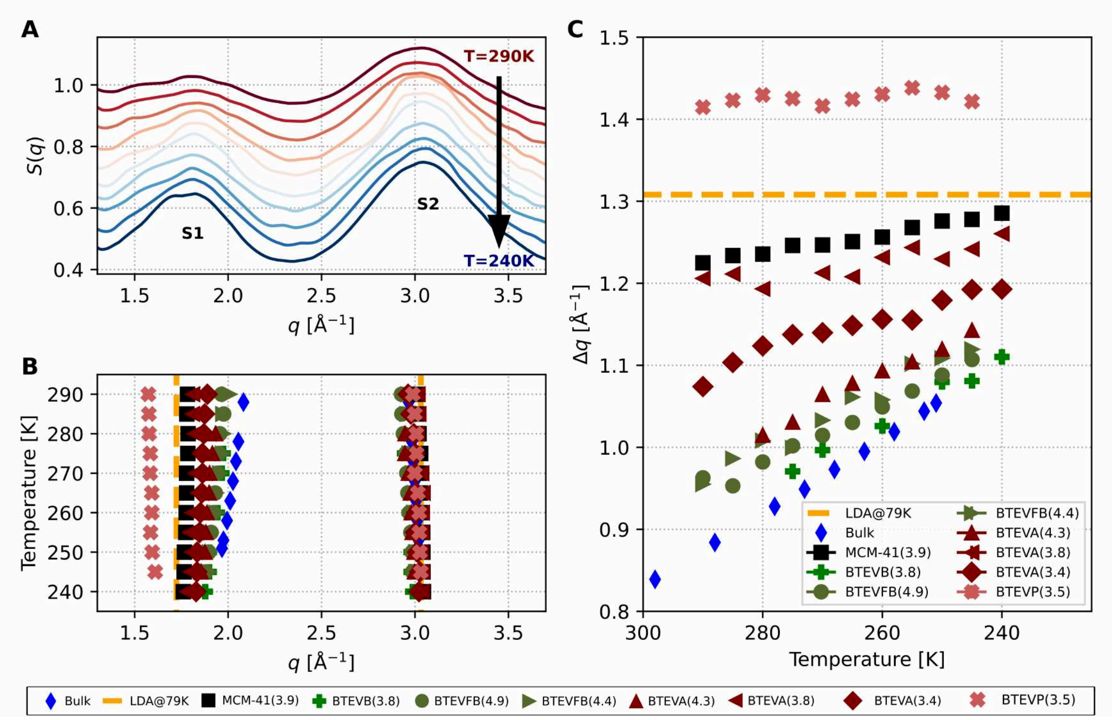

Figure 4.4: Structure factor peaks of various PMO materials at different temperatures. **A** The structure factor $S(q)$ of water in BTEVA(3.8)-PMO from 290 K (top) to 240 K (bottom) as an example of the typical form of the structure factor. **B** The structure factor peaks over different temperatures for water in different PMOs as well as in bulk. The bulk data was obtained from Sellberg *et al.*[100] **C** The splitting Δq between the $S(q)$ peaks. The LDA value was obtained from Mariedahl *et al.*[11]

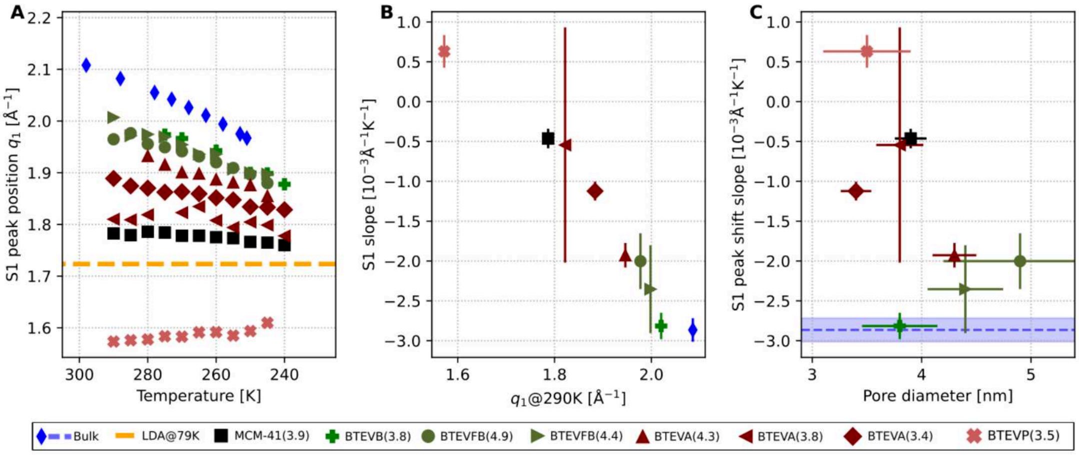

Figure 4.5: Visualizations of the shift in the position of the first structure factor peak of water in various PMOs. **A** Position of the first structure factor peak in relation to the temperature. **B** The slope of the linearly fitted peak shift against the peak position at 290 K of the same fit. **C** The slope of the linearly fitted peak shift against the pore size.

samples, with the slopes depending on the type of porous material. At room temperature, bulk water shows the highest q_1, which then decreases the most throughout the cooling process. Next to the bulk water are the rather hydrophobic materials BTEVB and BTEVFB, the latter of which were measured with two different pore diameters of 4.9 and 4.4 nm. At lower q_1, we then find more hydrophilic samples including BTEVA with different pore diameters, as well as MCM-41(3.9). These also show a smaller slope than bulk water and the more hydrophobic samples. BTEVP(3.5) shows a different behaviour than the other samples with the lowest q_1 at room temperature, which then increases with lower temperatures. A shift of S1 to smaller q in water under confinement has consistently been reported in previous studies as well.[21,104,105]

Figure 4.5A also shows the q_1-value for low density amorphous ice (LDA), as measured by Mariedahl *et al.*[11]. It provides a reference when comparing structural features in this context, as it has a strongly tetrahedral structure without interstitials[11,106]. In our study, all samples seem to approach the value of low density amorphous ice (LDA) when cooling, including BTEVP(3.5). In this sample, S1 starts in fact at a lower q_1 than LDA and then rises upon cooling, thereby also approaching the value of LDA. Note also that water under confinement has a smaller q_1 than bulk water for all observed materials and temperatures.

Fig. 4.5A suggests a correlation between the slope of the linearly fitted peak shift and the peak position at room temperature. This relationship is shown in Fig. 4.5B. Here, a clear trend with regard to material hydrophilicity is observed. At room temperature, q_1 is at lower values for hydrophilic samples, while the slopes of their S1 shifts are larger. Hydrophobic pores lead to larger q_1-values at room temperature while the slopes are more negative. The correlation between the hydrophilicity (*i.e.* the water sorption isotherm onset) and the q_1-slope is shown in Fig. 4.6, further supporting this trend. Here, the hydrophilic materials show slopes with lower absolute values compared to the hydrophobic samples. Note that Fig. 4.6 only contains few samples. These are the ones of which the water sorption isotherms are available to the author.

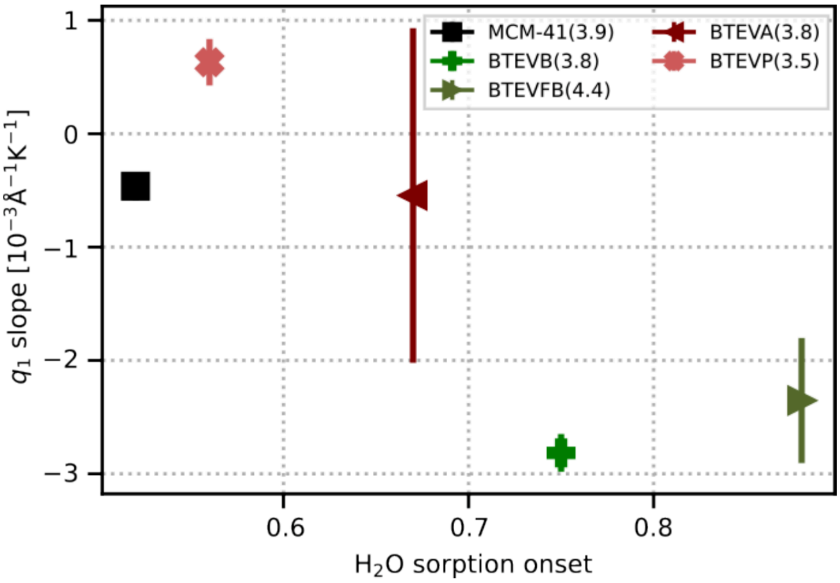

Figure 4.6: q_1 slope against H_2O sorption onset for sample where the water sorption isotherms are available.

Fig. 4.5C shows the slope of the linearly fitted peak shift against the pore diameter. For individual samples, a trend of the slope deviating further from bulk water in smaller pores can be observed. This trend seems to be stronger between the hydrophilic pores than the more hydrophobic ones. BTEVA(4.3) shows a slope closer to bulk water and the hydrophobic samples than to BTEVA(3.8) and BTEVA(3.4). In the hydrophobic samples, no such trend can be observed. In fact, they seem to show a decrease of the slope for smaller pore diameters, notably even between BTEVFB(4.9) and BTEVFB(4.4), which only differ in pore size. However, due to the pore size distributions (cf. Fig. 3.1A), errors in fitting parameters and the small number of measured samples, one should be careful when interpreting this data.

In bulk water, a lower-q position of S1 is often attributed to a larger amount of tetrahedrally structured water.[58,100] While this may also contribute to this effect, it cannot fully be transferred to confined water, as interface and geometric effects become non-negligible in this case. A particularly interesting quantity that varies in confinement conditions is the density of water. It has been agreed upon that layers with different densities form in water when confined in hydrophilic nanoporous material.[19–21,73,107,108] More molecules adsorb to the pore wall in this case, leading to a higher number density close to the interface and a lower density in the core of the pore. As discussed above, the average density of water throughout the whole pore cross section under confinement in MCM-41 is also considerably lower than that of bulk water.[21,107]

This effect could explain the material-dependent shift of the S1, as it is most prominent in rather hydrophilic pores, with a strong wall-water interaction. As water confined in hydrophobic pores has a larger contact angle with the pore wall, the density is not decreased as strongly and therefore the S1 shift is not observed as strongly as in hydrophilic pores. Furthermore, due to geometric reasons, the negative pressure could scale with smaller pore diameters. This might lead to the effect being more pronounced in smaller pores than in larger ones, which is also reflected in the stronger S1 shift presented in Fig. 4.5. The interplay of pore size and hydrophilicity seems to induce a very low density in BTEVP(3.5), which would be even lower than that of LDA and especially low at room temperature. Note that while the density cannot completely be identified via the structure factor, a smaller density would certainly lead to smaller values of q_1[21] and is therefore in agreement with the data presented here, as well as previous studies.[21,104,105]

The next sections will now move the discussion from reciprocal space to real space by investigating the PDFs which were calculated from the structure factors, as well as the running coordination numbers.

4.4 Pair Distribution Function

Figure 4.7A shows the structure factors at the highest and lowest studied temperatures ($T_{\max}$ and $T_{\min}$). In Figure 4.7B the computed pair distribution functions (PDFs) for water in the various PMO materials are plotted once at $T_{\max}$ and once at $T_{\min}$. The values for $T_{\max}$ and $T_{\min}$ are noted in the individual plots for each sample in Figure 4.8.

The highest temperature was 290 K in all cases except BTEVA(4.4), where it was 280 K and BTEVB(3.8), where it was 275 K, while and the lowest was 240 K for MCM-41(3.9) and BTEVA(3.8) and 245 K for BTEVA(4.4), as well as BTEVP(3.8). For bulk water, $T_{\text{max}} = 295.1\,\text{K}$ and $T_{\text{min}} = 254.1\,\text{K}$.[100]

Figure 4.7B reveals qualitative differences in the structure of confined water compared to bulk that are present in all PMO materials. The most striking one is the splitting of the broad second neighbour peak of bulk water into several seperate ones. In MCM-41(3.9), BTEVA(3.8), BTEVA(3.4) and BTEVP(3.5), two peaks are present in this region, while the rest of the samples cause three peaks.

The appearance of several peaks emerging in the region from 3.5 to 5 Å can be attributed to a more pronounced, albeit distorted, tetrahedrally bonded network, which has also been observed in previous studies for (hydrophilically) confined water.[21,38,39,107] It also has been argued that the interaction between the silanol groups in the pore wall and the confined water also contributes to the pair distribution function at a bond length of approximately 3.8 Å.[38,75] However, this effect does not seem to be reflected in all measured data.

Comparing the rather hydrophilic samples BTEVA(4.3), BTEVA(3.8) and BTEVA(3.4) shows a shoulder at 3.8 Å in BTEVA(4.3), which cannot be observed for the latter two. If the water-substrate interaction was a dominant effect in these pores, one would expect a more prominent contribution in smaller pores, instead of larger ones. On the other hand, this peak is quite prominent in the more hydrophobic BTEVB(3.8). An explanation for this difference could be, that in the hydrophobic samples, more water molecules bind to the silanol groups, as they interact less with the functional groups. In contrast, in hydrophilic samples, the increased amount of interactions between the functional groups and the confined water leads to less interactions with the silica in the pore wall. While the water-silanol interaction contributes to the PDFs as well, we also propose another explanation that addresses the emergence of three peaks in materials with larger pores compared to only two in those with smaller ones.

While the broad peak in bulk water suggests a broad distribution of second-neighbour distances, the two peaks present in the previously mentioned samples would hint at two more discrete distances. The emergence of a third peak may indicate a more bulk-like behaviour in these materials, such that the number of possible second-neighbour bonding lengths is increased in comparison to the samples giving only two peaks. With this interpretation, the results presented in Fig. 4.7B are consistent with literature,[21,38,39,107]

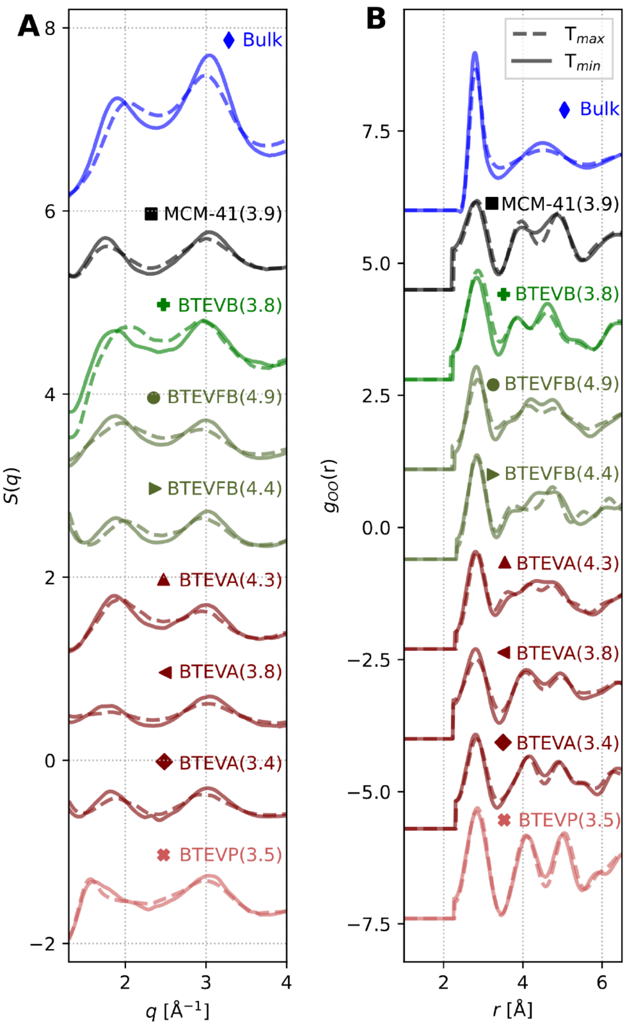

Figure 4.7: **A** Structure factor of water in the studied samples at the highest as well as the lowest used temperature. The data for bulk water was measured by Pathak *et al.*[42]. The curves are set 1 unit apart of each other. **B** The pair distribution functions at the same temperatures. $g_{OO}(r < 2.2\,\text{Å})$ were set to zero, as signal in this range comes from artifacts of the correlation. Bulk data is from Skinner et al[43]. The curves are set 1.7 units apart of each other.

as two peaks are predominantly present in smaller and more hydrophilic pores and three peaks in larger, as well as more hydrophobic pores.

It is also possible that this splitting is due to artifacts from the calculation of the PDFs. The PDF is defined as an infinite integral (see Eq. 2.6). By using finite integration boundaries, as necessary for experimental data, an oscillation is introduced into the data, the so-called termination ripples.[103,109] Maxima in this oscillation could be misinterpreted as PDF peaks. This effect therefore proposes itself as another source of the third peak.

4.5 Running Coordination Number

The analysis of the pair distribution functions gave a first hint towards the presence of tetrahedral structuring in the confined water. To gain more insight into this, we take a look into the interstitial molecules between the first and second neighbour peaks. These can be visualized by integrating the radial distribution function to obtain the running coordination number n_{OO}, following Eq. 4.2[11,21,42]. The resulting curves for n_{OO} versus the distance from an initial oxygen atom are shown in Fig. 4.8, again at the highest and lowest temperatures for each sample. The curve for bulk water is also shown for comparison. More or less pronounced plateaus are observed around 3.5 Å in all samples, as well as in bulk water. A more strongly pronounced plateau can be attributed to more tetrahedral structuring, as it indicates less or no interstitial oxygen atoms between the first and second neighbour shells.[42] From this we can derive another qualitative statement about the presence of tetrahedrally structured water in the various confining materials. The curves of BTEVA(3.8), BTEVA(3.4) and especially BTEVP(3.5) and MCM-41(3.9) show a strongly pronounced plateau, indicating a larger ratio of tetrahedral water when compared to bulk water. Water confined in the remaining materials shows a more bulk-like plateau, indicating a more disordered water structure in these materials. These results are again in agreement with the previously discussed findings that (hydrophilic) confinement supports the formation of a tetrahedrally structured hydrogen bond network.[21,38,39,107]

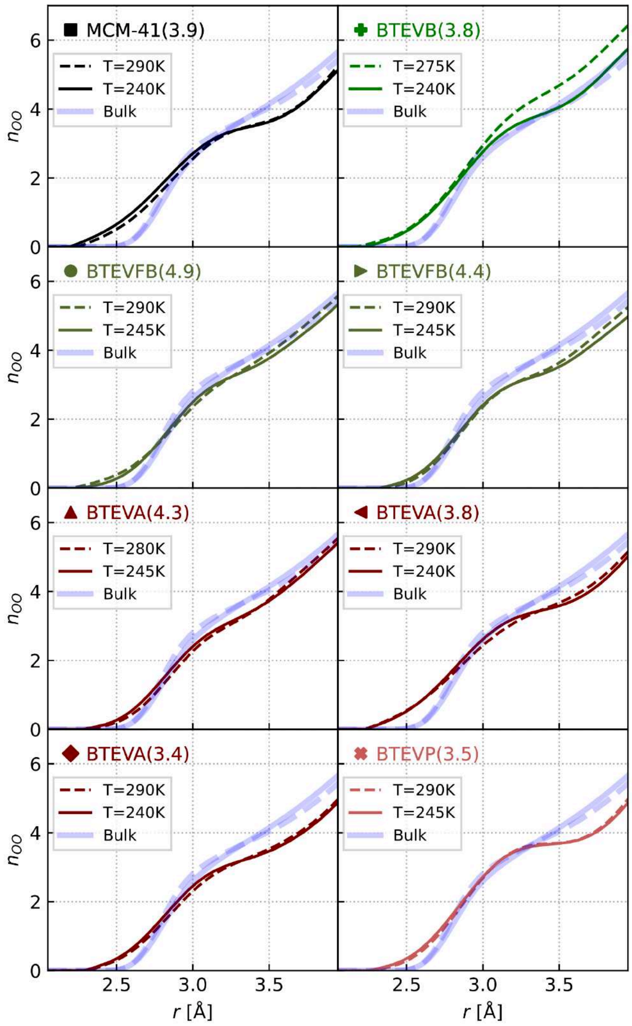

Figure 4.8: The running coordination number of water in the samples. Bulk data was calculated from the PDF obtained from Skinner *et al.*[43]

4.6 Summary

The presented results confirm that the structural behavior of water under confinement in PMOs is strongly influenced by the properties of the confining material. In particular, the shift of the first structure factor peak of water during cooling differs more strongly from bulk water in hydrophilic pores than in more hydrophobic pores. This effect can be attributed to a lower density of the confined water compared to bulk. It could also be shown that by reducing the pore diameter, this effect can be further amplified. This observation experimentally confirms previous simulation studies that propose a lowered density, specifically in hydrophilic confinement, due to negative pressures inside the pore.[19–21]

In the PDFs of water confined in PMOs, a distinction can be observed between materials which lead to either two and three peaks in the region of 3.5 to 5.5 Å, *i.e.* the region of the second neighbour peak in the PDF of bulk water. While smaller pores give two distinct peaks, confinement in larger pores leads to three peaks or no clear peak structure at all. The presence of two peaks is attributed to the development of a distorted tetrahedral bonding structure,[21,38,107] while the presence of a third peak could hint at the restoration of more bulk-like conditions. Looking at the minimum between the first and second PDF peak, as well as the running coordination number, a higher amount of tetrahedral structuring in smaller and more hydrophilic pores was observed. In contrast, larger and more hydrophobic pores show a weaker development of tetrahedral structures. This is in agreement with conclusions from previous scattering studies, which also observe that hydrophilic confinement supports tetrahedral structuring.[21,38,39]

It is however important to mention previous investigations of water, specifically under confinement in PMOs concluded that this confinement actually hinders the development of a tetrahderal network.[31,36] This discrepancy might be related to the fact that these studies use spectroscopy techniques. It was mentioned before (Sec. 2.2.3) that spectroscopy and scattering-based techniques come to conflicting conclusions regarding the tetrahedrality of confined water. While studies using spectroscopy tend to conclude less tetrahedrally structured water,[31,36,37] scattering techniques tend to indicate a stronger tetrahedral structuring.[38,39] Considering this, the results of this investigation fall in line with literature, despite conflicting previous studies of water in PMOs. It is also the first X-ray scattering study of this kind specifically focused on water in PMOs.

Note that the study presented here only contains data at limited temperatures. It would be of great interest to investigate, how the observed behavior, especially the shift of the first structure factor peak, continue under further supercooling. Furthermore, a relatively limited range of pore diameters (3.4 to 4.9 nm) was considered. Confinement in smaller pores may further inhibit the formation of ice and therefore enable studies at lower temperatures than in this study.

Despite these limitations, it can be concluded that by confinement in PMOs with varying pore diameters and pore wall chemistry, it is possible to tune fundamental properties of water, such as density and amount of tetrahedral structuring.

5 Structure of Ice in PMOs

This chapter investigates the effect of PMO confinement on the structure and orientation of ice. To achieve this, powder X-ray scattering, as detailed in Sec. 3.2 was used to determine the structure and lattice parameters. The orientation of ice crystallites was investigated by nanofocused X-ray scattering in combination with X-ray cross correlation analysis (XCCA, see Sec. 5.3.1). This chapter is largely based on research that was previously published in *The Journal of Chemical Physics*.[92]

5.1 The intensity signal

Before quantifying the structure of ice, *e.g.* by identifying the lattice parameters of confined ice crystallites, a more qualitative analysis of the integrated intensities should be conducted. Figure 5.1 shows the azimuthally integrated X-ray scattering intensity of water confined in various PMOs at temperatures between 290 and 150 K. It was obtained by subtracting the signal of an empty PMO from that of its water-filled counterpart. In some samples, namely BTEVFB(4.9), BTEVA(4.4), BTEVA(3.8) and BTEVP(3.5), this did not fully remove the signal from the empty PMO. Here, remaining peaks at 1.7 Å^{-1}, which stem from the periodicity of the functional groups in the pore wall, are visible. The reason for this were on the one hand fluctuations of the X-ray intensity during the measurement, which could not fully be compensated by normalization. On the other hand, the electron density difference is lower for water-filled pores, hence the PMO peaks are more prominent inempty (or air-filled) pores. In these cases, the (100) peak of hexagonal ice overlaps with the PMO peak and was therefore not taken into account when determining the lattice constants discussed later.

5.1.1 Freezing temperature and non-freezing layer

Fig. 5.2A shows the extracted water signals at the temperatures, where freezing occurs, specifically between 245 and 220 K. From these, the temperature range in which freez-

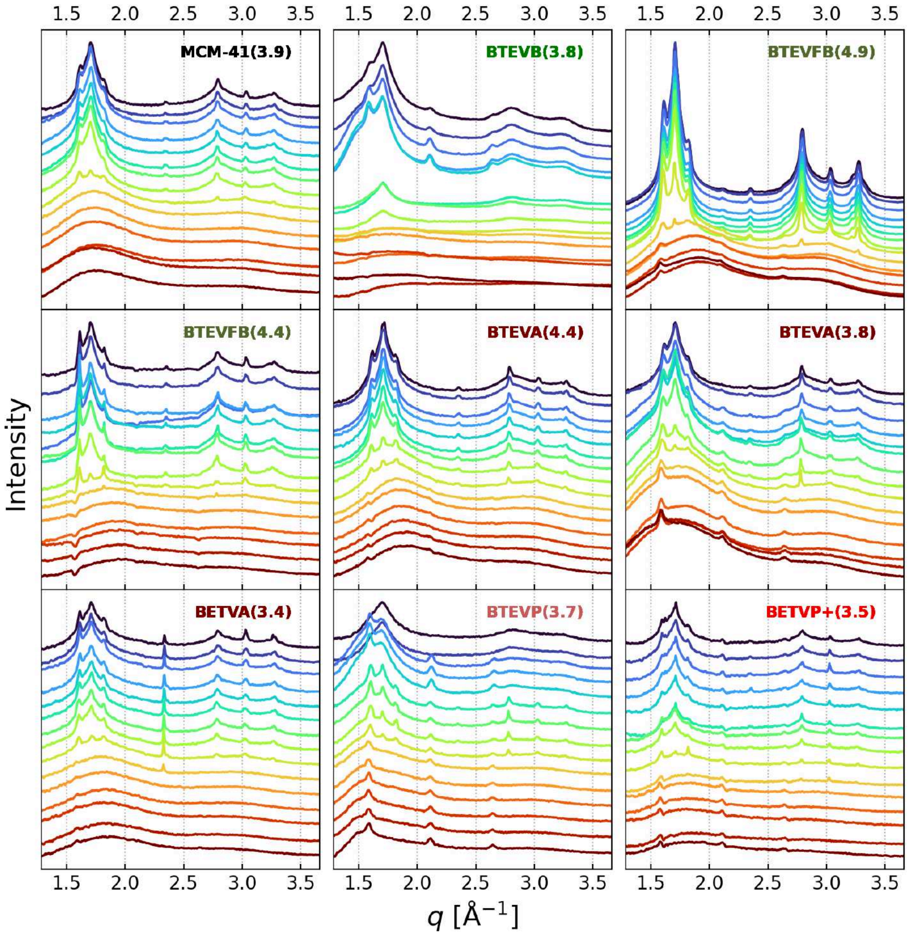

Figure 5.1: X-ray diffraction signal of water in several different PMOs at temperatures between 290 (bottom, red) and 150 K (top, blue) in steps of 10 K.

ing occurs can be determined more precisely for each material. The range covers the temperatures between the last $I(q)$, where no ice peaks are observed and the first where ice peaks are clearly visible. These freezing ranges are plotted in Fig. 5.2B together with the expected melting point for confined water, assuming a non-freezing layer thickness between 0.4 and 0.7 nm.[18,23] One observes that the determined freezing ranges are similar to the expected melting points, which confirms that this signal originates from confined water/ice, rather than *e.g.* intergranular ice. The plot also shows lower freezing temperatures for smaller pores, as expected (see section 2.2.3). However, for pore diameters smaller than approximately 4.0 nm, no further decrease is present. They are also in a similar range as the freezing temperatures by Mietner, presented in Fig. 2.18. Note that the two materials with the largest pore diameter, *i.e.* BTEVFB(4.9) and BTEVFB(4.4) are also the only two more hydrophobic pores plotted here. No freezing range for BTEVB(3.8) could be determined as the freezing point fell into the range that is lost due to the re-measurements mentioned above in Sec. 5.1.

Using Eq. 2.11, it is now possible to estimate the thickness of the non-freezing layer based on the temperature ranges presented in Fig. 5.2B. These are shown in Fig. 5.3, where a decrease in the thickness with decreasing pore diameter is observed. However, the values for the smallest pores are unphysical as the nearest-neighbor distance of two water molecules, plotted in orange, is typically about 0.18 nm and therefore higher than the lowest value for BTEVP+(3.4) and BTEVA(3.4). If these unphysical values are disregarded, the non-freezing layer thickness is more or less constant between about 0.4 and 0.8 nm, in agreement with the literature.[23] Note that this is just a very rough estimate, as the melting and freezing temperatures are not thermodynamically equivalent and because the determination of the freezing temperature ranges is quite imprecise. Furthermore, K_{GT} is assumed to be the same for all materials, even though it can vary depending on the material. However, the assumption should be reasonable, ass all materials are silica-based and therefore rather similar.

5.1.2 Hexagonal, stacking disordered and amorphous phases

In most samples, characteristics of both I_h-like, sharp Bragg peaks and more ice I_c-like, diffuse peaks are visible. Specifically, in the regions between 1.5 and 2.0 Å^{-1} and between 2.5 and 3.5 Å^{-1}, an overlay between a broad diffuse peak and the triplet characteristic for ice I_h is observed. This structural behaviour of ice crystallization has

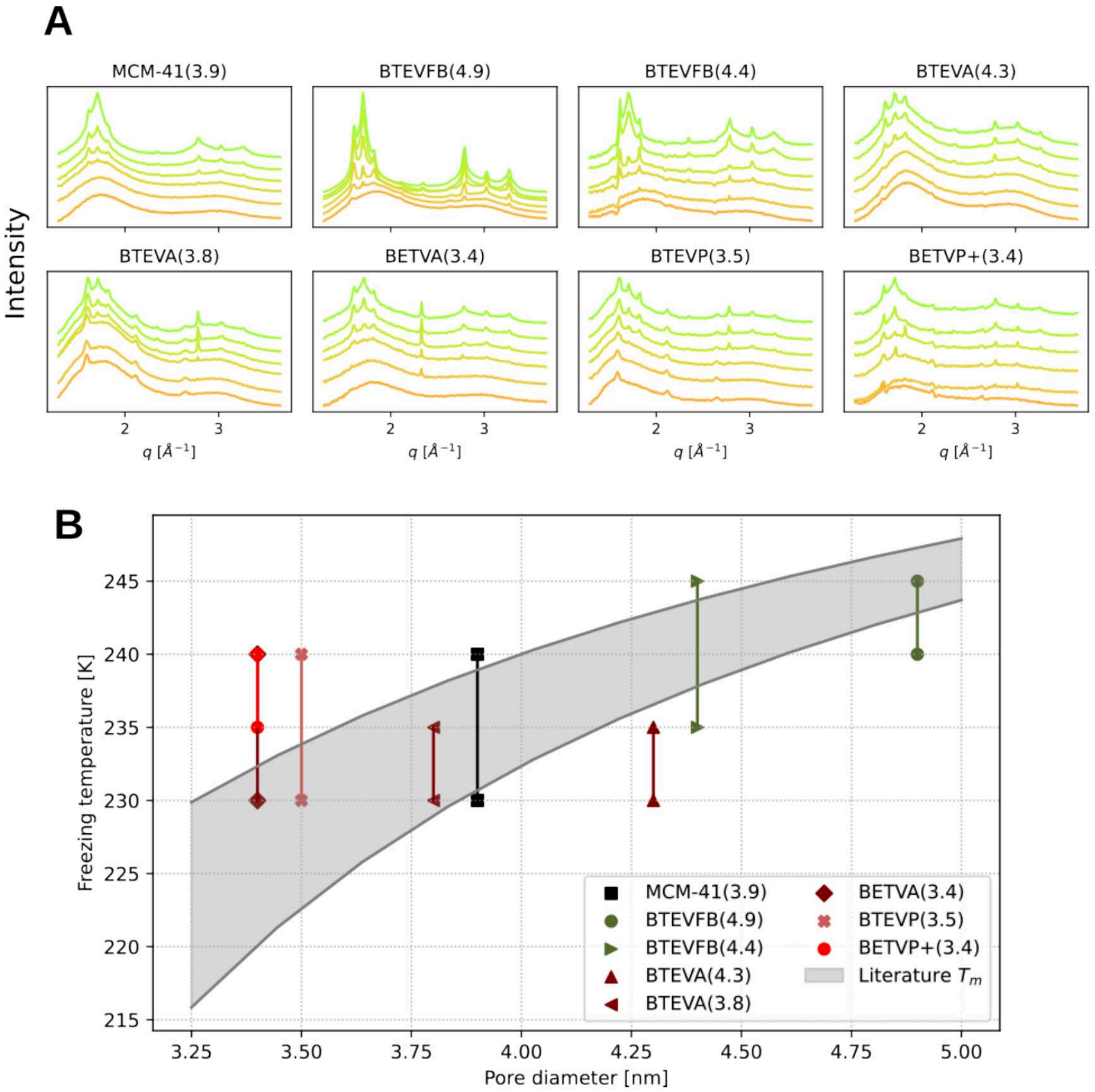

Figure 5.2: Freezing ranges of water in PMOs. **A** $I(q)$ of water in various PMOs in the range where freezing generally occures (245 (bottom) to 220 K (top)) in steps of 5 K. The colors reflect those of the same temperature region in Fig. 5.1. **B** Freezing ranges of water in various PMOs in relation to pore diameter. A freezing range is defined as the range between the last temperature without ice peaks in the $I(q)$ and the first where they are clearly visible. T_m was calculated assuming a non-freezing layer of 0.4 to 0.8 nm.[18,23]

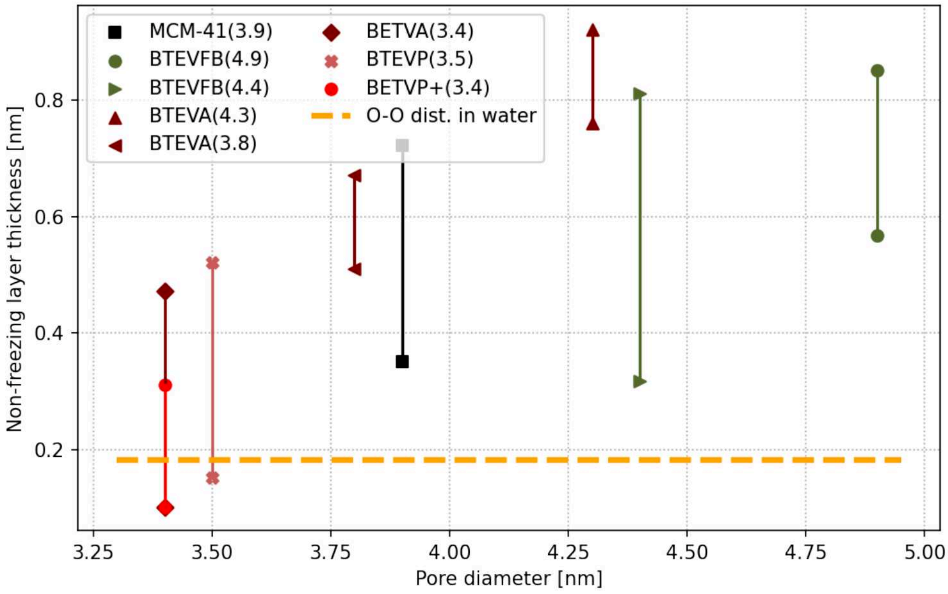

Figure 5.3: The thickness of the non-freezing water layer as calculated from the freezing temperature ranges using a modified Gibbs-Thompson equation (eq. 2.11).[23]

been found in previous simulation[22,89] and experimental[23,110,111] studies on water in nanopores. Fig. 5.4 shows a separation of the diffuse and Bragg contributions for the

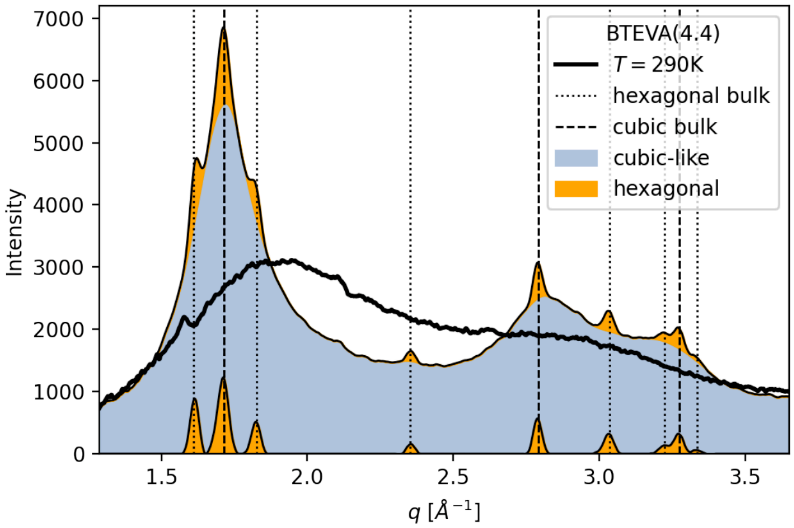

Figure 5.4: The cubic-like and hexagonal contributions to the integrated scattering pattern at T =165 K are shown in blue and orange, respectively. The $I(q)$ of the confined water at 290 K is plotted for comparison (black), as well as the peak locations for bulk cubic and hexagonal ice (dark grey). Bulk hexagonal peaks are also located at the same positions as the bulk cubic peaks.

example of BTEVA(4.4). The contributions are marked in blue (diffuse) and orange (Bragg). The diffuse part also contains the contribution from liquid, non-freezing interfacial water, which is known to appear in nanopores[22,72,89]. This contribution is not marked in Fig. 5.4 as it is difficult to meaningfully separate it from the broad cubic-like contribution. The confined water in the same pore at room temperature is also plotted to visualize the general shape of this amorphous contribution. However, as discussed in Sections 4.1 and 4.3, the first sharp diffraction peak of water grows and shifts to lower q-values under confinement and even more during cooling, ending up closer to the first diffuse peak.

The presence of both the diffuse and Bragg contributions suggest the formation of stacking disordered ice I in the pore. The diffuse part implies small individual crystallites with a large number of stacking faults while the Bragg contribution can probably be described as ice I_h with a large ratio of Φ_h to Φ_c according to Malkin *et al.*[65]. Going forward, the Bragg contribution will therefore be referred to as the hexagonal contribution even though it does probably not represent pure ice I_h.

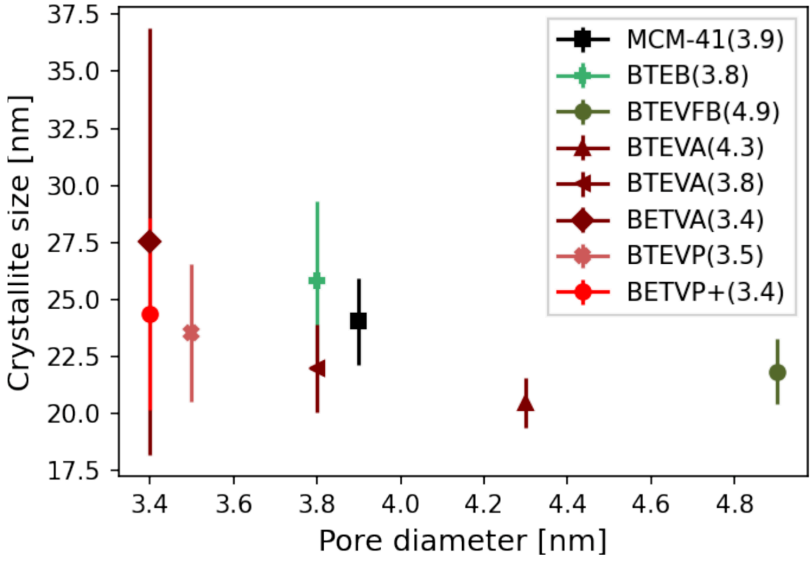

Figure 5.5: The crystallite sizes of the hexagonal contribution in the measured samples in relation to the pore diameter calculated using the Scherrer equation.

In order to estimate the sizes of individual crystallites, the Scherrer equation (Eq. 2.9) can be applied, leading to values of 35 to 50 nm with no systematic difference between the samples. The values are rather vague, as the Scherrer constant K strongly depends on various factors as mentioned in section 2.1.2. In this case, cylindrical crystallites are assumed, which generally leads to Scherrer constants $K > 0.9$. The number therefore only serves as an estimate of the order of magnitude of the crystallite size, not as an exact result. The crystallites of the diffuse constribution was calculated to be in the range of 1 to 2 nm. This is in agreement with findings of Moore *et al.*[22], stating that cubic ice domains in silica pores are in the range of only few layers. However, due to the discussed amorphous contribution, a precise determination is not possible.

Some of the studied samples stand out in this regard. BTEVFB(4.9) shows the previously discussed general structure but has much higher relative intensities of the (hexagonal) ice peaks. This can be explained by its pore diameter, which is the largest of the measured samples at 4.9 nm. Therefore, the amount of ice present in the pore is larger than for the other materials, leading to a stronger scattering signal. In BTEVB(3.8) and BTEVP(3.5), one can see that the patterns differ at the five lowest temperatures. These measurements were performed with a higher initial cooling rate than the standard procedure with no equilibration steps being taken while cooling down to 180 K. In BTEVB(3.8), the PMO peak at $1.7\,\text{Å}^{-1}$ is more visible at these temperatures while the overall structure is qualitatively the same as for the higher temperatures. In BTEVP(3.5), however, we observe no hexagonal ice peaks at the separately measured temperatures. This suggests that the emerging ice structure is dependent on the cooling rate. Specifically, a higher cooling rate seems to hinder the formation of hexagonal ice. Note also that BTEVB(3.8) represents the only sample in which no hexagonal ice peaks were observed in both the standard measurement and the measurement with ramped cooling.

5.2 Lattice constants of ice in PMOs

This section will investigate the hexagonal contribution to the signal with a focus on the influence of the PMO confinement on the ice structure. Figure 5.6 shows the lattice constants for the hexagonal ice contributions inside the different PMOs, as well as those of bulk ice. The bulk ice values are based on the polynomial expression given by Röttger *et al.*[112,113] to describe the lattice constants of hexagonal ice over a wide temperature range sorted by pore size. While the measured samples follow the general trend as expected in bulk ice, some notable deviations are observed.

The left panel of Fig. 5.6 shows ice in the largest pores with diameters $\geq 4.4\,\text{nm}$. While the more hydrophilically amine-functionalized BTEVA(4.4) closely follows the lattice parameters of bulk ice, the two samples with the BTEVFB precursor do not follow this behavior. In BTEVFB(4.4), both a and c are larger than in bulk ice. Their ratio, however, is still similar to bulk ice. This is not the case for BTEVFB(4.9), where only c differs from bulk, implying an elongated hexagonal unit cell.

This trend is also observable for MCM-41(3.9) in the middle panel. Similarly to BTEVFB(4.9), hexagonal ice in MCM-41 seems to be elongated along its c-direction. In contrast, BTEVB(3.8) gives a lower value for a and consequently also a lower value for the c/a ratio.

The smaller BTEVA(3.4) and BTEVP+(3.5) in the right panel show a stronger deviation from bulk than the ones discussed previously. Note that BTEVA(3.4) differs in particular also from its larger counterparts. While ice in BTEVA(3.4) and BTEVA(3.8)

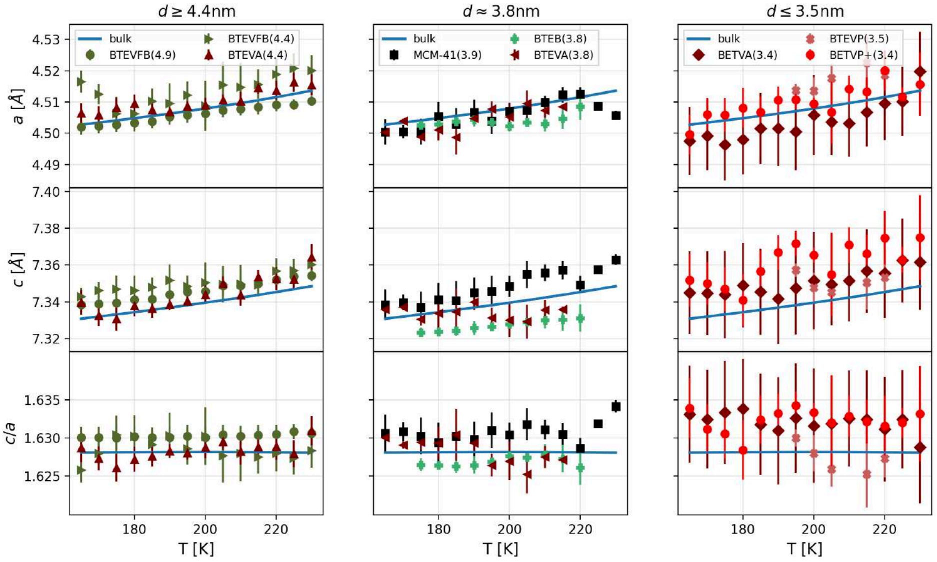

Figure 5.6: Lattice parameters a and c of hexagonal ice in various porous materials, as well as their ratio c/a. The three columns show materials with decreasing pore diameters from left to right. Hydrophilic PMO samples are plotted in a shade of red while more hydrophobic ones are a shade of green. MCM-41 is plotted in black. The lattice parameters of bulk ice are also plotted for comparison. Bulk values were calculated according to Röttger *et al.*[112,113]

structures similarly to bulk ice, in BETVA(3.4) it also shows an elongated hexagonal cell with c/a that is above that of bulk ice. This may indicate that a pore size effect only becomes relevant below 3.8 nm, at least in BTEVA-PMOs. However, it is to note that BTEVA(3.4) has a larger error margin, potentially stemming from the lower amount of water adsorbed in the pore, which in turn gives a weaker scattering signal. The other sample with a pore diameter in this range, BTEVP+(3.5), supports a pore size-dependent deformation of the hexagonal structure as it shows the most elongated c-parameter out of all materials. Note here that due to its synthesis, a residual iodide ion is present in the BTEVP+(3.4), which takes up additional space in the vicinity of a functional group. The c/a-ratio in BTEVP(3.5) is again more closely following that of bulk ice, however, slightly larger lattice parameters for both a and c are observed, suggesting an overall expanded unit cell, similar to BTEVFB(4.4).

It is not obvious what causes these change in the lattice constants relative to bulk ice. An explanation could be that the highly stacking disordered cubic-like phase leads to connections with the hexagonal ice domains that would be unfavorable under bulk conditions, leading to the observed elongated (BTEVFB(4.9), MCM-41(3.9), BTEVA(3.4), BTEVP+(3.4)), expanded (BTEVFB(4.4), BTEVP(3.5)) or truncated (BTEB(3.8)) hexagonal unit cells. Notably, only BTEB(3.8) leads to a c/a smaller than bulk while also being the sample with the smallest d_{org} at only 0.76 nm (see Table 3.1). This length describes the distance between the silicon atoms at either end of the organic moiety. With this, d_{org}/c in BTEB(3.8) is close to 1, while for all other PMOs, the ratio is closer to 1.5. While there is also the interfacial water between the pore wall and the ice, this indicates that the length of the organic moieties could play an important role in the development of ice in PMOs and seems to be a major factor in the observed lattice constant shift.

5.3 Ice crystal orientation

The shifts in lattice parameters are most often not equal for a and c. This could be caused by a dependence of the lattice parameter shift on the orientation. Such a dependence could stem from the pore wall chemistry. The interactions of water with the organic moieties could force the molecules into arrangements that would not be favorable under bulk conditions while hindering others that would. We shall now investigate the orientation of these hexagonal crystals relative to the pore axis to evaluate such a de-

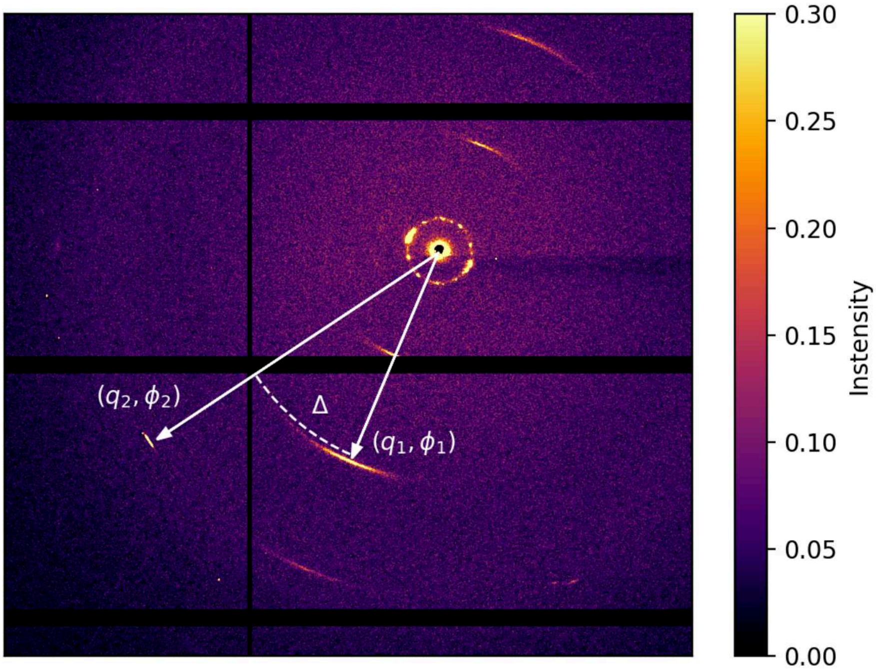

Figure 5.7: A detector image of ice-filled BTEVP(3.8) at 150 K with a visualization of the XCCA process. q_1 is here the value for the signal from the PMO at an angle ϕ_1 while q_2 is that of the (002) peak of hexagonal ice at an angle $\phi_2 = \phi_1 + \Delta$.

pendence. In order to determine an orientational dependence, X-ray Cross Correlation Analysis (XCCA) was conducted[48–51,114]. Following Eq. 5.1, an angular correlation is calculated between spots at two different q-values[46]. We choose one q-value to be the expected value for a (001) periodicity of the functional groups of the PMO and the other that of hexagonal ice (see Fig. 5.7).

5.3.1 Application of XCCA

The background of XCCA is explained in further detail in Sec. 2.1.3. Briefly summarized, the intensity $I(q_1, \phi)$ at q_1 and azimuthal angle ϕ is correlated with $I(q_2, \phi + \Delta)$ as

$$C(q_1, q_2, \Delta) = \frac{\langle I(q_1, \phi) I(q_2, \phi + \Delta) \rangle_\phi}{\langle I(q_1, \phi) \rangle \langle I(q_2, \phi) \rangle_\phi}. \tag{5.1}$$

If the q values related to peaks from the PMO structure are now chosen as q_1 and those related to ice structure as q_2 (cf. Fig. 5.7), the resulting correlation function $C(\Delta)$ gives a statistical insight into common angles Δ between the scattering planes of the PMO and the ice crystallites (see discussion below).[46,47] Fig. 5.7 shows an exemplary detector image from this experiment. The spots from the $(00l)$ reflections are clearly visible, *e.g.* the one marked with (q_1, ϕ_1). The spot marked with (q_2, ϕ_2) relates to the ice formed in the pore. It is much narrower compared to that of the PMO. Fig. 5.8shows three detector images of the same sample but measured at different locations in the sample. One observes that the Bragg reflections of the PMO material and ice appear at different locations and with varying intensity on the detector. As described above, the intensities of the PMO and ice reflexes are correlated in respect to the azimuthal angles between them. This is done for all detector images in order to asses the presence of preferred orientations of the ice crystals relative to the pore.

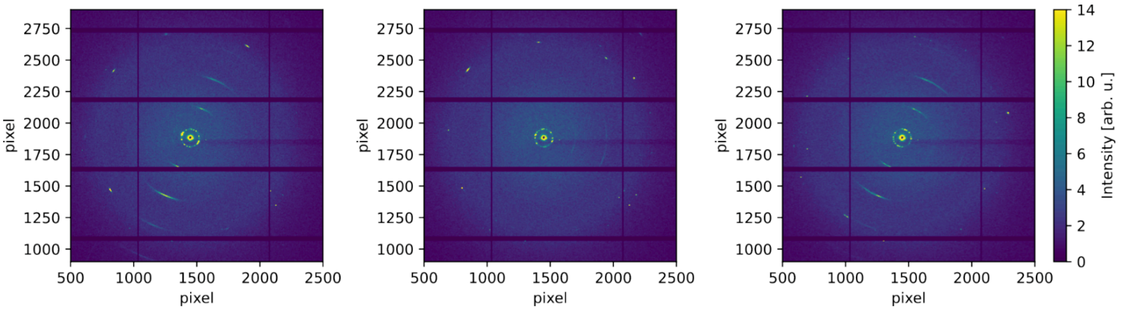

Figure 5.8: Nanofocused scattering detector images of the same sample at different locations in the sample.

5.3.2 Measurements and XCCA corrections

The data presented in this chapter was obtained during the experiment described in Section 3.3. At a constant temperature of 150 K, X-ray scattering patterns were taken at 105 unique spots for each sample, arranged in rows of 21 spots, as illustrated in Fig. 5.9B. Fig. 5.9A exemplary shows the azimuthally integrated intensity of all measured signals in BTEVP(3.8). Each scan, and therefore each subfigure, is equivalent to one row of measurement spots. In some signals, most prominently in the upper most signals of scans 11 and 12, larger ice peaks are present. These probably come from bulk ice forming outside of the pores, as these are also the measurements at the outermost spots in the sample capillary. In order to exclude XCCA contributions from this bulk ice, these measurements were not taken into account during the correlation analysis.

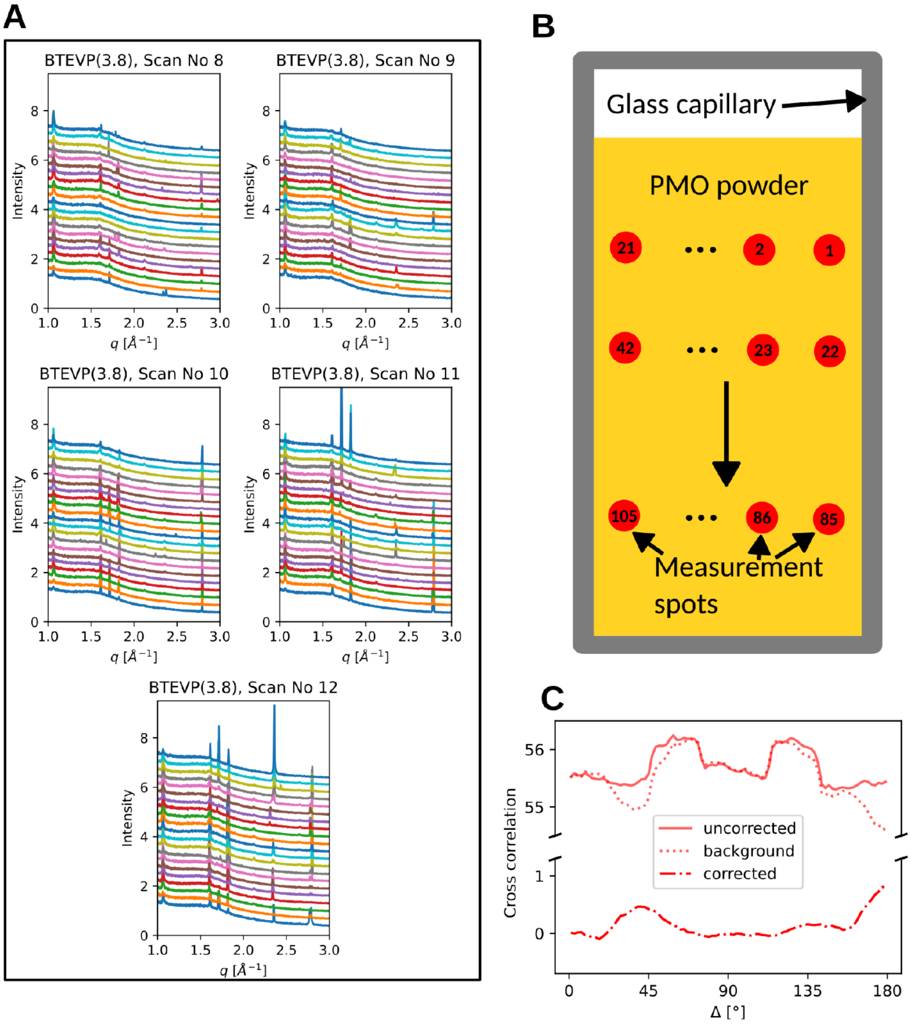

Figure 5.9: **A** X-ray scattering signals of each individual shot in BTEVP(3.8) at 150 K. **B** Pattern of the spots at which X-ray scattering patterns were taken. **C** Original (solid), background (dotted) and corrected (dash-dotted) correlation functions of BTEVP+(3.5).

When XCCA is applied, artificial contributions to the correlation functions can occur. These have their origin for example in sensitivity differences in the detector pixels and stray or parasitic light. In order to mitigate these background correlations, a correction was applied. In this correction, correlation between PMO and ice peaks were calculated where the two peaks come from unrelated measurement points. For example, the (001) PMO peak from image 1 was correlated with the (002) ice peak from images 2 through 105 (cf. Fig. 5.9B). Analogous to Eq. 5.1, this can be described for one pair of images as

$$C_{m,n}(q_1, q_2, \Delta) = \frac{\langle I_m(q_1, \phi) I_n(q_2, \phi + \Delta) \rangle_\phi}{\langle I_m(q_1, \phi) \rangle \langle I_n(q_2, \phi) \rangle_\phi}, \tag{5.2}$$

where m and $n \neq m$ are the indices of the images. These were calculated for a large number of image combinations and then averaged to produce the background correlation. Fig. 5.9C shows the original correlation function of BTEVP+(3.5), along with the background correlation and the corrected signal. One observes that the background correlations are the main contributor to the amplitude of the original signal. The background subtraction is therefore crucial to obtain meaningful information from these cross correlations.

5.3.3 Regions of interest for XCCA

As discussed in Sec. 5.2, the lattice constants of ice in PMOs change in comparison to bulk ice, causing a shift of the corresponding peak. This effect also appeared in some samples in the $I(q)$ of the nanofocus X-ray scattering experiment, specifically in BTEVP(3.8). Fig.5.10 shows the area of the characteristic ice $\mathrm{I_h}$ triplet peak in the measured samples. In BTEVP(3.8), the three peaks all show a bimodality with one of the modes located exactly at the bulk peak position. This is an indication that bulk ice formation has occured in this sample, as already discussed in the section above. One observes that when removing the suspected bulk contributions, these these modes decrease in intensity, confirming that the removal of the bulk contaminated shots improves the quality of the data for XCCA purposes.

For the implementation of XCCA, regions of interest (ROIs) around the relevant peaks were defined. The intensity values inside these ROIs at a given angle ϕ were then averaged in order to obtain the value used in the correlation. The ROIs for all peaks are shown in Fig. 5.11 for the example of BTEVP(3.8), once in polar coordinates and once in the averaged $I(q)$. Note that only the second and third PMO peak, as well as the second ice peak were used in the further analysis.

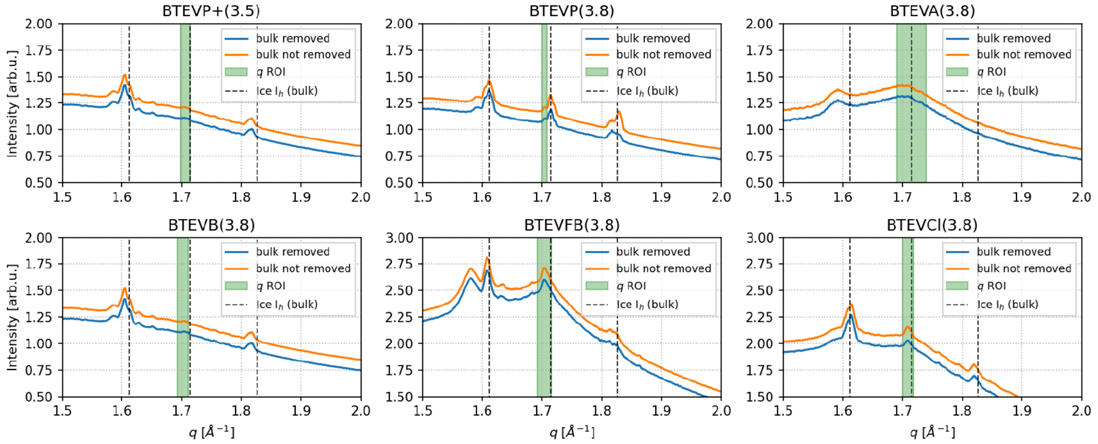

Figure 5.10: Regions of interest (ROIs) for the (002) ice peak in the measured samples. The plots show the $I(q)$, averaged over all considered measurements for each sample. Once with suspected bulk contributions removed (blue) and and once with them included (orange). The ROIs are marked in green and the bulk peak positions with a dashed line.

5.3.4 Orientation of ice crystals in PMO pores

Figure 5.12 shows a selection of correlation functions in PMOs with 3.8 nm pore diameter. The correlations between the (002)-peak of ice with both the (001) and (002)-peaks of the PMOs are shown in the subfigures 5.12A and 5.12B, respectively. The latter represent the periodicity of the functional groups in the pore walls and therefore the pore axis direction. Since $(001)_{\mathrm{PMO}}$ and $(002)_{\mathrm{PMO}}$ are parallel, both correlations should show the same qualitative features. Their equivalence can therefore be used as an additional indication if visible peaks are actual angular correlations or just artifacts, for example from detector noise, background scattering or limited statistical accuracy. Note that the angles of the correlation peaks are statistical values that indicate a preferred orientation. Other orientations might also be present inside one pore. The analysis is therefore sensitive to the specific area where the scattering pattern was taken.

The correlation functions in some materials show very clear peaks, while others do not. The presence of peaks implies that some materials lead to certain angles Δ between the (001)-axis of the ice crystals and the pore axis being more common than others. The absence of peaks can either mean the absence of ice crystals in these materials or random orientations of crystals with respect to the pore axis. For the hydrophilic samples (red), BTEVP+(3.5) shows a large peak at 180°, indicating a preferred prientation of

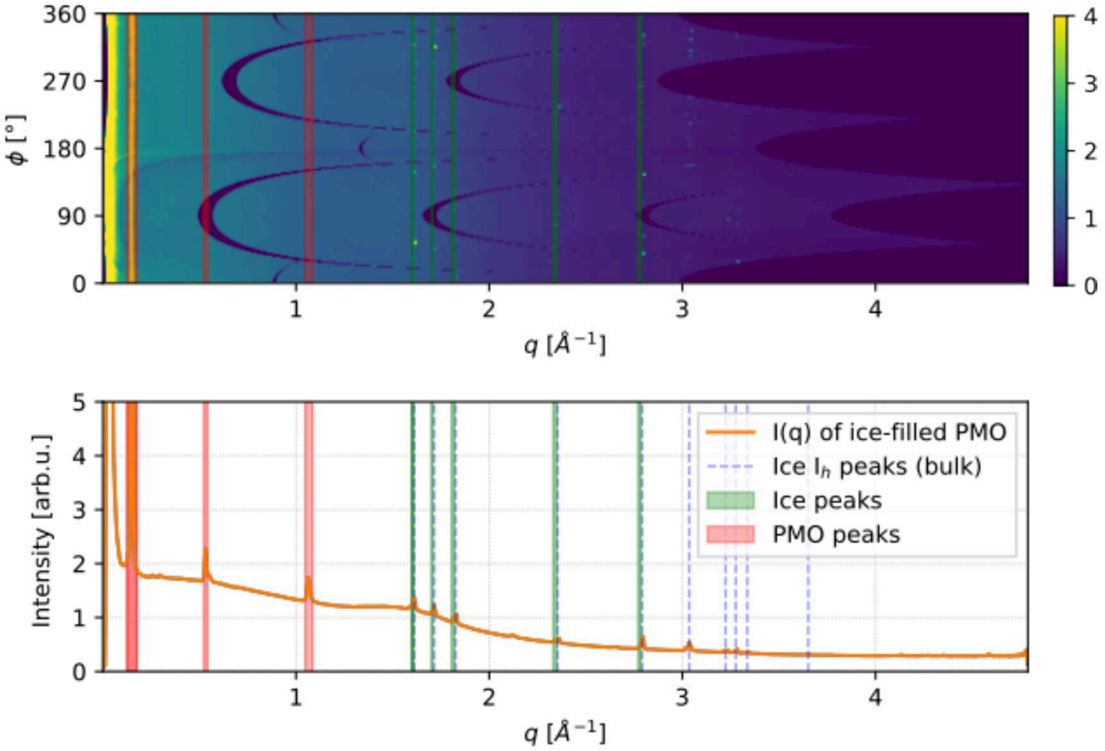

Figure 5.11: Regions of interest of the PMO (red) and ice peaks (green) for the example BTEVP(3.8). The upper plot shows the averaged detector image in polar coordinates, while the lower plot shows the averaged $I(q)$. Here, the bulk ice peak positions are also plotted for reference.

the (00l) axis of the ice parallel to the pore axis. A second large peak can be seen at about 40°. BTEVP(3.8) shows a quite large peak at about 30° and some smaller ones at approximately 60°, 120° and 150°. BTEVA(3.8) primarily shows a peak at 90°, albeit less pronounced than in BTEVP(3.8). In contrast, the more hydrophobic samples, BTEVB(3.8) also shows some pronounced peaks at 30°, 150° and two peaks slightly above and below 90°, respectively. BTEVFB(3.8) only shows some weak peaks at 150°, 75° and 30°, although the latter is only visible in the correlation with $(002)_{\mathrm{PMO}}$. BTEVCl(3.8) does not show any peaks at all. As the latter two are rather hydrophobic materials, the data presented in Fig. 5.12 generally suggests stronger correlations between the pore and ice crystal orientation in hydrophilic compared to hydrophobic pores with the exception of BTEVB(3.8). However, in those samples that show strong peaks (*i.e.* BTEVB(3.8), BTEVA(3.8), BTEVP(3.8), BTEVP+(3.5)), no systematic dependence of the correlation

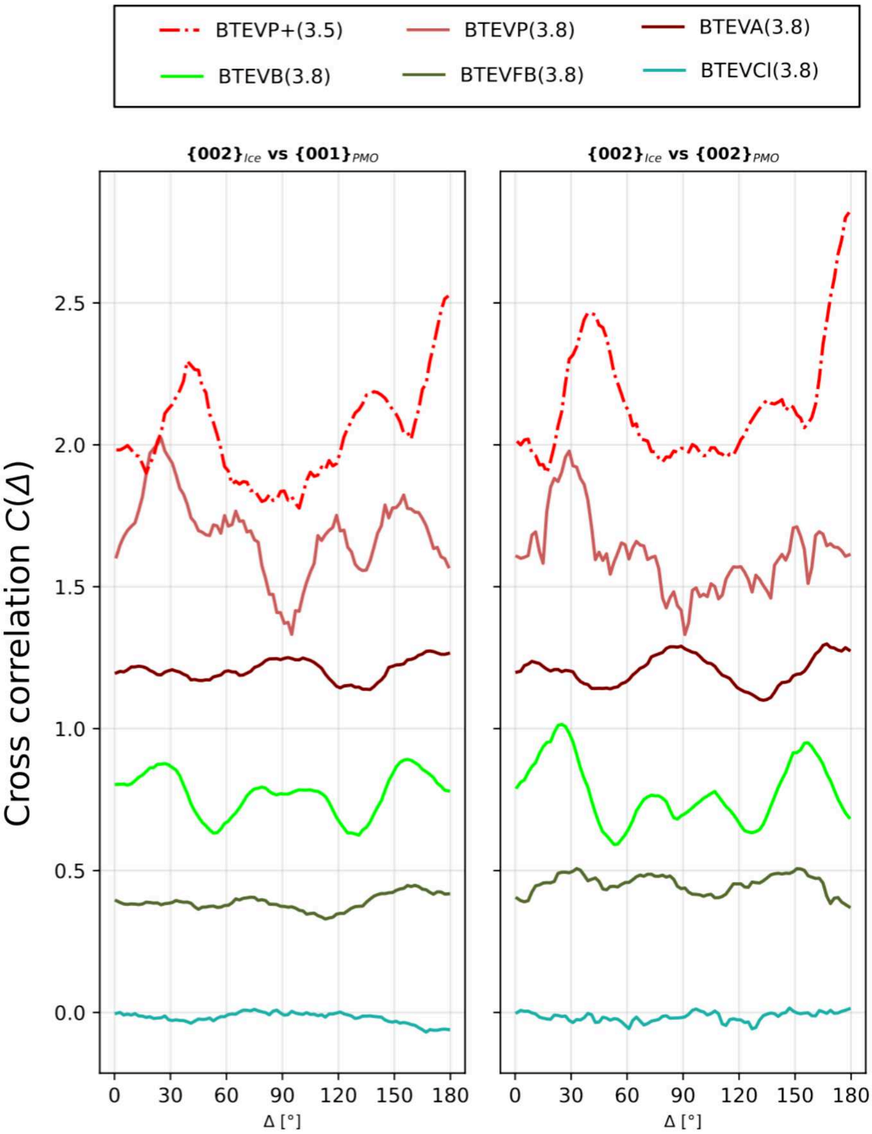

Figure 5.12: Angular correlations between spots of the (002) signals of hexagonal ice and the (001) (panel A) and (002) (panel B) of the functional groups of various PMOs. The plots are shifted vertically for clarity.

angles Δ on the material properties can be determined at these pore diameters but it is notable that BTEVP+(3.5) shows the largest peak out of all measured materials while also having the lowest pore diameter and volume.

Note that the absence of correlation peaks in BTEVFB(3.8) and BTEVCl(3.8) does not necessarily imply that no preferred orientations occur in these samples. Instead, it is also possible that the amount of averaged spots is too small in these cases and more data would be required to reach a convergence. In any case, if preferred orientations are present, they are much more weakly pronounced in comparison to the other samples.

5.4 Comparison of angular correlations and lattice parameter shifts

Figure 5.13 compares the lattice constants (panel A) with the angular correlation functions (panel B) for samples measured in both experiments. The obtained ice crystal orientations relative to the pore axis in these samples are visualized in Fig. 5.13C. A striking observation is that BTEVP+(3.4), which showed a strong unit cell elongation along the *c*-axis, also gives a strong correlation at 180°. This suggests that the elongated cells are often oriented along the pore axis. Additionally, another strong peak at about 45° and a third smaller peak at about 140° are visible. BTEVA(3.8), which closely sticks to the bulk lattice parameters, seems to be mostly oriented orthogonal to the pore axis as can be seen from its correlation peak at 90°. Smaller peaks at around 15° and 165° are also present. The correlations in BTEVB(3.8), which is the only measured PMO to exclusively show cubic-like ice characteristics, have two strong, symmetric correlation peaks at 30° and 150° and additionally two smaller peaks at about 75° and 105°, which are also symmetric. BTEVP(3.5) shows a strong peak at 30° and generally has a similar profile to BTEVP+(3.4) with no correlation at 90° and an additional small peak at around 150°, symmetric to its large peak at 30°. Both of these materials have the same functional pyridine group, but in BTEVP+(3.4), this group possesses an additional positive charge, a methyl group and the iodide counterion mentioned before.

5.5 Summary

The overall structure of ice confined in PMOs, consisting of cubic, hexagonal and amorphous contributions, which stem from the liquid layer at the pore wall[22,23], is well in

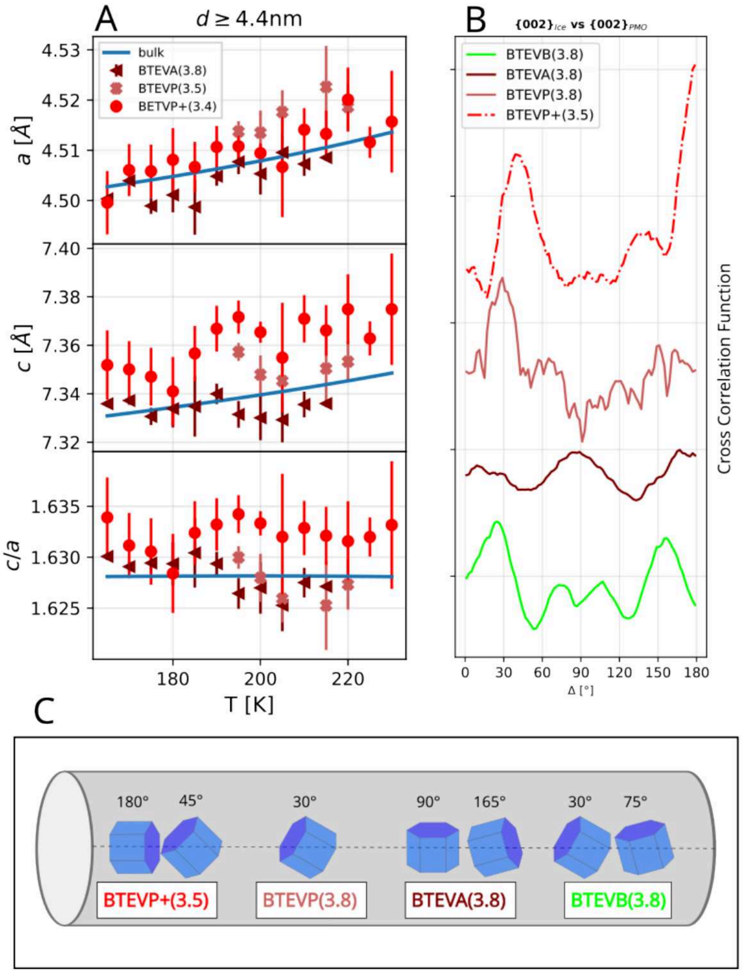

Figure 5.13: Comparison of lattice constants and correlation functions. **A** Lattice constants of materials for which XCCA was also conducted. **B** Angular correlation curves for materials in A. The correlations are for angles between spots at q-values identified for the (002) peak in hexagonal ice and the (002) peak of the functional group periodicity in the PMO. **C** A visualization of the most prominent angles Δ as shown in B. The gray cylinder represents the pore, the black dashed line the pore axis and the blue hexagonal prisms hexagonal crystallites.

accordance with literature.[22,23,72,89,110,111] We furthermore found indications that the structure is dependent on the way the sample is cooled. We consistently observed hexagonal contributions when lowering the temperature in a step-wise manner, while continuous cooling led to pure cubic (or cubic-like) ice.

While previous studies did not report lattice constant shifts of the hexagonal phase in confinement,[23] we observe that they deviate from bulk ice in several of our measured samples. This effect depends on both the pore surface chemistry and the pore size of the confining material. All of the hydrophobically functionalized materials discussed in this study, *i.e.* BTEVFB(4.9), BTEVFB(4.4) and BTEB(3.8), show a deviation from bulk properties, while in hydrophilic materials, this effect is mostly observable for small pore diameters $\leq 3.8\,\mathrm{nm}$. These shifts therefore seem to be dependent on both the pore wall chemistry and especially the pore size as stronger shifts were observed in smaller pores (*i.e.* BTEVP(3.7), BTEVP+(3.5), BTEVA(3.4)). We most commonly observe an increased c/a ratio, meaning an elongation of the unit cell (see Fig. 5.6).

Cubic or stacking disordered ice and an amorphous non-freezing layer have consistently been reported in similar pores in various studies.[22,23,111,115] The broad peaks observed in our data are in agreement with the argumentation of Morishige *et al.*[115] and Moore *et al.*,[22] that confined cubic ice consists of small crystallites with a large number of stacking faults to such a degree that it is better described as stacking disordered ice.[65]

The sharp ice $\mathrm{I_h}$ peaks that are observed in these systems were argued by Thangswamy *et al.*[111] to be in fact not hexagonal ice inside the pore but ice that crept out of the pore during crystallization, forming bulk crystallites outside the pore, as suggested by a calculated crystallite size that is considerably larger than the pore diameter.[111] In this study, similarly sized crystallites were found, calculated to be around 20 to 30 nm. However, it can be assumed that the hexagonal contribution is in fact ice inside the pores. The sharpness of the corresponding peaks and the implied large crystallite size does not necessarily mean that they have to be outside of the pore. Instead they could be caused by crystallites grown along the pore axis with the crystallite size describing the length of a cylindrical crystallite. This way, it is in principle only limited by the length of the pore. This is supported by the fact that larger pores lead to larger hexagonal peaks, as in BTEVFB(4.9) or BTEVA(4.4) compared to smaller pores such as BTEVP(3.5) or BTEVP+(3.4). Furthermore, we observe the previously discussed deviations in the lattice parameters of the hexagonal contributions from those of bulk ice, both in the powder and nanofocused X-ray scattering experiments.

XCCA suggests preferred orientations of the hexagonal contributions in some samples (see Figs. 5.12 and Fig. 5.13). For a pore diameter of about 3.8 nm, it is found that stronger correlations tend to occur in more hydrophilic pores. When comparing the XCCA results to the lattice parameter shifts in specific samples (Fig. 5.13), more prominent correlations are found in samples that also exhibit larger lattice parameter shifts (*e.g.* BTEVP+(3.5)) or exclusively cubic-like ice (BTEVB(3.8)), implying a close connection between the general structure of the ice and the orientation of its crystallites. Constraints in the form of small pore diameters and pore wall functionalization may influence the crystal formation such that specific orientations are preferred. These could in turn change the lattice parameters of the crystal. Note that the preferred orientations are mostly observed in PMOs with hydrophilic moieties, which also show the strongest density decrease and tetrahedral structuring in liquid water (see Chapter 4). This implies that the observed behavior of lattice parameter shifts and preferred orientation may be a result of the altered structure of liquid water under PMO confinement.

6 Structural influence of water adsorption on PMOs

It was mentioned in Section 4.1 that the Bragg peaks from PMO periodicities had to be removed in order to analyze the water signal. This is because the adsorption of water influences the structure of the PMOs themselves, leading to changes in the peak position and intensity in the PMO peaks. A comparison of empty and H_2O-filled X-ray scattering signals of BTEVA(4.4), as well as the subtracted signal, are shown in Fig.6.1 as an example. Fig. 6.1A shows the q-range relevant for the water signal while Fig. 6.1B focuses on the (001) and (002) PMO peaks. Especially in Fig. 6.1B, changes in the peaks are observed, resulting in artifacts in the subtracted signal. Both the peak position and the intensity are affected by water adsorption. These changes in the $(00l)$ PMO peaks will be further investigated in the following chapter by focusing on the PMOs instead of the water signals. This was achieved by using in-situ X-ray scattering during the water adsorption into the pores, following the experimental description in Section 3.3.

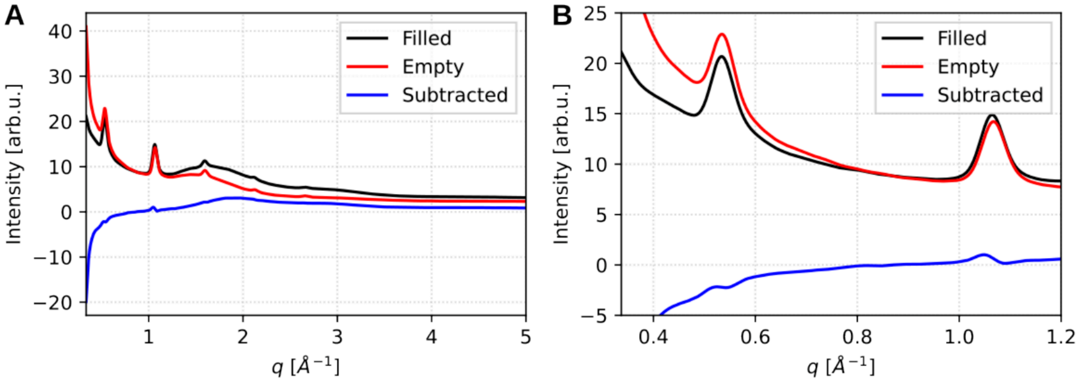

Figure 6.1: Filled, empty and subtracted X-ray scattering signals of BTEVA(4.4) in the q-range relevant for the water signal (**A**) and in the range of the (001) and (002) PMO peaks (**B**). Data was obtained in the experiment at P02.1, described in Section 3.2.

6.1 In-situ X-ray scattering signals of PMOs during adsorption

The azimuthally integrated X-ray scattering intensity signals for the measured PMOs at relative humidities of 0 and 100 %RH are shown in Fig. 6.2. One observes that difference in intensity at the two humidities are barely, if at all, visible in this scaling, indicating that the contribution of the adsorbed water must be small. In fact, the adsorption of water can not be verified just from these signals. Note especially the signals of BTEVA(4.4), which show a much smaller difference than in the data presented in Fig. 6.1. This could be explained by the way the water was adsorbed in the P02.1 experiment. Here, the powder was exposed to water vapor in a climate chamber for 1-2 days, while the adsorption in the in-situ X-ray scattering experiment took place in about 1-2 hours. Furthermore, only a fraction of the powder was directly exposed to water vapor in the in-situ experiment. This, combined with the fact that only the relative humidity in the humidifier is known, could lead to relative humidities at the sample that are in fact lower than the given value.

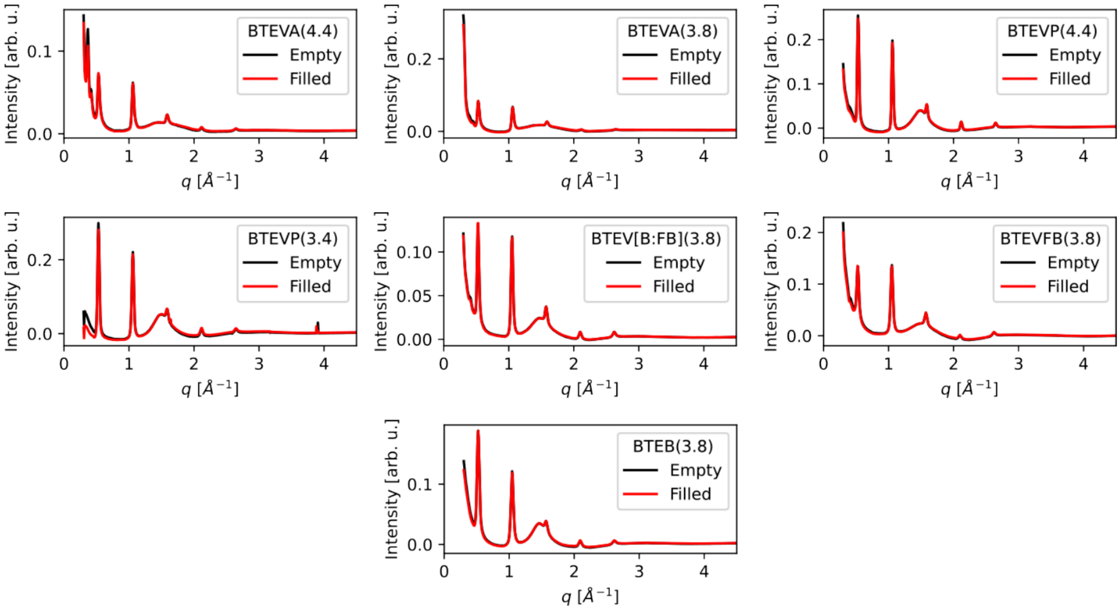

Figure 6.2: $I(q)$ of PMOs at 0 and 100 %RH.

Only in BTEVP(3.4) the two curves are distinguishable in the relevant q-range (between 1 and $4\,\text{Å}^{-1}$). A visible effect presents itself in changes of the intensity of the first and/or second diffraction peak from the PMO (*i.e.* the peaks at $q \approx 0.5\,\text{Å}^{-1}$ and $q \approx 0.5\,\text{Å}^{-1}$).

Specifically, both peaks decrease in intensity at high relative humidity in BTEVP(4.4) and BTEVP(3.4), while in the remaining samples, only the second peaks shows a clear decrease. A shift in q is not visible in the presented scaling in either of the materials. A further investigation of the changes in the PMO peak positions and intensities is conducted in Sec. 6.3.

6.2 Verification of water adsorption

As a water signal can not be identified directly from the X-ray scattering signals presented in Fig. 6.2, this section aims at verifying that water adsorption has occured during the in-situ measurements. For this, the water signal has been extracted, as explained in Sec. 4.1. The extracted water signals for 70, 80, 90 and 100 %RH are shown in Fig. 6.3. Water signals are observed in all samples, verifying the adsorption process. Background measurements at all relative humidities are subtracted to ensure that the water signals do not originate from the water vapor in the experimental cell.

A striking observation is that at 90 and 100 %RH, the strongest water signal is present in BTEVP(3.4). This is surprising but can be explained by excess water. As it has the smallest pore diameter, and is furthermore rather hydrophilic, the water is probably adsorbed and condensated already at lower relative humidities than the other samples. This is most likely the case between 70 and 80 %RH, as the water signal is similar to the other samples at 80 %RH, despite its smaller pore diameter and therefore pore volume. In contrast, there is no water signal present in BTEVP(3.4) at 70 %RH. Further condensation could then occur outside the pore leading to intergranular excess water. In fact, this process is possible in all measured samples, however, due to the otherwise more uniform water signal intensity, it is reasonable to assume that this did not take place.

The water signal with the lowest intensity at 100 %RH is observed in BTEV[B:FB](3.8), which could be explained by its organic moieties. This material possesses alternating fluorinated and unfluorinated BTEVB and BTEVFB groups, which are both rather hydrophobic. This arrangement may have the effect that it is very unfavorable for water to adsorb into the pore, as the condensation first happens at the pore wall.

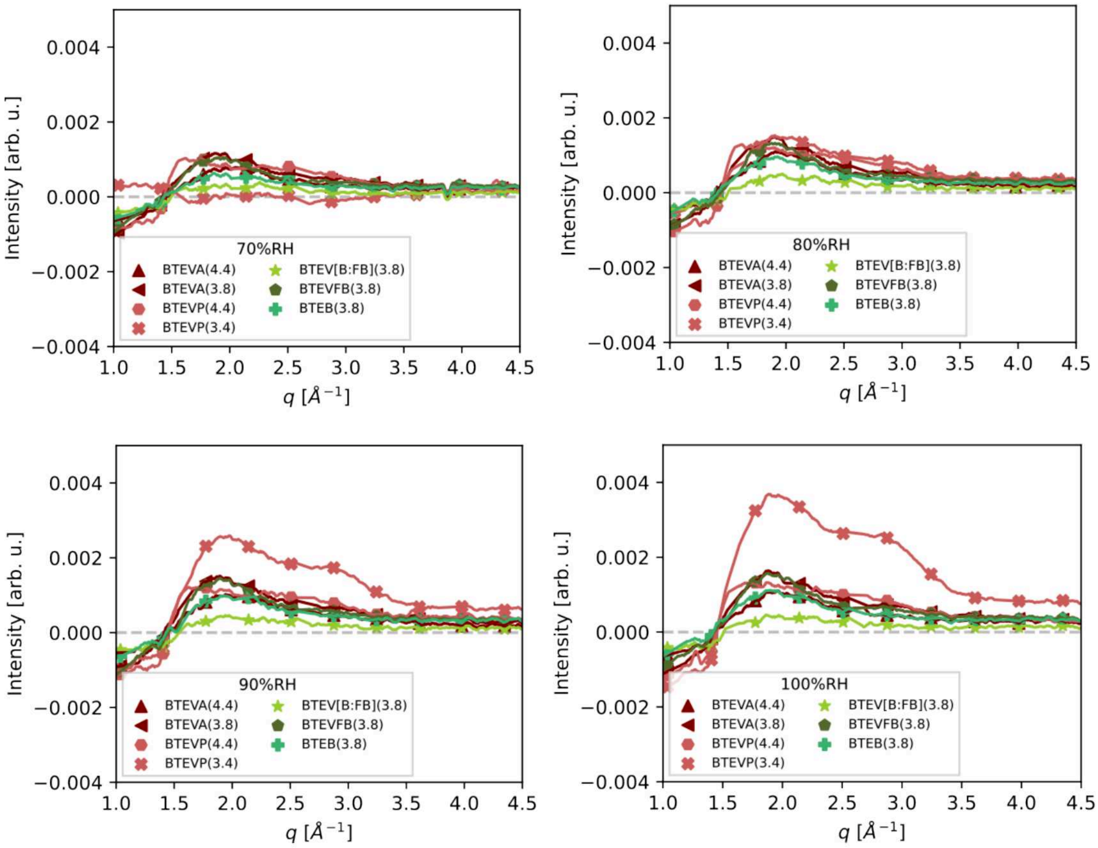

Figure 6.3: Extracted water signals of in the in-situ filled PMOs at relative humidities of 70, 80, 90 and 100 %RH.

6.3 Changes in the PMO peaks

The X-ray scattering signals in Fig. 6.2 already gave some hints on the effect of water adsorption into the PMO pores. After verifying the water adsorption, this section aims to more closely investigate the changes of the PMO peaks.

The two panels on the left of Fig. 6.4 show the change in the scattering plane distance $\Delta d = 2\pi \left(\frac{1}{q_{\mathrm{H}}} - \frac{1}{q_0} \right)$ for the first and second peak, where q_0 is the peak maximum at 0 %RH and q_{H} that at relative humidity H. The upper panel shows the values obtained from the first peak, located at $q \approx 0.5\,\text{Å}^{-1}$. This peak corresponds to the (001) Bragg reflection, which is caused by the periodicity of the organic moieties in the pore wall. Specifically, the distance $d = 2\pi/q$ obtained from the peak position describes the length of one group. Δd then gives the difference between this length at 0 %RH and at relative humidity H.

Here, one observes varying behavior between the materials. While Δd stays roughly around 0 in the BTEVP materials and BTEVA(3.8), it increases with the humidity in pores with hydrophobic moieties, *i.e.* BTEV[B:FB](3.8), BTEVFB(3.8) and BTEB(3.8). A less pronounced increase is also observed in BTEVA(4.4). While the values of these changes are rather small ($< 0.02\,\text{Å}$) and the error margins quite large in comparison, this still hints at a restructuring effect within the PMO material. Note that in the second peak, the difference in behavior between the materials is not as stark as in the first peak and distinctions between the materials cannot be meaningfully identified.

The two panels on the right of Fig. 6.4 show the relative change in the integrated intensity of the two peaks. Again, the behavior of the materials is not uniform, especially in the first peak. In the BTEVA, BTEVFB(3.8) and BTE[B:FB](3.8), an increase of the intensity is observed. BTEB shows a relatively stable peak that does not increase as much as the ones mentioned before. In the BTEVP samples, the behavior is reversed, with the peak intensity decreasing with increasing relative humidity. In the second peak, all materials show a decrease in the peak intensity. However, the decrease is still strongest in the BTEVP samples and lowest in the hydrophobically functionalized materials.

The changes in the PMO peaks can be explained by the interaction of water with the functional groups in the pore wall. The decrease of the peak maximum in BTEVP suggests a lower degree of order of the organic moieties. This could be invoked by different configurations of the NH group of the pyridine. This group is able to rotate and therefore lead to non-identical configurations between different instances of the moiety.

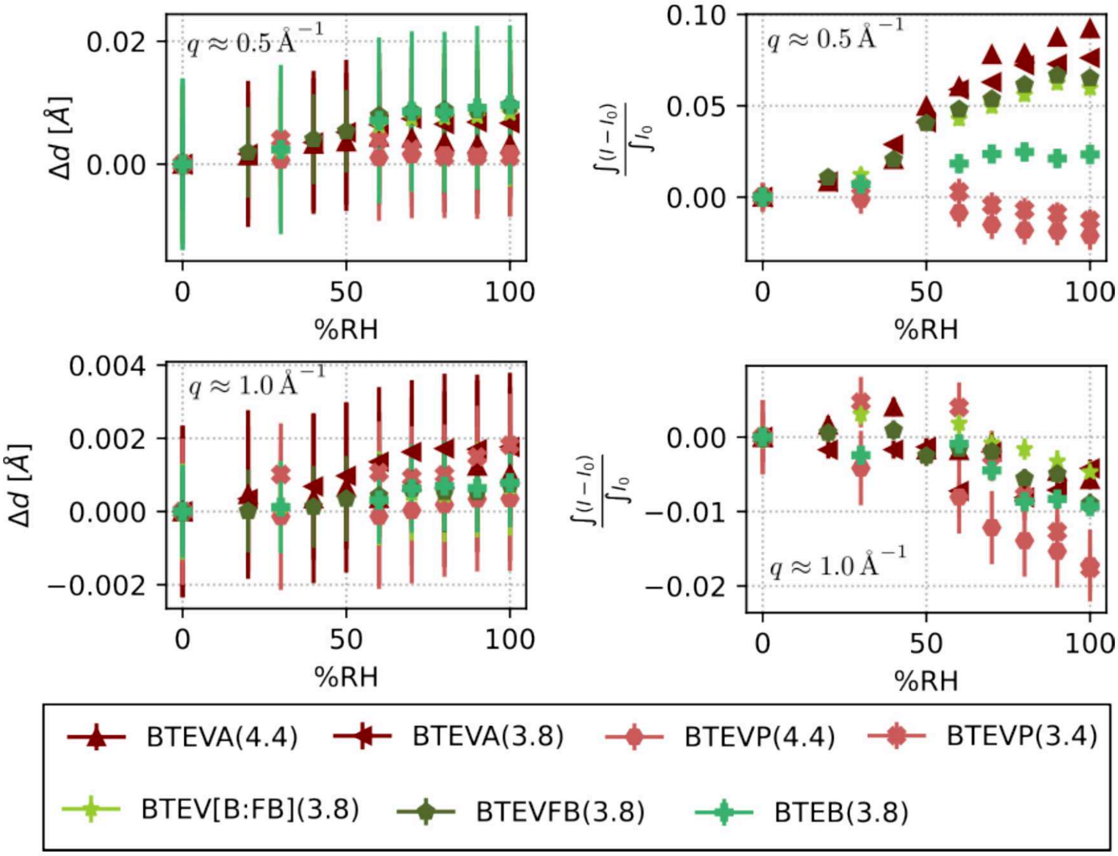

Figure 6.4: The change of the interplanar distance Δd (panels on the left) and integrated peak intensity (panels on the right) over relative humidity for the first and second $(00l)$ PMO peaks. The first peak is located at $q \approx 0.5\,\text{Å}^{-1}$ and the second at $q \approx 1.0\,\text{Å}^{-1}$.

When these non-identical groups interact with water, this could then lead to a decrease in the order of the organic moieties, as this interaction would then not be uniform throughout the pore wall. The discussion in Chapter 4 has shown that water interacts rather strongly with BTEVP.

The fluorine group in BTEVFB has a similar capability to rotate (see Fig. 6.5). However, in this material, an increase of the peak maximum, and therefore an increase in the order of the moieties, is observed. This discrepancy could be explained by the fact that the fluorine group acts hydrophobically. This leads to the space around it not being occupied by water, similar to the B-PMO shown in Fig. 2.13B. The uniform interaction with the silica between the organic moieties could then lead to an increase in the order of the moieties. As the water interacts strongly with the hydrophilic silica but not with the organic moiety, the occupancy of water molecules in the space between the moieties should be rather high, leading to the moieties being pushed apart by the water. This could then also explain the increase of Δd in the left panel.

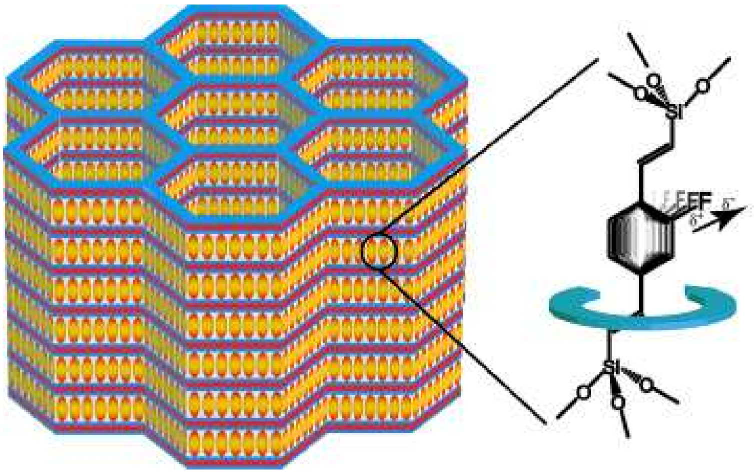

Figure 6.5: Visualization of the rotation of a moiety in a BTEVFB-PMO. Reused from Bracco *et al.*[29] with permission from *John Wiley and Sons.*

A similar behavior would be expected for BTEB(3.8), as this also constitutes a PMO with hydrophobic organic moieties. However, the distance between these is much smaller than in BTEVFB(3.8) (see Tab. 3.1). Because of this, the amount of silica between the moieties with which the water can interact is also lower, leading potentially to a weaker force on the material and therefore less restructuring of the pore material.

The last materials in this study are BTEVA with pore diameters of 3.8 and 4.4 nm.

In these, an increase in the peak maximum is also observed in the first peak. Notably, in BTEVA(3.8), the adsorption of water also induces a shift of the peak position to larger distances, while this is not the case in BTEVA(4.4).

An interesting discrepancy in the results presented in Fig. 6.4 is that in the peak intensities, the behavior in the first peak between the samples is different than in the second. While there is diverging behavior between the materials in the first peak, it decreases slightly in all of them in the second peak. As both peaks are identified with the periodicity of the organic moieties (*i.e.* (001) for the peak at $q \approx 0.5\,\text{Å}^{-1}$ and (002) for the peak at $q \approx 1.0\,\text{Å}^{-1}$), it is expected that these peaks should behave similarly. An explanation for this variation could be the change of X-ray contrast between the pore wall and its center when water gets adsorbed. As water has a higher electron density than air, a higher scattered intensity will be present from water than from air. Therefore, the ratio between the integrated intensity that is scattered from the pore wall material to that inside the pore is shifted towards the latter in the case of water-filled pores. This effect probably exists in combination with the physical effect discussed above. However, for peaks at larger q, the decrease in contrast might become dominant, leading to the apparent intensity decrease. An additional factor could be the signal of the water, which is more strongly present in the second peak. As it is rather broad compared to the Bragg peaks of the PMOs, it describes a background contribution in this context. When isolating the PMO peaks, these could therefore appear smaller in comparison to the empty PMO, as more intensity gets subtracted when isolating the peak.

The presence of the physical restructuring and the decrease in contrast is also supported by the fact that, while the peak maximum decreases in all samples in the second peak, the order of the materials is similar to that in the first peak with BTEVP at the bottom (*i.e.* with a stronger intensity decrease) and more hydrophobic materials and BTEVA at the top (*i.e.* with a weaker intensity decrease). This indicates that while the contrast decrease might be the dominant effect for this peak, there might be another influence in the form of the aforementioned restructuring effect.

6.4 Summary

The in-situ study of water being adsorbed into PMOs confirms changes in the Bragg peaks originating from the PMO moiety periodicities during water adsorption. By isolating the contribution of the adsorbed water, it was confirmed that the process was successful. However, the amount of water is most likely lower than in the experiments where the pores were filled ex-situ, as indicated by a barely noticeable difference between the X-ray scattering signals at 0 and 100 %RH. This is most likely due to the longer and more even exposure to water vapor in the climate chamber opposed to the experimental cell in the in-situ experiment.

The adsorption led to changes in both the peak position and the peak intensity, especially in the (001) peak, *i.e.* the first-order peak that is identified with the periodicity of the organic moieties in the PMO pore wall. Specifically the change in intensity varied throughout the set of samples. BTEVFB(3.8), BTEV[B:FB](3.8) and the two BTEVA samples showed an increase of the intensity with higher relative humidities, while it decreased in the BTEVP samples. The intensity of the (001) peak stayed roughly the same in BTEB(3.8). An increase of the intensity of implies a more ordered structure of the corresponding lattice planes, while a decrease suggests the opposite. The hydrophobic or hydrophilic interaction of the moieties with water might therefore cause a restructuring of the moieties, which decreases the order in BTEVP, while increasing it in the other samples. BTEB is not as strongly affected as the distance between two groups is much smaller than in the other materials, leading to a weaker effect.

In the (002)-peak, a decrease of the intensity is observed in all samples. This can be explained by a decrease of the X-ray contrast between the pore wall material and the pore center. As this is not observed in the (001)-reflection, this might become a dominant effect only at larger q. Additionally, the water signal also contributes more strongly at larger q (*i.e.* at $q \approx 1\,\text{Å}^{-1}$). This means a stronger background signal that is difficult to mitigate when isolating the PMO peak. Therefore the intensity of the peak itself may appear lower than it is.

Previous studies of the influence of water adsorption on the structure of porous silica showed that repeated adsorption leads to changes in the SAXS regime in SBA-15, *i.e.* the ($hk0$) peaks of the material.[116] The discussion in this chapter showed, that also in the WAXS regime, *i.e.* the ($00l$) peaks of the PMOs, is affected by the adsorption. While this study does not reveal if the process is repeatable and is based on only one adsorption cycle, it still presents interesting results, especially since not many studies are conducted regarding the WAXS regime in this context.

7 Conclusion

The aim of this thesis was to explore the interactions between water and ice with confining PMO materials, using X-ray scattering. The structure of liquid water (Chapter 4) and ice (Chapter 5) under confinement was investigated, as well as the influence that the adsorbed water has on the PMO material (Chapter 6). The findings present the first X-ray scattering study of water under confinement in a broad range of different PMO materials with a large selection of PMO precursors and pore diameters.

Probing the structure factor of liquid water in PMOs revealed a decrease in its density when compared to bulk water. While this effect was present in all measured PMOs, notable differences between the various materials were observed. The water confined in hydrophobically functionalized PMOs retained a density closer to that of bulk water, while in hydrophilic pores, it differed more from bulk. This observation experimentally confirms previous simulation studies that propose a lowered density, specifically in hydrophilic confinement, due to negative pressures inside the pore.[19–21] This may be caused by meniscii,[21] which form at the pore opening, as well as bound water that adsorbs inside the pore wall, such that a clearly defined boundary between the wall and the water cannot be established anymore.[19]

The analysis of the pair distribution function and the running coordination number proposed that confinement in pores with hydrophilic moieties and smaller pore diameters supports the development of a more pronounced tetrahedral water network. This result is in disagreement with previous spectroscopy studies, which observe less tetrahedral structuring in PMOs.[31,36] As discussed before in Sections 2.2.3 and 4.5, there is a discrepancy between studies on confined water that use spectroscopy methods and those utilizing scattering and simulation techniques. The former tend to conclude less tetrahedrally structured water,[31,36,37] while the latter observe a more tetrahedrally structured network.[20,21,38,39] The results from this thesis therefore agree with the scattering studies that find more tetrahedral water, especially in silica confinement while disagreeing with previous spectroscopy-based studies of water in PMOs.

In PMO-confined ice, an X-ray scattering signal with various contributions was observed. In most materials the signal contained diffuse stacking-disordered, amorphous and hexagonal characteristics (see 5.1.2). This is in agreement with previous studies of ice in mesoporous silica confinement.[23,111] However, a new finding was the presence of a slight shift in the peaks from the hexagonal contribution. The corresponding lattice parameters a and c therefore differ when compared to bulk ice I_h. This shift varies for the PMO materials and is not isotropic in most materials. Instead an elongation of the cell is observed, in which the c-parameter changes more strongly than a, resulting in a larger ratio c/a compared to bulk ice.

Furthermore, preferred orientations of ice crystallites in respect to the pore were found in BTEVP+(3.5) and BTEVP(3.8) and to a lesser extent also in BTEVA(3.8) and BTEVB(3.8). From this it can be concluded that hydrophilic pore functionalization is connected to crystallites growing in preferred orientations. Notably, these are also the PMOs, which lead to the strongest density decrease and tetrahedral structuring in liquid water. This suggests that the emergence of preferred ice crystal orientations is caused by the strong pore wall-water interaction and the subsequent altered water structure.

Lastly, the effect of water adsorption on the structure of the PMO, specifically the periodicity of the organic moieties, was investigated. Here, a restructuring is observed in most of the measured materials, as indicated by changes in the peak positions and intensities of the (001) peaks of the PMOs during water adsorption. A growth in peak intensity, indicating a more ordered structure of the organic moieties, was present in all samples except BTEB(3.8) and the BTEVP materials. The structure in BTEB(3.8) was not strongly affected by the water adsorption, probably due to the short length of its moieties. BTEVP(4.4) and BTEVP(3.4) showed a decrease in the peak intensity, suggesting a decrease in the order of the functional groups. This could be caused by varying orientations of the moieties, as their structure allows for rotation along its long axis. This way, interactions of the strongly structured water network, which is present in these materials (see Sec. 4.5), with the rotated organic moieties might cause strains on the pore wall, leading to slight deformations.

It is important to note that the results presented in Chapters 4, 5 and 6 are closely linked and influence each other. Chapter 4 discussed that the structure of water is influenced by the PMO confinement. However, Chapter 6 showed that the PMO material is just as well impacted by the adsorption of water. It can be assumed that this results in a complex interplay between the two effects, where the PMO functionalization affects the water structure, which in turn alters the PMO structure and so on, until an equilibrium state is reached. When lowering the temperature, the resulting water structure most likely has a strong influence on the ice formation, as discussed in Chapter 5.

A striking observation that re-appears in the discussions is that confinement in PMOs with hydrophilic functionalization results in behavior that is most different from bulk water. This is especially the case for the structure factors (Sec. 4.3) and tetrahedral structuring (Sec. 4.5) in liquid water, as well as the emergence of preferred orientations of ice crystals (Secs. 5.3.4 and 5.4). A possible explanation for this phenomenon is that in the hydrophilic PMOs water can form hydrogen bonds with the silica, as well as the functional groups in the pore wall, thereby altering the water network directly. In contrast, the interaction with hydrophobic moieties is rather defined by an absence of bonds. As this is more of a indirect influence, the difference to bulk water may therefore not be as strongly pronounced as in hydrophilically functionalized PMOs.

These results once again underline the peculiarities of water, especially when it is subject to confinement. In particular, they imply that the interaction of water with a confining medium has a strong influence on its structural behavior. An example of this is the tetrahedral hydrogen-bond network, which has been shown to be affected by not only the geometry of the confinement but also the pore wall chemistry. Subsequently, the structure of ice forming in these pores is also affected.

Going forward, this could be used as a means to study fundamental properties of water and ice. Confinement could for example be utilized for supercooling while tuning the pore-water interaction such that the structure of the confined water is close to that of bulk water. From Chapter 4 one can infer that this could be achieved by using a hydrophilically functionalized PMO, as the structure factor peaks, as well as the amount of tetrahedral structuring in these are closest to bulk water (cf. Figs. 4.4, 4.7 and 4.8). One could also utilize confinement interface effects to induce specific structural properties. Examples of this are the lowered density of water presented in Sec. 4.3 or the ice leading to the diffuse cubic-like ice signal discussed in Sec. 5.1.2.

The influence of the water adsorption on the confining material is also of great interest with a number of studies investigating the imbibition of water into porous materials.[117,118] In this context, the findings from Chapter 6 could help to engineer new functional hybrid materials based on water in conjunction with tunable porous materials, which could for example serve as actuation materials.[119,120]

Generally, considering the prevalence of confined water and ice in nature, the interactions discussed above could be an important factor, for example in geological or biological contexts and should be considered when investigating water and ice in confinement.

Bibliography

[1] P. H. Gleick. *Water in crisis.* Vol. 100. New York: Oxford University Press, 1993.

[2] E. R. Buskirk and S. M. Puhl. *Body fluid balance: exercise and Sport.* Vol. 9. CRC Press, 1996.

[3] E. Camprubi et al. “The emergence of life”. In: *Space Sci. Rev.* 215.8 (2019), pp. 1–53.

[4] P. G. Debenedetti and H. E. Stanley. “Supercooled and glassy water”. In: *Physics Today* 56.6 (2003), pp. 40–46.

[5] P. Ball. “Water—an enduring mystery”. In: *Nature* 452.7185 (2008), pp. 291–292.

[6] P. Gallo et al. “Water: A tale of two liquids”. In: *Chem. Rev.* 116.13 (2016), pp. 7463–7500.

[7] L. G. M. Pettersson, R. H. Henchman, and A. Nilsson. “Water - The Most Anomalous Liquid”. In: *Chem. Rev.* 116.13 (2016), pp. 7459–7462.

[8] R. Shi and H. Tanaka. “The anomalies and criticality of liquid water”. In: *Proc. Natl. Acad. Sci. U.S.A.* 117.43 (2020), pp. 26591–26599.

[9] G. M. Kontogeorgis et al. “Water structure, properties and some applications–A review”. In: *Chem. Thermodyn. Therm. Anal.* 6 (2022), p. 100053.

[10] C. G. Salzmann et al. “The polymorphism of ice: five unresolved questions”. In: *Phys. Chem. Chem. Phys.* 13.41 (2011), pp. 18468–18480.

[11] D. Mariedahl et al. “X-ray scattering and O–O pair-distribution functions of amorphous ices”. In: *J. Phys. Chem. B* 122.30 (2018), pp. 7616–7624.

[12] C. G. Salzmann. “Advances in the experimental exploration of water’s phase diagram”. In: *J. Chem. Phys.* 150.6 (2019).

[13] M. Ladd-Parada et al. “Following the crystallization of amorphous ice after ultrafast laser heating”. In: *J. Phys. Chem. B* 126.11 (2022), pp. 2299–2307.

[14] W. H. Thompson. “Solvation dynamics and proton transfer in nanoconfined liquids”. In: *Annu. Rev. Phys. Chem.* 62 (2011), pp. 599–619.

[15] G. F. Reiter et al. “Anomalous ground state of the electrons in nanoconfined water”. In: *Phys. Rev. Lett.* 111.3 (2013), p. 036803.

[16] K. Kapoor, S. Patil, et al. “Viscoelasticity and shear thinning of nanoconfined water”. In: *Phys. Rev. E* 89.1 (2014), p. 013004.

[17] D. Munoz-Santiburcio and D. Marx. “Chemistry in nanoconfined water”. In: *Chem. Sci.* 8.5 (2017), pp. 3444–3452.

[18] S. Jähnert et al. “Melting and freezing of water in cylindrical silica nanopores”. In: *Phys. Chem. Chem. Phys.* 10.39 (2008), pp. 6039–6051.

[19] P. Gallo, M. A. Ricci, and M. Rovere. “Layer analysis of the structure of water confined in vycor glass”. In: *J. Chem. Phys.* 116.1 (2002), pp. 342–346.

[20] A. K. Soper. “Density profile of water confined in cylindrical pores in MCM-41 silica”. In: *J. Phys. Condens. Matter* 24.6 (2012), p. 064107.

[21] A. K. Soper. “Radical re-appraisal of water structure in hydrophilic confinement”. In: *Chem. Phys. Lett.* 590 (2013), pp. 1–15.

[22] E. B. Moore et al. “Freezing, melting and structure of ice in a hydrophilic nanopore”. In: *Phys. Chem. Chem. Phys.* 12.16 (2010), pp. 4124–4134.

[23] S. Mohammed et al. “Structure of ice confined in silica nanopores”. In: *Phys. Chem. Chem. Phys.* 23.22 (2021), pp. 12706–12717.

[24] S. Inagaki et al. “An ordered mesoporous organosilica hybrid material with a crystal-like wall structure”. In: *Nature* 416.6878 (2002), pp. 304–307.

[25] A. Sayari and W. Wang. “Molecularly ordered nanoporous organosilicates prepared with and without surfactants”. In: *J. Am. Chem. Soc.* 127.35 (2005), pp. 12194–12195.

[26] M. Cornelius, F. Hoffmann, and M. Fröba. “Periodic mesoporous organosilicas with a bifunctional conjugated organic unit and crystal-like pore walls”. In: *Chem. Mater.* 17.26 (2005), pp. 6674–6678.

[27] M. Beretta et al. “Towards peptide formation inside the channels of a new divinylaniline-bridged periodic mesoporous organosilica”. In: *Chem. Commun.* 46.14 (2010), pp. 2495–2497.

[28] M. Waki et al. “Crystal-like periodic mesoporous organosilica bearing pyridine units within the framework”. In: *Chem. Commun.* 46.43 (2010), pp. 8163–8165.

[29] S. Bracco et al. “Dipolar rotors orderly aligned in mesoporous fluorinated organosilica architectures”. In: *Angew. Chem., Int. Ed.* 54.16 (2015), pp. 4773–4777.

[30] S. Martens et al. “Periodic mesoporous organosilicas as adsorbents of toxic trace gases out of the ambient air”. In: *Z. anorg. allg. Chem.* 640.3-4 (2014), pp. 632–640.

[31] J. B. Mietner. “Zu Gast in Nanoporen: das große Potential von PMOs bei der Untersuchung der Eigenschaften von Wasser in Nanoporen unterschiedlicher Polarität”. Doctoral Dissertation. Staats-und Universitätsbibliothek Hamburg Carl von Ossietzky, 2018.

[32] J. B. Mietner et al. “Properties of water confined in periodic mesoporous organosilicas: nanoimprinting the local structure”. In: *Angew. Chem.* 56.40 (2017), pp. 12348–12351.

[33] J. B. Mietner, M. Fröba, and R. Valiullin. “Water Transport in Periodic Mesoporous Organosilica Materials”. In: *J. Phys. Chem. C* 122.24 (2018), pp. 12673–12680.

[34] A. Jani et al. “Dynamics of water confined in mesopores with variable surface interaction”. In: *J. Chem. Phys.* 154.9 (2021), p. 094505.

[35] B. Malfait et al. “Influence of pore surface chemistry on the rotational dynamics of nanoconfined water”. In: *J. Phys. Chem. C* 125.30 (2021), pp. 16864–16874.

[36] B. Malfait et al. “Structure of water at hydrophilic and hydrophobic interfaces: Raman spectroscopy of water confined in periodic mesoporous (organo) silicas”. In: *J. Phys. Chem. C* 126.7 (2022), pp. 3520–3531.

[37] V. Crupi et al. “A new insight on the hydrogen bonding structures of nanoconfined water: a Raman study”. In: *J. Raman spectrosc.* 39.2 (2008), pp. 244–249.

[38] P. Smirnov et al. “X-ray diffraction study of water confined in mesoporous MCM-41 materials over a temperature range of 223- 298 K”. In: *J. Phys. Chem. B* 104.23 (2000), pp. 5498–5504.

[39] H. Khoder et al. “X-ray scattering study of water confined in bioactive glasses: experimental and simulated pair distribution function”. In: *Acta Crystallogr. A* 76.5 (2020), pp. 589–599.

[40] J. Als-Nielsen and D. McMorrow. *Elements of modern X-ray physics.* John Wiley & Sons, 2011.

[41] Martin Chaplin. *Water Structure and Science.* URL: `https://water.lsbu.ac.uk/water/`.

[42] H. Pathak et al. “Intermediate range O–O correlations in supercooled water down to 235 K”. In: *J. Chem. Phys.* 150.22 (2019), p. 224506.

[43] L. B. Skinner et al. “The structure of water around the compressibility minimum”. In: *J. Chem. Phys.* 141.21 (2014), p. 214507.

[44] S. Lele and T. R. Anantharaman. “Influence of crystallite shape on particle size broadening of Debye-Scherrer reflections”. In: *Proc. Natl. Acad. Sci. India A* 64 (1966), pp. 261–274.

[45] J. I. Langford and D. Louër. “Diffraction line profiles and Scherrer constants for materials with cylindrical crystallites”. In: *J. Appl. Cryst.* 15.1 (1982), pp. 20–26.

[46] F. Lehmkühler et al. “Structure beyond pair correlations: X-ray cross-correlation from colloidal crystals”. In: *J. Appl. Cryst.* 49.6 (2016), pp. 2046–2052.

[47] N. Mukharamova et al. “Revealing grain boundaries and defect formation in nanocrystal superlattices by nanodiffraction”. In: *Small* 15.50 (2019), p. 1904954.

[48] F. Lehmkühler, G. Grübel, and C. Gutt. “Detecting orientational order in model systems by X-ray cross-correlation methods”. In: *J. Appl. Cryst.* 47.4 (2014), pp. 1315–1323.

[49] I. A. Zaluzhnyy et al. “Angular x-ray cross-correlation analysis (AXCCA): Basic concepts and recent applications to soft matter and nanomaterials”. In: *Materials* 12.21 (2019), p. 3464.

[50] F. Schulz et al. “Plasmonic supercrystals with a layered structure studied by a combined TEM-SAXS-XCCA approach”. In: *Adv. Mater. Interfaces* 7.19 (2020), p. 2000919.

[51] F. Schulz et al. “Recent notable approaches to study self-assembly of nanoparticles with X-ray scattering and electron microscopy”. In: *Part. Syst. Charact.* 38.9 (2021), p. 2100087.

[52] I. Lokteva et al. “Coexistence of HCP and BCT phases during in situ superlattice assembly from faceted colloidal nanocrystals”. In: *J. Phys. Chem. Lett.* 10.20 (2019), pp. 6331–6338.

[53] An. Nilsson and L. G. M. Pettersson. “The structural origin of anomalous properties of liquid water”. In: *Nat. Commun.* 6.1 (2015), pp. 1–11.

[54] D. Hankins, J. W. Moskowitz, and F. H. Stillinger. “Water molecule interactions”. In: *J. Chem. Phys.* 53.12 (1970), pp. 4544–4554.

[55] D. Eisenberg and W. Kauzmann. *The structure and properties of water.* OUP Oxford, 2005.

[56] V. P. Voloshin and Y. I. Naberukhin. “Proper and improper hydrogen bonds in liquid water”. In: *J. Struct. Chem.* 57 (2016), pp. 497–506.

[57] K. Amann-Winkel et al. “X-ray and neutron scattering of water”. In: *Chem. Rev.* 116.13 (2016), pp. 7570–7589.

[58] R. Shi and H. Tanaka. “Direct evidence in the scattering function for the coexistence of two types of local structures in liquid water”. In: *J. Am. Chem. Soc.* 142.6 (2020), pp. 2868–2875.

[59] F. Perakis et al. “Coherent X-rays reveal the influence of cage effects on ultrafast water dynamics”. In: *Nature Comm.* 9.1 (2018), p. 1917.

[60] L. G. M. Pettersson and A. Nilsson. “The structure of water; from ambient to deeply supercooled”. In: *J. Non-Cryst. Solids* 407 (2015), pp. 399–417.

[61] A. Rosu-Finsen et al. “Medium-density amorphous ice”. In: *Science* 379.6631 (2023), pp. 474–478.

[62] V. F. Petrenko and R. W. Whitworth. *Physics of ice.* OUP Oxford, 1999.

[63] R. Ramírez, N. Neuerburg, and C. P. Herrero. “The phase diagram of ice Ih, II, and III: A quasi-harmonic study”. In: *J.Chem. Phys.* 137.13 (2012).

[64] E. B. Moore and V. Molinero. “Is it cubic? Ice crystallization from deeply supercooled water”. In: *Phys. Chem. Chem. Phys.* 13.44 (2011), pp. 20008–20016.

[65] T. L. Malkin et al. “Stacking disorder in ice I”. In: *Phys. Chem. Chem. Phys.* 17.1 (2015), pp. 60–76.

[66] L. Del Rosso et al. “Cubic ice Ic without stacking defects obtained from ice XVII”. In: *Nat. Mater.* 19.6 (2020), pp. 663–668.

[67] H. König. “Eine kubische eismodifikation”. In: *Z. Kristallogr. Cryst. Mater.* 105.1-6 (1943), pp. 279–286.

[68] T. Loerting et al. “How many amorphous ices are there?” In: *Phys. Chem. Chem. Phys.* 13.19 (2011), pp. 8783–8794.

[69] J. L. Finney et al. “Structures of high and low density amorphous ice by neutron diffraction”. In: *Phys. Rev. Lett.* 88.22 (2002), p. 225503.

[70] J. Deschamps et al. “A thermodynamic limit of the melting/freezing processes of water under strongly hydrophobic nanoscopic confinement”. In: *Phys. Chem. Chem. Phys.* 12.7 (2010), pp. 1440–1443.

[71] J. Jelassi et al. “Studies of water and ice in hydrophilic and hydrophobic mesoporous silicas: pore characterisation and phase transformations”. In: *Phys. Chem. Chem. Phys.* 12.12 (2010), pp. 2838–2849.

[72] E. B. Moore, J. T. Allen, and V. Molinero. “Liquid-ice coexistence below the melting temperature for water confined in hydrophilic and hydrophobic nanopores”. In: *J. Phys. Chem. C* 116.13 (2012), pp. 7507–7514.

[73] P. Gallo, M. Rovere, and S.-H. Chen. “Dynamic crossover in supercooled confined water: Understanding bulk properties through confinement”. In: *J. Phys. Chem. Lett.* 1.4 (2010), pp. 729–733.

[74] M. Erko et al. “Density minimum of confined water at low temperatures: a combined study by small-angle scattering of X-rays and neutrons”. In: *Phys. Chem. Chem. Phys.* 14.11 (2012), pp. 3852–3858.

[75] M. Aso et al. “Thermal behavior, structure, and dynamics of low-temperature water confined in mesoporous organosilica by differential scanning calorimetry, X-ray diffraction, and quasi-elastic neutron scattering”. In: *Pure Appl. Chem.* 85.1 (2012), pp. 289–305.

[76] S. Engemann et al. “Condensed Matter: Structure, etc.-Interfacial Melting of Ice in Contact with SiO2”. In: *Phys. Rev. Lett.* 92.20 (2004), pp. 205701–206100.

[77] S. Schöder et al. "Radiation-induced premelting of ice at silica interfaces". In: *Phys. Rev. Lett.* 103.9 (2009), p. 095502.

[78] M. Jażdżewska et al. "Structure of ice confined in carbon and silica nanopores". In: *Bull. Mater. Sci.* 42.4 (2019), pp. 1–7.

[79] Q. Yang et al. "Functionalized periodic mesoporous organosilicas for catalysis". In: *J. Mater. Chem.* 19.14 (2009), pp. 1945–1955.

[80] B. Karimi, H. M. Mirzaei, and A. Mobaraki. "Periodic mesoporous organosilica functionalized sulfonic acids as highly efficient and recyclable catalysts in biodiesel production". In: *Catal. Sci. Technol.* 2.4 (2012), pp. 828–834.

[81] S. Parambadath et al. "A pH-responsive drug delivery system based on ethylenediamine bridged periodic mesoporous organosilica". In: *Microporous Mesoporous Mat.* 215 (2015), pp. 67–75.

[82] K. M. Rao et al. "Tunable intracellular degradable periodic mesoporous organosilica hybrid nanoparticles for doxorubicin drug delivery in cancer cells". In: *ACS Biomater. Sci. Eng.* 4.1 (2018), pp. 175–183.

[83] S. Inagaki et al. "Light harvesting by a periodic mesoporous organosilica chromophore". In: *Angew. Chem.* 121.22 (2009), pp. 4102–4106.

[84] H. Takeda et al. "Light-Harvesting Photocatalysis for Water Oxidation Using Mesoporous Organosilica". In: *Chem. Eur. J.* 20.29 (2014), pp. 9130–9136.

[85] J. G. Croissant et al. "Syntheses and applications of periodic mesoporous organosilica nanoparticles". In: *Nanoscale* 7.48 (2015), pp. 20318–20334.

[86] T. Dang-Vu and J. Hupka. "Characterization of porous materials by capillary rise method". In: *Physicochem. Probl. Miner. Process.* 39 (2005), pp. 47–65.

[87] W. Wang et al. "Water repellent periodic mesoporous organosilicas". In: *ACS nano* 5.2 (2011), pp. 1267–1275.

[88] C. C. Collados et al. "Assessment of Hydrophilicity/Hydrophobicity in Mesoporous Silica by Combining Adsorption, Liquid Intrusion, and Solid-State NMR Spectroscopy". In: *Langmuir* (2024).

[89] E. Stefanutti et al. "Ice crystallization observed in highly supercooled confined water". In: *Phys. Chem. Chem. Phys.* 21.9 (2019), pp. 4931–4938.

[90] R. Richert. “Dielectric spectroscopy and dynamics in confinement”. In: *Eur. Phys. J. Spec. Top.* 189.1 (2010), pp. 37–46.

[91] N. C. Gießelmann et al. “Structure of Water under Confinement in Periodic Mesoporous Organosilicas Investigated by X-ray Scattering”. In: *J. Phys. Chem. C* 128.1 (2023), pp. 499–507.

[92] N. C. Gießelmann et al. “The structure of ice under confinement in periodic mesoporous organosilicas (PMOs)”. In: *J. Chem. Phys.* 161.3 (2024).

[93] M. Bilo. “Controlled pore glasses and alginate hydrogels as form-giving matrices for nanoporous organosilicas. University of Hamburg, Germany”. PhD thesis. 2019.

[94] J. Feng et al. “Hyperbranched polymer based on triphenylamine and pyridine: Fluorescent chemosensors for palladium ions”. In: *J. Appl. Polym. Sci.* 121.1 (2011), pp. 217–225.

[95] A.-C. Dippel et al. “Beamline P02.1 at PETRA III for high-resolution and high-energy powder diffraction”. In: *J. Synchr. Rad.* 22.3 (2015), pp. 675–687.

[96] A. Buffet et al. “P03, the microfocus and nanofocus X-ray scattering (MiNaXS) beamline of the PETRA III storage ring: the microfocus endstation”. In: *J. Synchr. Rad.* 19.4 (2012), pp. 647–653.

[97] C. Krywka et al. “A two-dimensional waveguide beam for X-ray nanodiffraction”. In: *J. Appl. Cryst.* 45.1 (2012), pp. 85–92.

[98] I. Lokteva et al. “In situ small-angle X-ray scattering environment for studying nanocrystal self-assembly upon controlled solvent evaporation”. In: *Rev. Sci. Instrum.* 90.3 (2019).

[99] DESY. *P21.1 High Energy X-Ray Diffraction for Physics and Chemistry.* Accessed on May 7, 2024. URL: `https://photon-science.desy.de/facilities/petra_iii/beamlines/p21_swedish_materials_science/p211_high_energy_x_ray_diffraction_for_physics_and_chemistry/index_eng.html`.

[100] J. A. Sellberg et al. “Ultrafast X-ray probing of water structure below the homogeneous ice nucleation temperature”. In: *Nature* 510.7505 (2014), pp. 381–384.

[101] C. Benmore, L. C. Gallington, and E. Soignard. “Intermediate range order in supercooled water”. In: *Mol. Phys.* 117.18 (2019), pp. 2470–2476.

[102] P. Juhás et al. “PDFgetX3: a rapid and highly automatable program for processing powder diffraction data into total scattering pair distribution functions”. In: *J. Appl. Crystallogr.* 46.2 (2013), pp. 560–566.

[103] T. Egami and S. J. L. Billinge. *Underneath the Bragg peaks: structural analysis of complex materials.* Newnes, 2012. Chap. 5.

[104] K. Yoshida et al. “Thermodynamic, structural, and dynamic properties of supercooled water confined in mesoporous MCM-41 studied with calorimetric, neutron diffraction, and neutron spin echo measurements”. In: *J. Chem. Phys.* 129.5 (2008), p. 054702.

[105] W. A. Kamitakahara et al. “Temperature dependence of structure and density for D2O confined in MCM-41-S”. In: *J. Phys. Condens. Matter* 24.6 (2012), p. 064106.

[106] D. T. Bowron et al. “The local and intermediate range structures of the five amorphous ices at 80K and ambient pressure: A Faber-Ziman and Bhatia-Thornton analysis”. In: *J. Chem. Phys.* 125.19 (2006), p. 194502.

[107] R. Mancinelli et al. “Multiscale approach to the structural study of water confined in MCM41”. In: *J. Phys. Chem. B* 113.50 (2009), pp. 16169–16177.

[108] M. Erko, D. Wallacher, and O. Paris. “Deformation mechanism of nanoporous materials upon water freezing and melting”. In: *App. Phys. Lett.* 101.18 (2012), p. 181905.

[109] P. F. Peterson et al. “Improved measures of quality for the atomic pair distribution function”. In: *J. App. Crystallogr.* 36.1 (2003), pp. 53–64.

[110] K. Domin et al. “Structure of ice in confinement: Water in mesoporous carbons”. In: *J. Chem. Eng. Data* 61.12 (2016), pp. 4252–4260.

[111] M. Thangswamy et al. “Evolution of confined ice nano structures at different levels of pore filling: a synchrotron based X-ray diffraction study”. In: *Phys. Chem. Chem. Phys.* 22.25 (2020), pp. 14309–14317.

[112] K. Röttger et al. “Lattice constants and thermal expansion of H2O and D2O ice Ih between 10 and 265 K”. In: *Acta Crystallogr. B* 50.6 (1994), pp. 644–648.

[113] K. Röttger et al. “Lattice constants and thermal expansion of H2O and D2O Ice Ih between 10 and 265 K. Addendum”. In: *Acta Crystallogr. B* 68.1 (2012), pp. 91–91.

[114] R. P. Kurta, M. Altarelli, and I. A. Vartanyants. “Structural Analysis by X-ray Intensity Angular Cross Correlations”. In: *Adv. Chem. Phys.* 161 (2016), pp. 1–39.

[115] K. Morishige and H. Uematsu. “The proper structure of cubic ice confined in mesopores”. In: *J. Chem. Phys.* 122.4 (2005), p. 044711.

[116] M. Erko et al. “Repeated sorption of water in SBA-15 investigated by means of in situ small-angle x-ray scattering”. In: *J. Phys. Condens. Matter* 24.28 (2012), p. 284112.

[117] Zhilin Cheng et al. “Wettability control on imbibition behavior of oil and water in porous media”. In: *Phys. Fluids* 34.7 (2022).

[118] Juan Sanchez et al. “Deformation dynamics of nanopores upon water imbibition”. In: *PNAS* 121.38 (2024), e2318386121.

[119] Manuel Brinker et al. “Giant electrochemical actuation in a nanoporous silicon-polypyrrole hybrid material”. In: *Sci. Adv.* 6.40 (2020), eaba1483.

[120] Manuel Brinker and Patrick Huber. “Wafer-Scale Electroactive Nanoporous Silicon: Large and Fully Reversible Electrochemo-Mechanical Actuation in Aqueous Electrolytes”. In: *Adv. Mater.* 34.1 (2022), p. 2105923.

Acknowledgements

Finishing this thesis is of course something that I could not have done all alone. There are so many people that helped me on this path and that I would like to acknowledge in the following.

First, I want to thank the people that have supervised the project over these years: Gerhard Grübel, who gave me the opportunity to work in the Coherent X-ray Scattering Group and at such an exciting facility as DESY, as well as Andreas Stierle, who took over the project first supervisor at such an advanced state. I also want to thank the second supervisor of the thesis, Michael Fröba, for his valuable input and thorough scientific discussions of the topic. I am especially thankful to Felix Lehmkühler for his day-to-day help and guidance. He always has an open door for questions and problems and has a real talent for giving his input without being overbearing. Any Doctoral student can count himself lucky to work under Felix' supervision!

I also want to thank the members of the group (Should I call it CXS or SMP?), as well as the P10 staff, which is very closely connected to the group. To name here are Robert Bauer, Francesco Dallari, Felix Lehmkühler, Claudia Goy, Svenja Hövelmann, Wonhyuk Jo, Michael Sprung, Wojciech Roseker, Michael Walther and especially my office mates, Nele Striker and Alexander Gierke. A special thanks also goes to Fabian Westermeier, who took over the role as my DESY mentor. Even though I only met everyone remotely at first, there was always such welcoming and friendly atmosphere. I especially want to thank the half of the group that does not care about football for their patience in the endless discussions of the last matches that the other half would engage in every week.

I want to thank the group of Michael Fröba at the chemistry department at the university of Hamburg, especially Sophia-Marie Meinert, Philip Lenz, Támas Simon and Christian Köhn for the great collaboration, valuable scientific discussions, help at the beamtimes and for their patience in explaining the complexities of inorganic chemistry to a physicist like me.

A PhD project at a synchrotron facility entails a lot of time on the beamline, something

that I had no experience in before joining the FS-CXS group. I want to thank Francesco, who I joined for my first ever beamtime. Since then I had the privilege of joining a lot of projects at DESY, European XFEL and ESRF and I am thankful to everyone that allowed me to join their experiments and gain the experience that I have now. I especially want to thank everyone who joined the experiments that contributed to this thesis. A beamtime is always a team effort and without their help, this project would not have been possible. I also want to thank Jo in particular for giving me a bit of a head start thanks to some preliminary analysis on some old that he did and shared with me. Thank you also to the beamline staff at P02.1, P21.1 and the nanofocus endstation at P03, where the experiments were conducted.

For the scientific exchange and discussions I also want to thank all the members of the state funded research (LFF) project "Control of the special properties of water in nanopores". The regular meetings were invaluable to understanding and interpreting the data. Furthermore, this doctoral project was funded by this LFF and I am therefore grateful for the possibility of doing this exciting research as a job.

I also want to mention the PhD initiative DOIT that voices the concerns and standpoints of doctoral researchers on Campus Bahrenfeld to DESY and the University of Hamburg. I had the privilege of representing this initiative for almost the entirety of my time at DESY as a speaker and I want to thank my fellow speakers over the time, Philipp Amstutz and Ana Ventura Barroso, as well as all the other active members for their engagement. In this context, I also want to thank the team of the PIER Helmholtz Graduate School, especially Stefanie Tepass and Mirko Siemssen, for their effort in providing great conditions and learning opportunities for the doctoral students.

Last but most definitely not least I want to thank my friends and family for their help and support over the years, not only of my PhD, but also what came before. I recognize that I was able to study under conditions that not many others can enjoy and that I did not have to worry about many things that pose major problems for other students. I am therefore very grateful to my parents, Sabine and Frank for their support. Without them, I probably would not have been able to reach the point of starting a PhD in the first place. Lastly, I want to thank Johanna for making the move to Hamburg with me, for helping me through the difficult times of frustration that are part of every PhD journey and just generally for always being there.

Eidesstattliche Versicherung

Hiermit versichere ich an Eides statt, die vorliegende Dissertationsschrift selbst verfasst und keine anderen als die angegebenen Hilfsmittel und Quellen benutzt zu haben.

Sofern im Zuge der Erstellung der vorliegenden Dissertationsschrift generative Künstliche Intelligenz (gKI) basierte elektronische Hilfsmittel verwendet wurden, versichere ich, dass meine eigene Leistung im Vordergrund stand und dass eine vollständige Dokumentation aller verwendeten Hilfsmittel gemäß der Guten wissenschaftlichen Praxis vorliegt. Ich trage die Verantwortung für eventuell durch die gKI generierte fehlerhafte oder verzerrte Inhalte, fehlerhafte Referenzen, Verstöße gegen das Datenschutz- und Urheberrecht oder Plagiate.

13.5.2025 N. G

Datum Unterschrift der Doktorandin / des Doktoranden